NTNU – Trondheim
Norwegian University of
Science and Technology

Seismic Expression of Deep-Water Fan with an Example from Triassic in Southwestern Barents Sea

Murad Babayev

Petroleum Geosciences
Submission date: November 2014
Supervisor: Ståle Emil Johansen, IPT

Norwegian University of Science and Technology
Department of Petroleum Engineering and Applied Geophysics

This thesis is dedicated to my beloved family

Acknowledgements

This thesis has been carried out at the Department of Petroleum Engineering and Applied Geophysics, Norwegian University of Science and Technology (NTNU). The thesis is the final product of TPG4925 – Master's Thesis in Petroleum Geophysics.

I would like to express my gratitude to my supervisor Professor Ståle Emil Johansen for giving me the opportunity to work with him on such an interesting topic and for guidance and support throughout the course of this work.

It is a pleasure to acknowledge with gratitude the financial support of Norwegian Government for two years of International Master's Program.

I also would like to thank my friends, Farad Kamyabi, Dicky Harishidayat, Juan Carlos Gloria López and Togi Yonathan Sitinjak, who were so supportive and generous. They always kept my moral high and motivated me to complete my thesis work.

Most importantly, none of this would have been possible without the endless love and patience of my family. My family, to whom this thesis is dedicated to, has been a constant source of love, support and encouragement during these two years.

Murad Fikrat Babayev

Trondheim, 2014

Abstract

Generation of high-quality 3D seismic data and easy access to this data across the deep-water environments together with the prior interest of oil companies in the deep-water exploration has attracted geoscientists to the thorough understanding of the deep-water depositional systems over the past few years. In this thesis work, 3D seismic data with several interpretation techniques gave the opportunity to demonstrate seismic expression of deep-water fan with an example from the Triassic in the southwestern Barents Sea. In order to perform a flawless analysis, it is significant to understand the internal architecture and development phases of the fan system by seismic expression of each depositional element in plan- and cross-sectional views.

The combination of flattening method with RMS seismic attribute is applied to demonstrate the evidences of fluvial and deep-water depositional systems in the upper (Snadd) and the lower (Havert) part of the Triassic formations. The advanced methods such as model and geobody extractions are performed to confirm the internal architecture of deep-water fan which is accurately presented in the image extracted by flattening rather than regular interpretation methods. Integration of plan- and cross-sections provides a better understanding of geomorphologic analysis which leads to categorize depositional elements such as main feeder channel, crevasse splay and channels, distributary channels and channelized lobe complex deposited within a low shelf to basin floor setting. These elements are generated through the development of fan system from initiation and growth phases to retreat phase. There exist similarities and differences in the architecture of fluvial and deep-water channels; the similarities are in shape, stream width and sinuosity ratio while the stream lengths are different for both channel systems. These comparisons also show that the seismic expression of deep-water system is clearly visible in the data rather than the fluvial counterparts.

Contents

List of Figures

List of Tables

Chapter 1

Introduction

Discovering the high potential fields such as Johan Castberg (former Skrugard) and Alta in the southwestern Barents Sea made this area to be in a great involvedness for the aim of the research projects in different fields, especially Geoscience. Even though the explorations in this area have been started almost 30 years ago, experts unanimously believe that large parts of the southwestern Barents Sea are still undiscovered. As shown in Figure 1.1a, the study area is located in the southwestern Barents Sea where Nordkapp Basin and Hammerfest Basin are separated by Loppa High, Bjarmeland Platform, and Finnmark Platform. These structures act as sedimentary basins in Triassic times, a calm period with regard to regional subsidence. In 2005, Hadler-Jacobsen et al. described that the sediments are mainly prograded on the Finnmark Platform developing deep-water fan system by focusing on its lithology distribution. This study aims to provide seismic expressions of deep-water fan with an example from the Triassic in the southwestern Barents Sea.

Availability of 3D seismic data and various innovative interpretation tools allowed expressing the seismic anomalies (Figure 1.2) associated with the stratigraphic features in the subsurface. This thesis is mainly focused on the seismic expression of deep-water fan system with targets into lower Triassic to understand the internal architecture and geomorphology of depositional elements and development trend using both cross- and plan-sectional views together. Another aim of the work is to recognize fluvial systems in the upper part of the Triassic in order to find out the similarities and differences of channels distributed in the area.

It is necessary to use ideal interpretation method to demonstrate the expression of

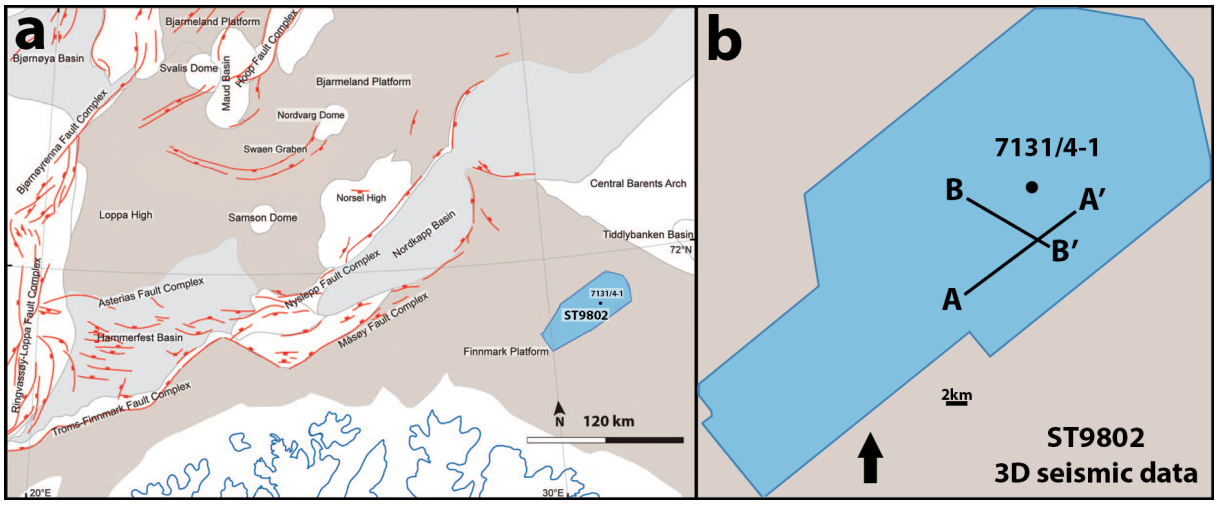

Figure 1.1: a) 3D seismic data (ST9802) outlined on the Finnmark Platform, SW Barents Sea (modified from Klausen et al., 2014), b) enlarge of seismic data is displayed with A-A' and B-B' composite sections (for section views, see Figure 1.2).

deep-water fan system in detail, even in low seismic resolution, as another purpose of this study. In my work, a flattening method is used to neglect structural effects and leave stratigraphic events seen on a flat surface. Integration of the method with various seismic attributes would display the seismic anomalies in the data precisely.

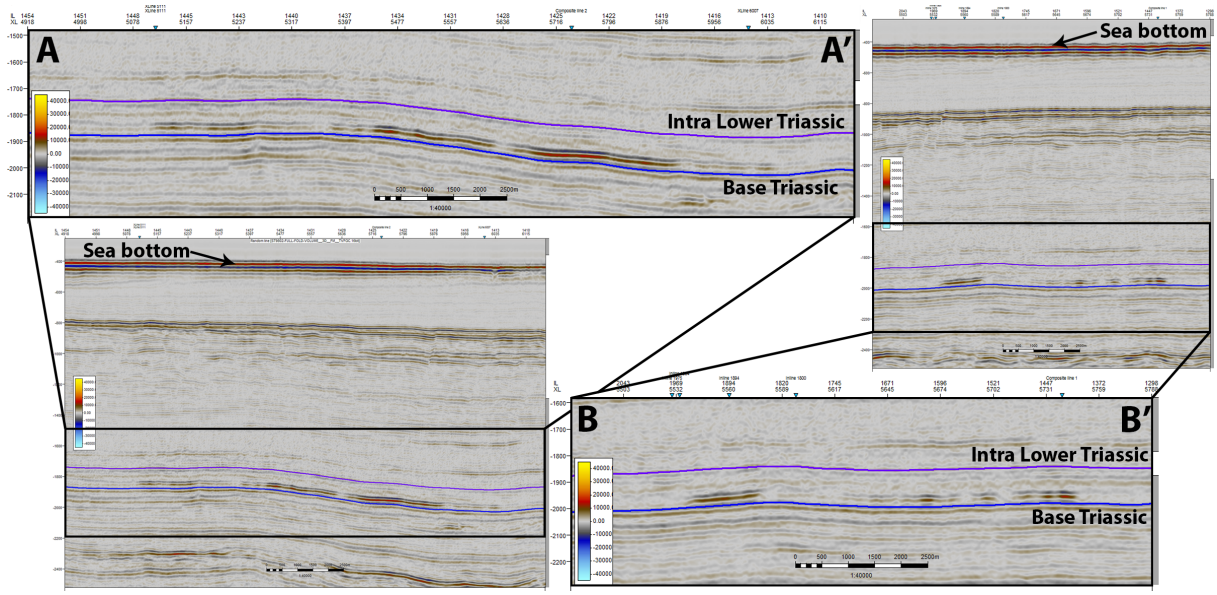

Figure 1.2: A-A' and B-B' composite sections (generated from the seismic data using Petrel software) demonstrate the seismic anomalies within the Triassic succession. The details of seismic anomalies are well illustrated in the enlarged part of the sections. Intra Lower and Base Triassic horizons are represented by purple and blue colors, respectively.

The surface maps of horizon interpretation method can be compared against the time slices of flattened method. The advanced interpretation methods such as model

construction and geobody extraction can also be used as alternative ways of expressing deep-water fan system.

The existence of depositional systems can be identified using flattening method in both upper and lower part of Triassic formations. This is not only significant for stratigraphic analyses, but also for comparing different channel systems, especially meandering type of channels.

Integration of cross- and plan-sectional views can provide a better understanding of seismic geomorphologic analysis which leads to identify the depositional elements and development phases of deep-water fan system.

This thesis includes seven chapters. Chapter 1 is an introduction to the study. Regional geology of the Barents Sea is reviewed in chapter 2. The detailed geological evolution of the area in Triassic times is also explained in this chapter. Chapter 3 is about the data and software packages used in the study. The methodology description is presented in chapter 4. Chapter 5 includes time slices, models and geobody extraction obtained. The results are discussed in chapter 6. Finally, chapter 7 includes the main conclusions of this study.

Chapter 2

Regional Geology

Extending from the Artic Ocean to northern Norway and Russian coastlines, and from the Norwegian—Greenland Sea to Novaya Zemlya, the Barents Shelf includes two major western and eastern geological provinces (Worsley, 2008). Five main depositional stages can be used for the thorough description of the region development starting from the late Paleozoic period. These stages show the continued movement of this part of the Eurasian plate from the equator in the middle Devonian—early Carboniferious until its nowadays High Artic latitudes; these caused important changes in the climate effecting the stratigraphy (Worsley, 2008). The stratigraphy of the western and eastern Barents Sea is illustrated in Figure 2.1. In 1984, Faleide et al. outlined the three major post-Caledonian tectonic stages in which the main structural elements were developed:

(1) The Svalbardian stage in the period of Late Devonian—Early Carboniferous.

(2) The Mid and Late Kimmerian stage from middle Jurassic to Early Cretaceous

(3) The tectonism occurred in the Norwegian—Greenland Sea ending up with the progressive northward opening in Cenozoic times.

2.1 Late Paleozoic

The major tectonic movements of Baltica and Laurentia collision happened in Middle Paleozoic affected the southwestern Barents Sea shown in Figure 2.2a (Gernigon and Brönner, 2012). It is well-proven that Caledonian and older Precambrian basement structures have tectonic effects on the structural and basin developments in the Barents Sea (Gernigon and Brönner, 2012). The Caledonides consolidated in the Late Silurian—Early

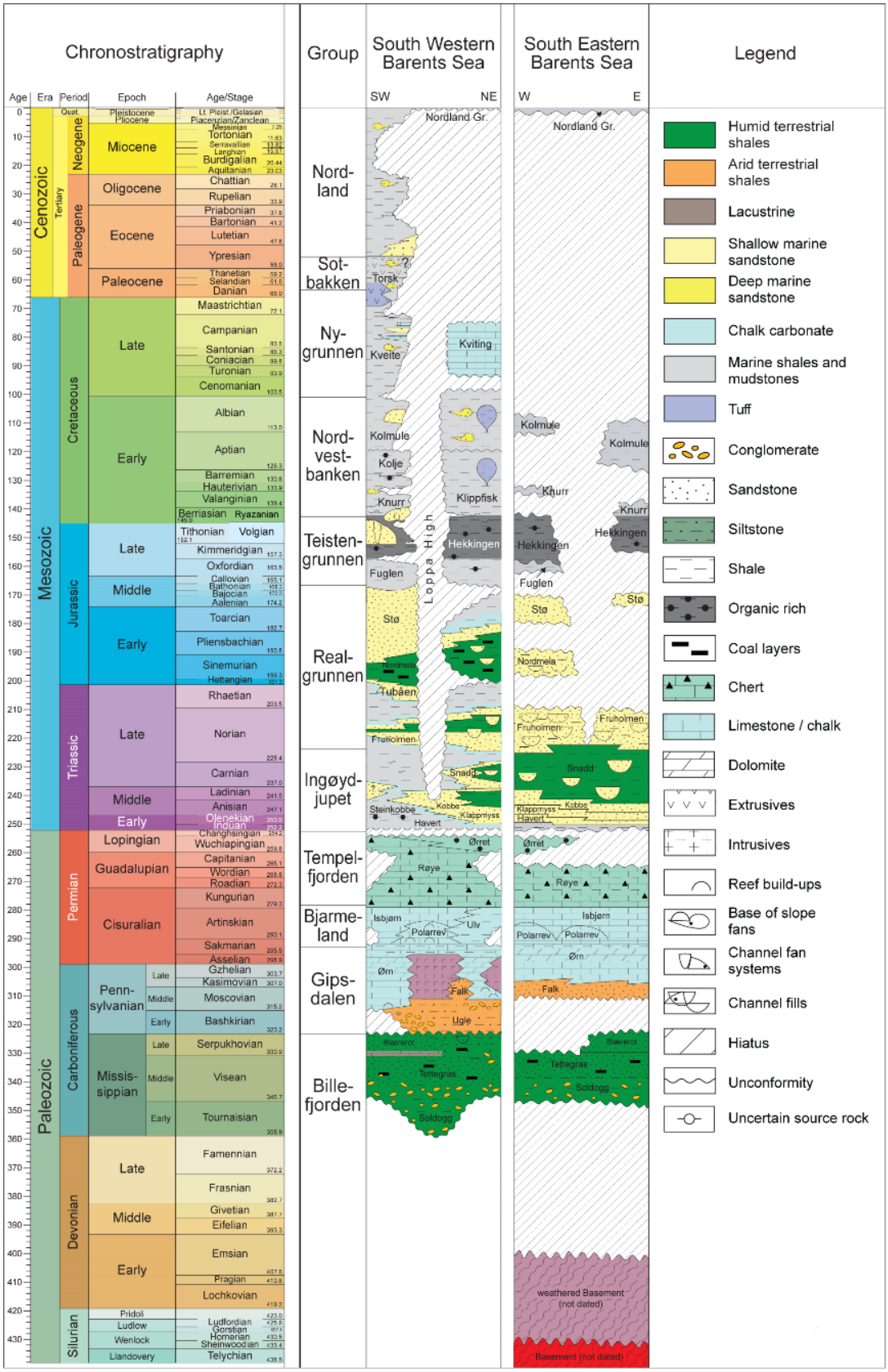

Figure 2.1: Lithostratigraphy of South Western and Eastern Barents Sea (modified from Ogg, 2013).

Devonian, form the metamorphic basement of the western Barents shelf. The erosion and uplift happened due to the orogeny led to the sediment deposition such as Old Red molasses (Faleide et al., 1984). Finnmark is among the platforms that have not experienced any orogenic events after the late Silurian—early Devonian Caledonian orogeny; however, graben systems constituted in the late Devonian, and vast swamp areas with prograding fans covered the most of the Barents Shelf (Bugge et al., 1995).

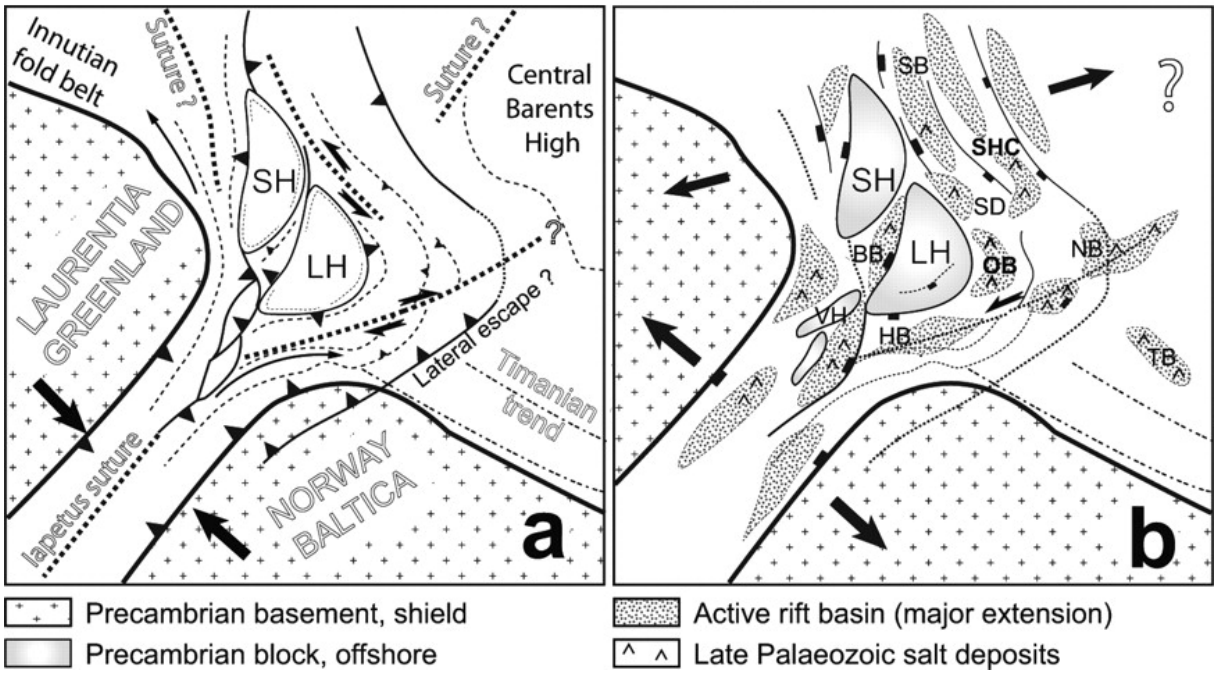

Figure 2.2: Paleozoic sketches of structural evolution of the SW Barents Sea: a) Lateral tectonic movements of Baltica and Laurentia caused by collision in Devonian time, b) extension happened in the Late Devonian to the Early Carboniferous resulted in Late Palaezoic graben development (modified from Gernigon and Brönner, 2012).

Together with rifting, extension (Figure 2.2b) which has been recognized to be the most dominant type of deformation happened since the Late Devonian to the Early Carboniferous period in the western Barents Sea, affected the area between Norway and Greenland (Gudlaugsson et al., 1998). Svalbardian movements, known to be the final stage of the Caledonian deformation, resulted in the horst and graben geometries in addition to the fan-shaped array of NE—SW trending along the Caledonian basement grain, all representing the Late Paleozoic period (Glørstad-Clark et al., 2010). These graben geometries filled by sediments demonstrates a coarsening-upward succession from meandering river sandstones to braided river and alluvial fan sandstones. There exists an eastwards transition in the deposits of the Finnmark Platform from continental to shallow marine (Bugge et al., 1995; Worsley, 2008). The replacement of the depositions by

the coastal plain sandstones and coals occurs gradually due to the sea regression in the Finnmark Platform in the Early Carboniferous times (Bugge et al., 1995).

Including different types of facies, which contain the depositions of evaporates and some clastics, carbonate sediments are developed in Mid-Carboniferous within a wide extent of Sverdrup to Pechora basins (Faleide et al., 1984; Gudlaugsson et al., 1998).

Regional subsidence dominated the tectonic movements in the SW Barents Sea in the Late Carboniferous (Gudlaugsson et al., 1998). Afterwards in the beginning of the Late Permian, recently developed Norwegian—Greenland rift system opens a continuous seaway ranging from the Arctic in the north to the northwest European basin in the south; however, this seaway was closed in the next period i.e., the Triassic (Glørstad-Clark et al., 2010). Progradation of clastic deposits over carbonate platform happened in the Late Permian times covering the Arctic area. The deposition started to prograde from the Uralian Mountains in the east to Novaya Zemlya further north in the eastern Barents Sea, whereas the clastic deposits in the south prograded mostly to the Finnmark Platform (Bugge et al., 1995).

2.2 Mesozoic

2.2.1 Triassic

In the Triassic times, the SW Barents Sea area known to be a part of Pangaea was exposed to two tectonic activities, one coming from Uralian Mountain building affecting the east and southeast part, and the other due to the crustal extension happened in the North Atlantic rift system toward the west which controlled the accommodation space in this area throughout the Triassic (Glørstad-Clark et al., 2010). Despite the Bjørnøya Basin and the northern plunging part of the paleo-Loppa High, Finnmark Platform happened to stay in the shallow marine environments during the course of deposition. The generation of accommodation space happened continuously during the reactivation of older structures and tectonic subsidence in this area (Glørstad-Clark et al., 2010).

In the early Triassic, the underlying siliceous-made units covered by a quite different unit after the deposition of the non-siliceous shales and mudstones. Whilst the early to middle Triassic shales are locally organic-rich, the Anisian/Ladinian are mostly rich in the organic matter, and important source rocks have been formed in this period (Worsley,

2008). Having a deltaic character, the sandstone source of the Ladinian/Carnian comes from various areas where the overlying Norian units indicate the signs of coastal/shallow marine environments (Worsley, 2008).

Early Triassic

The comparatively large infill in the Barents Sea when compared to the small input in the Hammerfest Basin brings up that the main source of the sediment through the deposition of Induan was the erosion of the Hercynian mountain chains to the east (Skjold et al., 1998). Figure 2.3 shows the paleogeographical development of the Induan stage, with the sea-level fall begins at the base of Dienerian. Primarily and before the progradation in the SW Barents Sea, the sediments must have been deposited in major basins of the east through the late Induan age (Glørstad-Clark et al., 2010). The increased degree of the structural elements' activity affected the sedimentation process (Glørstad-Clark et al., 2010). Probably happened in the latest Permian, the extension in the North Atlantic caused the most prominent highs such as the paleo-Loppa High, Stappen High and Bjørnøya-Sørkapp High. In the earliest Triassic times, this extentional regime propagated southwards with rifting between Greenland and Norway (Glørstad-Clark et al., 2010). The works also showed that the sigmoidal sequences are mainly prograded on the Finnmark Platform from the Fennoscandian Shield in the earliest Triassic (Skjold et al., 1998; Hadler-Jacobsen et al., 2005; Glørstad-Clark et al., 2010) where the development of the basin floor-fans in the lower subsequence was already discussed in work done by Hadler-Jacobsen et al. (2005).

The uplift and volcanism to the west was likely influenced by extensional tectonic activity in the east of the Uralian Mauntains reached through Smithian (Skjold et al., 1998). The paleogeography of the final stage of Smithian is shown in Figure 2.3. Both the Hammerfest Basin and Svalbard can be recognized with a specific feature, the so-called Smithian—Spathian boundry where the coarse-grained lithologies appear. As shown in Figure 2.3, the simultaneous commence of salt movement in the Nordkapp Basin led to a period of unrest with tectonic activities during early Spathian (Skjold et al., 1998).

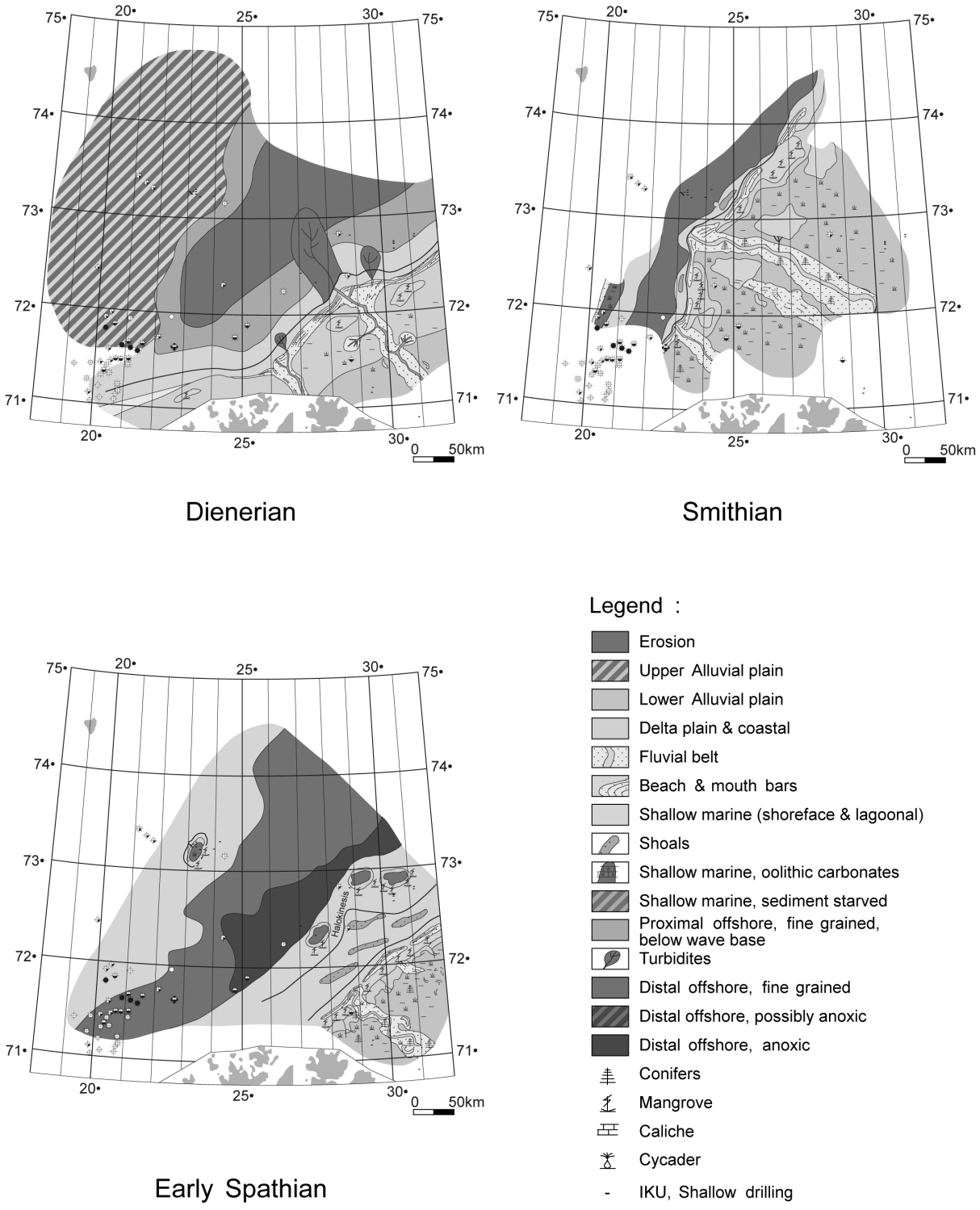

Figure 2.3: Early Triassic paleogeographical development — Dienerian, Smithian and Early Spathian (modified from Skjold et al., 1998).

Middle Triassic

The final stage of the rifting process between Norway and Greenland during the Mid Triassic in the North Atlantic rift system opposes to the recreated part of minor uplift of

the paleo-Loppa High during Early Triassic (Glørstad-Clark et al., 2010). The so-called western Barents Sea, a region with a central deeper trough in the Anisian, developed from a marine shelf. Figure 2.4 illustrates the paleogeographical development of Early and Late Anisian. The main sediment sources of the southern Barents Sea region are Novaya Zemlya and the Uralides in the east, the Baltic Shield to the south (Riis et al., 2008). A system of clinoforms trending in the north-northeast direction, covering the Bjarmeland Platform and Hammerfest Basin, has possibly been located in some area next to the paleocoast by the mid-Anisian, having the probability of sand deposition in delta-front environments (Worsley, 2008). The predominant deposition of fine-grained sediments in the Ladinian is the outcome of reversion in the Anisian progradational trend into a retrogradational process happening at the Anisian/Ladinian boundary (Skjold et al., 1998).

The paleotopographic relief related to Late Paleozoic uplift and rifting influenced the deposition during Triassic period. This relief was filled in with the sediments of the early and middle Ladinian (Glørstad-Clark et al., 2010). Among the existing multiple sediments sources, the main sediment source areas of the western Barents Sea were in the east and southeast of the area through the Triassic ages. The paleogeographic development of Late Anisian/Early Ladinian and Late Ladinian are summarized in Figure 2.4. The main southeastern source area was probably associated with the Uralian orogeny, while Novaya Zemlya to the east was likely more prominent source areas during Mid to Late Triassic (Glørstad-Clark et al., 2010).

Late Triassic

A supercontinent, Pangaea, postulated to be existed throughout the Triassic time, comprised intra-supercontinental rifting and continental reorganization processes by Late Triassic (Glørstad-Clark et al., 2010).

The deposition of shales containing high amount of organic materials on the Svalbard Platform carried on during the Ladinian time in which the prodelta shales were developed mostly in front of the prograding system in NW trend. By time, floodplain and deltaic became the dominant environments covering the province (Worsley, 2008). During the Carnian time, deltas prograded and went down (Worsley, 2008). Substantial changes in paleogeography occurred in the Ladinian/Carnian transition period as a result of sedimentation to coarse clastic (Skjold et al., 1998). Figure 2.5 shows the paleogeographical

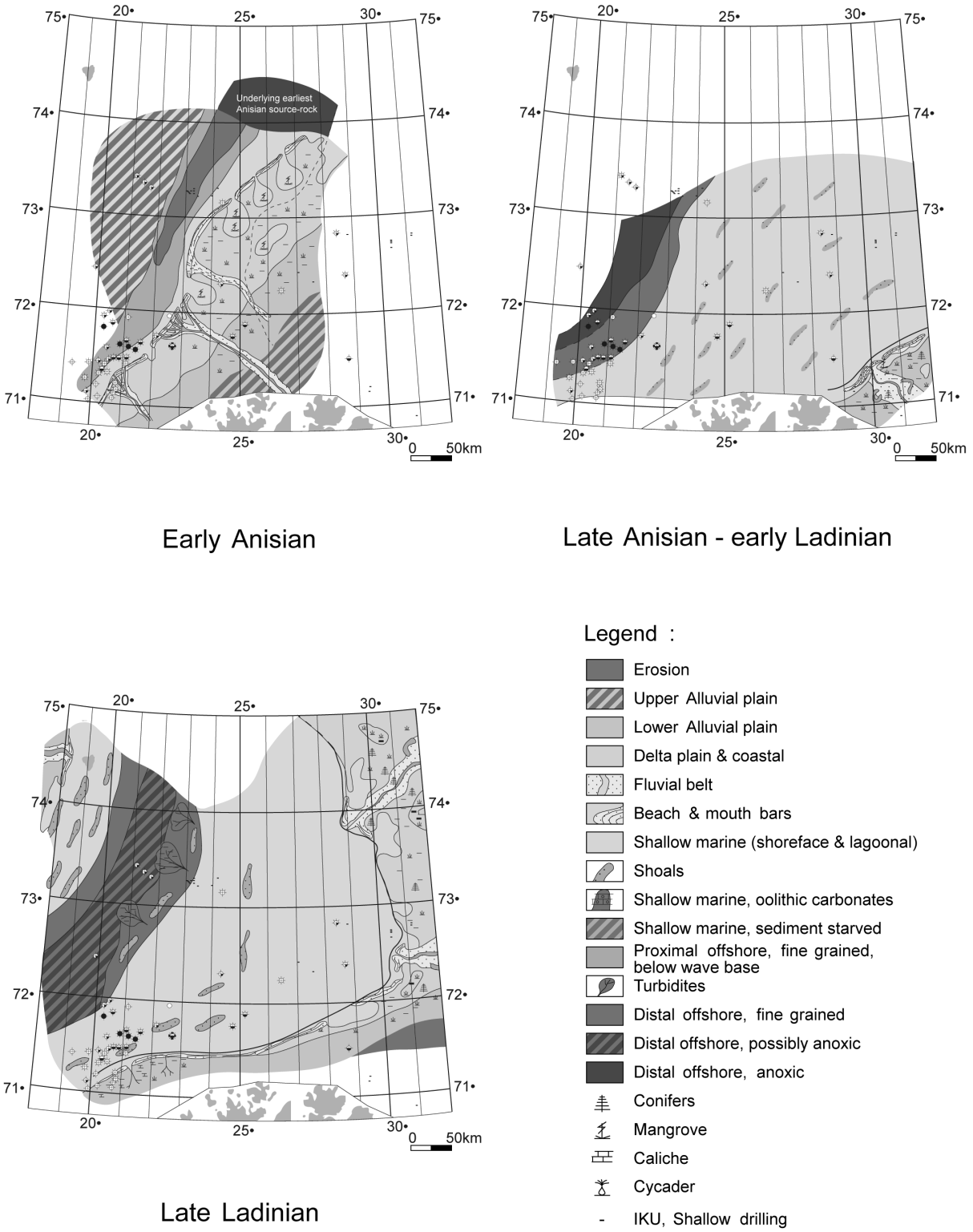

Figure 2.4: Middle Triassic paleogeographical development — Early Anisian, Late Anisian/early Ladinian and Late Ladinian (modified from Skjold et al., 1998).

construction of Early Carnian. Better reservoir properties were observed in the Carnian sandstones existing in the Finnmark Platform and Nordkapp Basin when it is compared to the northern sandstones. The mature provenance in the Baltic Shield is known to

be the source of these channel and coastal sands (Worsley, 2008). Subsidence processes were still happened in an intense degree all over the region (Worsley, 2008). Geographically synchronous transgressive/regressive sequences throughout the region have broken down due to the growing local tectonic activity (Worsley, 2008). The progradations' base starts from Ladinian in southeastern areas and extends to the Carnian prodeltaic shales on Spitsbergen (Worsley, 2008).

Although, it is highly probable that there exists no tectonic change in the Carnian/Norian transition, some basic environment-related changes are observed at the Carnian/Norian boundary (Skjold et al., 1998). The marine connection between the Boreal and Tethyan oceans were established by a supra regional relative rise in the sea-level in Early—Norian (Figure 2.5) (Worsley, 2008). Progradational systems finding their source in Uralides were replaced by coastal and shallow-marine environments created throughout the province. The environmental changes affect the sandstones, so they have very good conditions for the possible reservoirs in the south part of the Hammerfest Basin (Worsley, 2008).

2.2.2 Jurassic and Cretaceous

The early Kimmerian tectonic regime did not disturb the Barents Sea area during the Triassic to Jurassic (Faleide et al., 1984). The major rifting was not started in the area of East Greenland no earlier than Mid Kimmerian phase in Mid Jurassic times. The discrete pulses occur in the Mid Kimmerian phase and affect the rift system at the time of the Mid and Late Jurassic (Faleide et al., 1984) shown in Figure 2.6a. The Late Kimmerian tectonic regime was started at the transition period of Jurassic—Cretaceous. Normal faults along the weak zones of the Caledonian basement together with the tilted fault blocks in the southwestern part of the Barents Sea were created by these tectonic movements. Transpressional forces were also been active in the same tectonic phase (Faleide et al., 1984).

The basins of Bjornoya, Tromso and Harstad were the major depocenters in the SW Barents Sea through Early Cretaceous. The major fault complexes caused the basins to be separated from the stable areas to the east (Faleide et al., 1993). The opening of the Labrador Sea happened in the Late Cretaceous—Early Cenozoic period with regional subsidence along the North Atlantic rift basins (Faleide et al., 1993). The subsidence

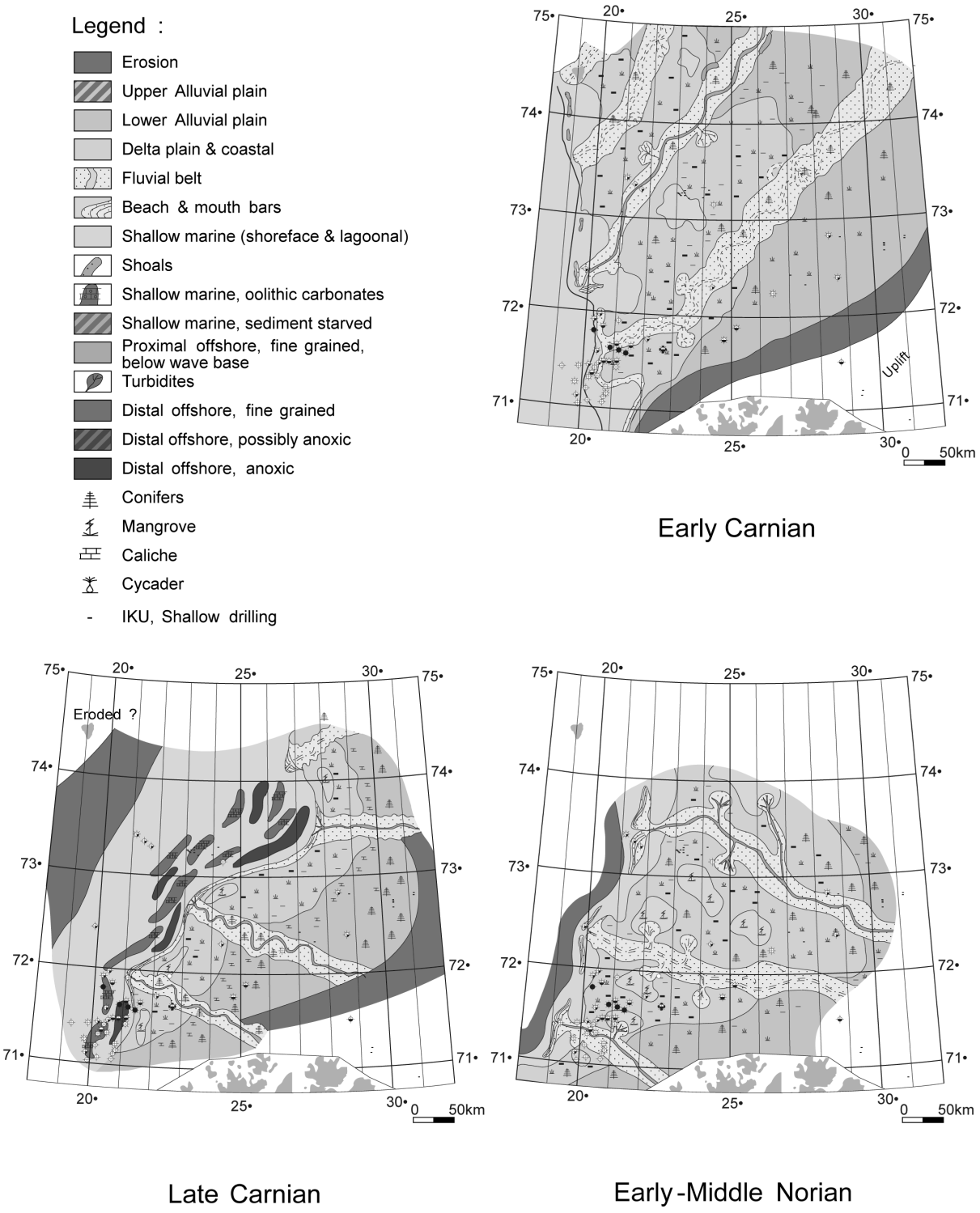

Figure 2.5: Middle to Late Triassic paleogeographical development — Early Carnian, Late Carnian and Early-Middle Norian (modified from Skjold et al., 1998).

continued in the southwestern area whilst Svalbard area stayed elevated during the same period. The southwestern area was influenced by faulting and subsidence before the Norwegian—Greenland opening (Faleide et al., 1984).

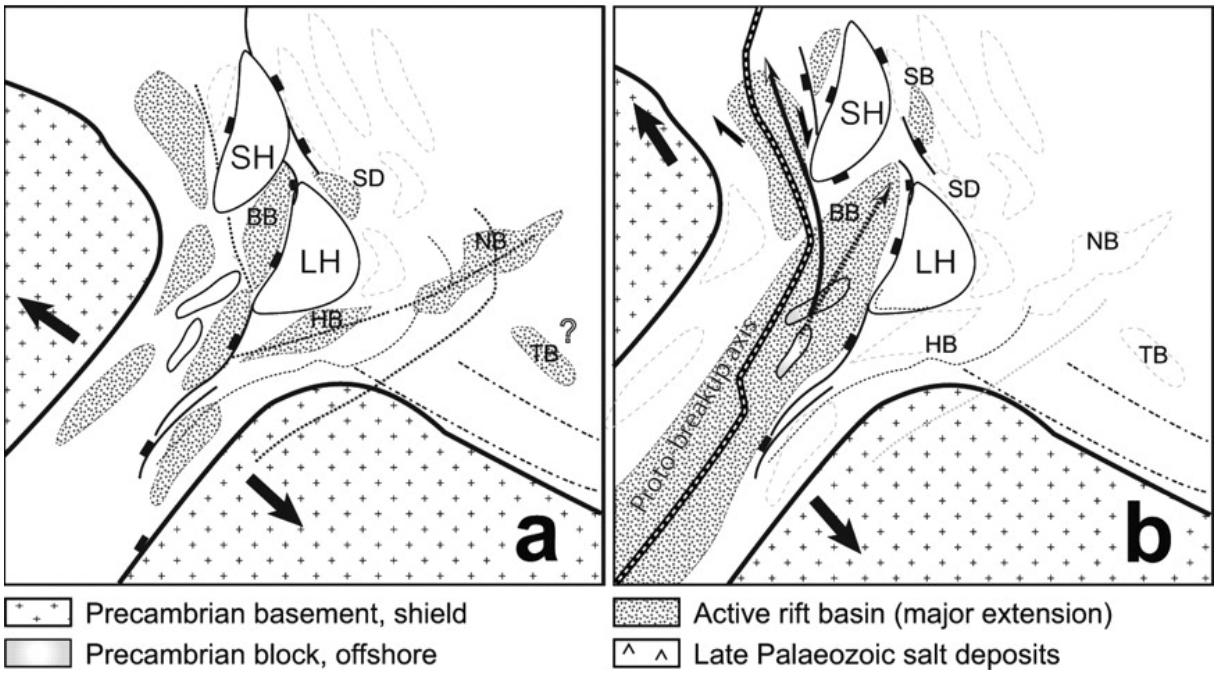

Figure 2.6: Mesozoic and Cenozoic sketches of structural evolution of the SW Barents Sea: a) Rift system leading to main stages of graben development at the time of the Early to Mid Mesozoic, b) continental break up between Laurentia and Baltica in Early Cenazoic times (modified from Gernigon and Brönner, 2012).

2.3 Early Cenozoic

In the Barents Sea during early Cenozoic, the western margin developed into a sheared margin due to the westward and northward rifting and continental break up, which reactivated the major wrench system called Kimmerian in the Laramide phase (Faleide et al., 1984), followed by sea floor spreading in the Eurasian Basin and Norwegian—Greenland Sea as shown in Figure 2.6b (Faleide et al., 1993; Glørstad-Clark et al., 2010; Glørstad-Clark et al., 2011). The regional uplift and erosion were the major activities in the Barents Sea through this period, with maximum degree of uplift increasing in the south-north and east-west trends, creating tilting from north to south (Faleide et al., 1993; Glørstad-Clark et al., 2010; Glørstad-Clark et al., 2011).

Chapter 3

Dataset

The seismic and well data were provided by Norwegian Petroleum Directorate (NPD). The seismic data (ST9802) is 3D post stack time migration acquired by Geco Prakla (Western Geco) on 25th of August 1999. Figure 3.1 illustrates the area of 3D survey in which an area of 1500 km^2 constrained by the black line is available for seismic interpretation out of the total area of 1900 km^2. ST9802 includes 2192 inlines and 5535 crosslines. The

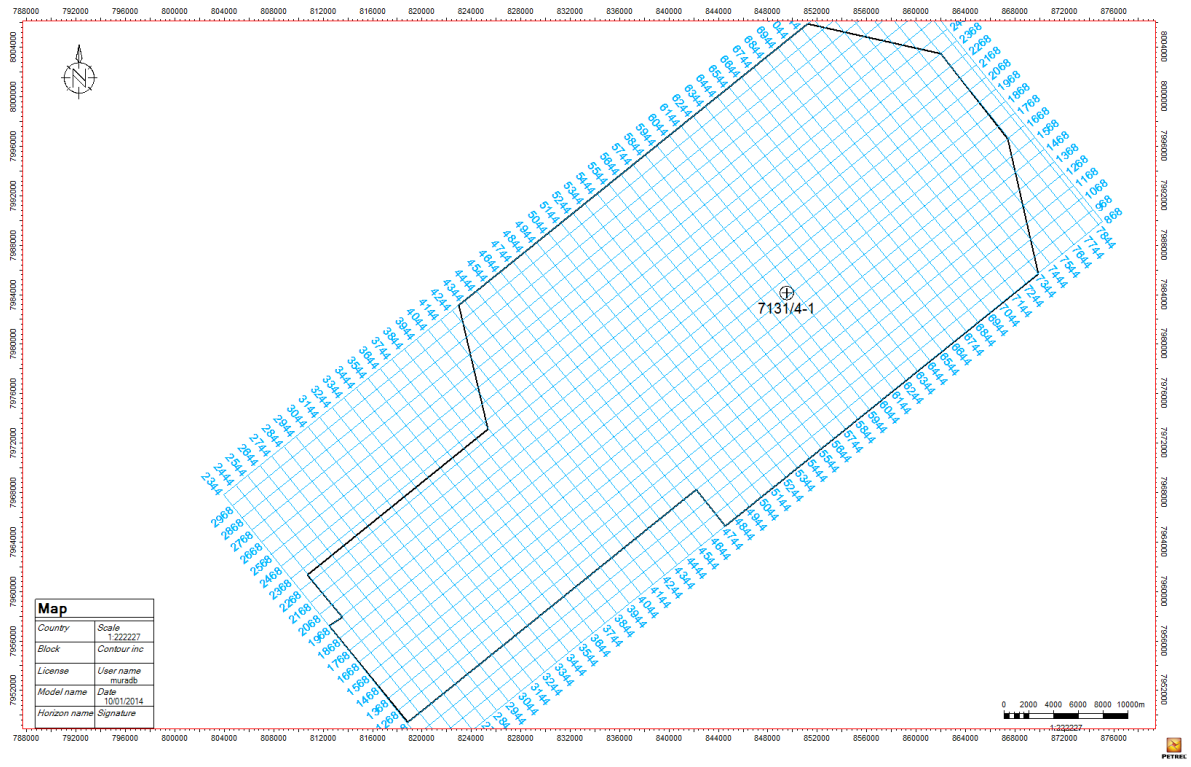

Figure 3.1: ST9802 — 3D seismic data. Available data is around 1500 km^2 described with black polygon. 7131/4-1 well is located inside the seismic data.

intervals for both inline and crossline are 12.5 m. The length is 69260.17 m for inline and

27423.95 m for crossline. Volume limits in processing grid are 868-3060 and 2323-7899 for inline and crossline, respectively. The volume is acquired in two-way travel time and has a geodetic system of ED50 UTM 35N.

Well number 7131/4-1 is the only well inside the area which is drilled by Statoil ASA (old) in the 2005 (Figure 3.1). The well comprises necessary standard wireline logs like GR, PEF, resistivity, neutron, density and sonic log. The distance between the rotary table and the sea surface is 25 m. The well has a total depth of 1295 m RKB and a water depth of 331 m at the well location. The bottom hole temperature is 45 $°C$ (NPD-Factpages, 2014).

Two commercial softwares were utilized for displaying, development and analysis of the data in this project. Petrel 2013.3 is the software which is used for well tie analysis, structural and stratigraphic interpretation of 3D data, mapping, attribute analysis and advanced interpretations like modeling and geobody extraction. Interactive Petrophysics 4.1 software was used for the basic log analysis module and displaying the data with log plots.

3.1 Polarity and Phase

The sea bottom reflection is a main indicator for determining the phase and polarity standards which are suggested by the Society of Exploration Geophysicists (SEG). Seismic polarity standards are divided into two types shown in Figure 3.2. If a reflection indicating an increase in acoustic impedance begins with a positive number (peak), it is the American (normal) polarity, while if it begins with a negative number (trough), it represents the European (reverse) polarity.

Zero and minimum phases are the main types of pulses used in the seismic data proposed by SEG. The onset of trough is interpreted for a minimum phase normal polarity wavelet. However, the center of peak is used for a zero phase normal polarity signal. Since zero phase is usually used in the seismic data, it is easy to interpret the center of peak and trough. The zero phase wavelet can achieve better resolution, because the shape of wavelet is symmetrical and the highest amplitude is recorded at the center of this wavelet.

In ST9802, seismic study demonstrated SEG zero phase normal polarity. This was concluded as the strong positive number (black peak) from the sea bottom interface

between sea water and sediments indicates an increase in acoustic impedance (Figure 3.2). The color variation of seismic data shown in the left-hand side of the figure depends on changes in amplitude related to physical characteristics of lithology and porosity.

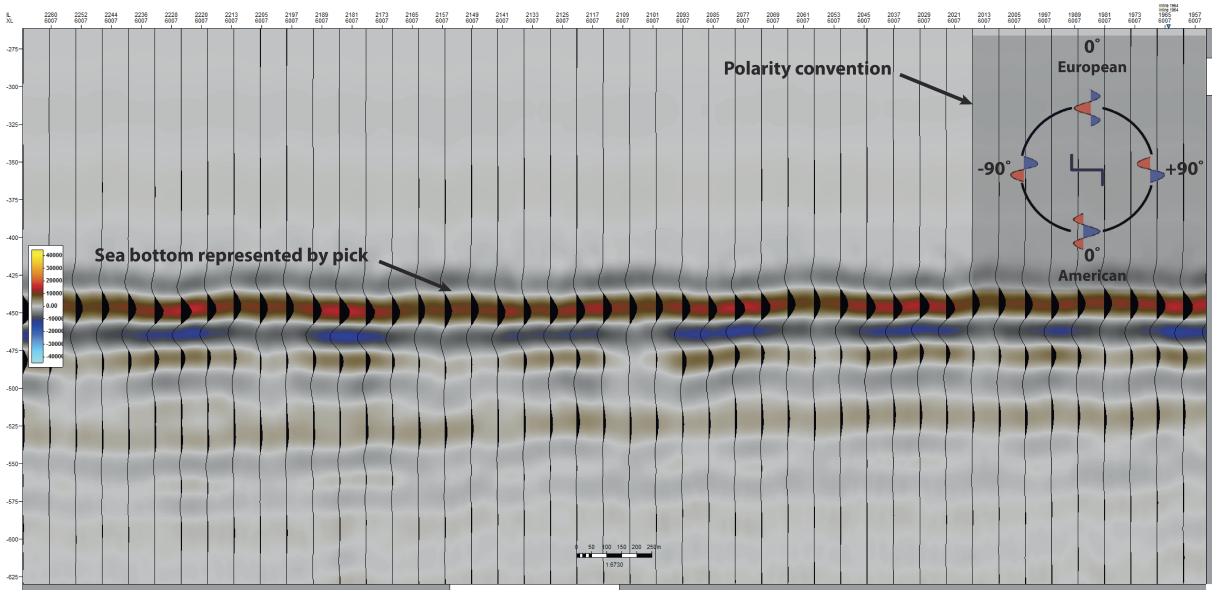

Figure 3.2: Seismic crossline (6007) displaying the seismic response related to the sea bottom represented by pick.

3.2 Seismic Resolution

The main purpose of the 3D seismic method is to obtain better resolution. The resolution of seismic data is measured in wavelength which is the proportional to the fraction of velocity/frequency. Velocity increases with depth due to more compacted sediments, whilst frequency decreases with depth because higher frequencies are quickly attenuated. Thus, the wavelength increases considerably with depth, creating lower quality resolution (Brown, 2004). The relation between these parameters is expressed as:

$$\lambda = v/f \tag{3.1}$$

where λ, v and f indicate wavelength, velocity and frequency, respectively.

Seismic resolution is very important factor for interpreters to see the details of geological features on seismic data. There are two types of resolution: the vertical resolution and horizontal resolution.

3.2.1 Vertical Resolution

The vertical resolution can be measured by considering the limit of separability which has an ability to differentiate the reflecting interfaces (top and base) of a thinning sedimentary bed (Bulat, 2005). The limit of separability is equivalent to a quarter of a wavelength (Brown, 2004, Bulat, 2005). The historic definition of this limit was provided by Rayleigh as the minimized interference effect at the half period separation between reflectors. This implies that for a bed with a thickness of $\lambda/4$, the interferences in the two boundaries of top and base will be tuned creating a strong reflector. For the case of thicker beds, overlapping the bed boundaries does not occur, and accordingly the vertical resolution is calculated by:

$$\Delta z = v/4f \tag{3.2}$$

where v and f represent the velocity and frequency, respectively (Sheriff and Geldart, 1995).

3.2.2 Horizontal Resolution

"Horizontal resolution refers to how close two reflecting points can be situated horizontally, yet be recognized as two separate points rather than one" (Yilmaz and Doherty, 2001). The Fresnel zone is defined to be the area on the reflector where is the source of the returned energy to the receiver through a half period (T/4) after the reflection starts (Bulat, 2005). Equation (3.3) presents the radius of the first Fresnal zone:

$$R_F = \sqrt{\lambda \cdot h_0/2} = v/2\sqrt{t/f} \tag{3.3}$$

where h_0 and v are the depth and average velocity. t and f are two-way travel time and frequency.

After comparing the equations (3.2) and (3.3), it is easy to conclude that both vertical and horizontal resolutions are directly proportional to frequency (Sheriff and Geldart, 1995).

Chapter 4

Methodology

This section provides the details of the methodology applied in this work. To start the analysis, the seismic and well data were loaded in the software as the inputs to carry out the seismic well tie analysis. The petrophysical analysis performed by the given well data was also the input for running the seismic well tie analysis. Afterwards, the seismic

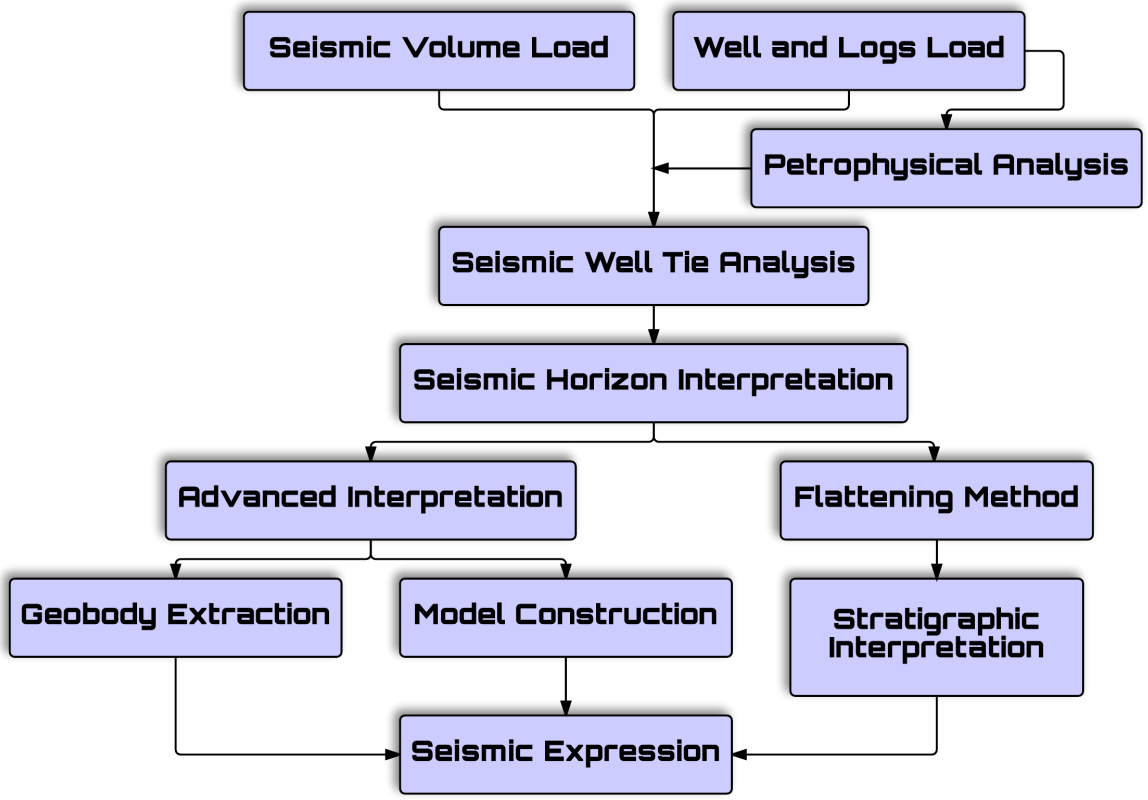

Figure 4.1: Thesis workflow is performed to achieve the proper image and to demonstrate the seismic expression of deep-water fan.

data was calibrated to well data prior to the interpretation of the horizons. Main parts of the study are Stratigraphic and Advanced interpretations. Stratigraphic interpretation is performed after flattening of seismic volume with seismic attributes. Attributes are also used in model construction which belongs to Advanced Interpretation. Creating a proper image and demonstrating the seismic expression of deep-water fan from the seismic volume are the main targets of this work. The summary of this workflow is shown in the flowchart provided in Figure 4.1.

4.1 Petrophysical analysis

Petrophysical analysis was performed using Interactive Petrophysics 4.1 software in the interval of 883 to 1260 m which covers upper Triassic formations, especially from Fruholmen to Kobbe. The software was mainly used for lithology analysis in this project.

The inputs of well data for the petrophysical analysis were gamma-ray, resistivity, density, PEF, neutron, sonic log and bottomhole temperature. Basic log analysis was realized to describe lithology and clay volume using wireline logs. The clay volume shown in Figure 4.2 was calculated through below equation as:

$$V_{clay} = (GR_{log} - GR_{clean})/(GR_{clay} - GR_{clean}) \tag{4.1}$$

where V_{clay} and GR are clay volume and gamma ray, respectively.

During lithology determination in the software, all the necessary correction procedures were followed to maintain the validity of the results.Thus, lithology information of Fruholmen, Snadd and Kobbe formations in well 7131/4-1 were obtained which is shown in Figure 4.2.

4.2 Depositional environment

4.2.1 Fruholmen formation

The core description of the well in the Fruholmen formation is demonstrated with log plot obtained by petrophysical analysis in Figure 4.3. Medium-, coarse-grained and mainly clay poor sandstones exist within the 10 m interval in the lowermost part of the selected core. The thickness of single beds is a few hundreds of millimeters. These beds consist of current

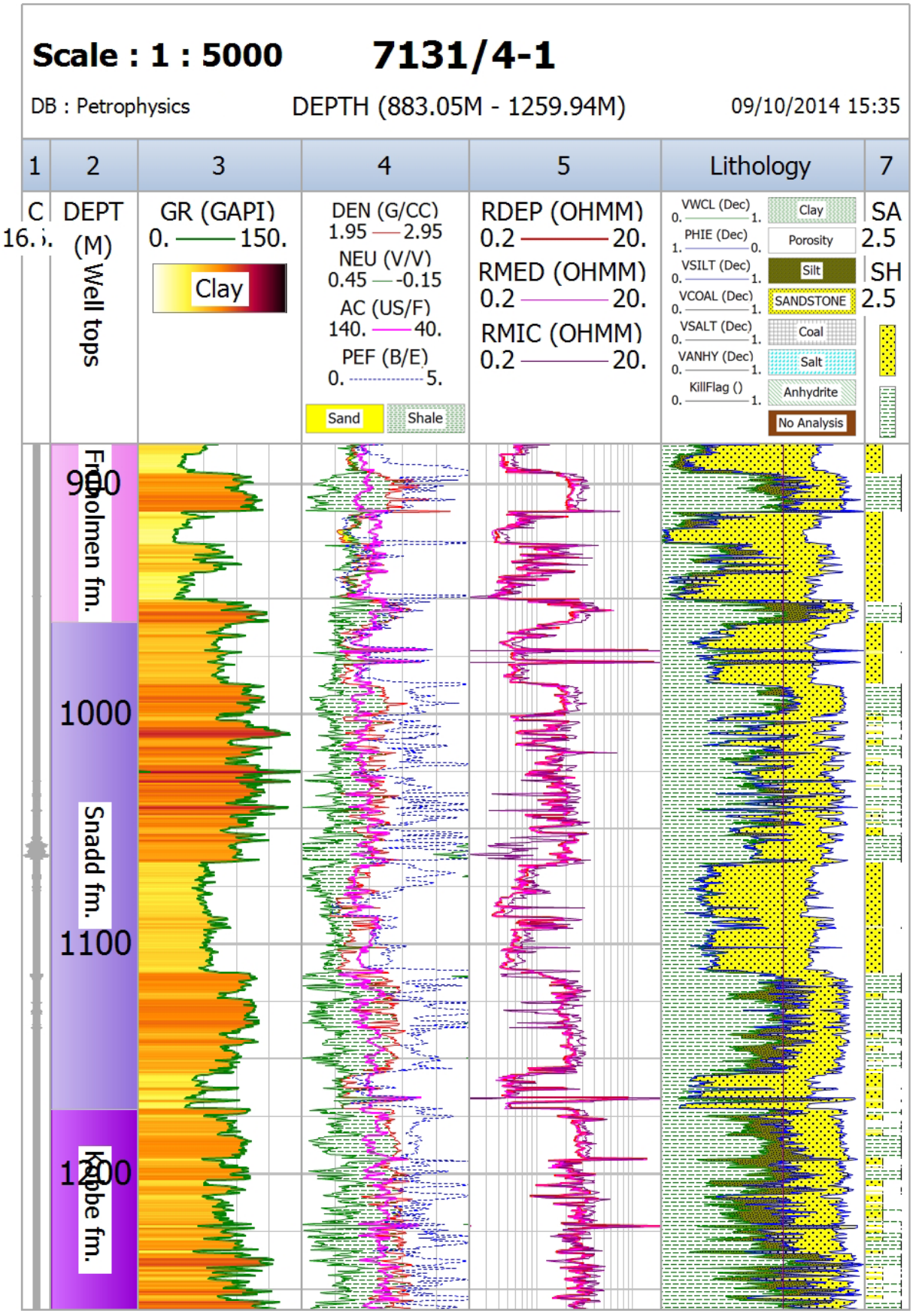

Figure 4.2: Log analysis of well 7131/4-1. Log plot performed in Interactive Petrophysics (IP) covers approximately depth of 377 m from Fruholmen to Kobbe formation (for log plot of each formation, see Appendix A).

ripples and are cross-bedded with bioturbation and coal or plant particles. This interval of core contains numerous fining-upward units of sandstones. The depositional environment is most likely tidal or fluvial channels. Above this interval, the sandstones from 934.5 to 925 m are mud-rich where approximately 1 m thick fine- and medium-grained sandstones are interbedded with siltstones and very fine-grained mud-rich sandstones. The wave ripple sandstones with bioturbation were also observed in this muddy interval. This interval was interpreted as sandy bay or lagoon deposits with crevasse splays and small mouth bars. 6 m fining-upward unit of coarse- and medium-grained sandstone with coal particles in large foreset beds overlie the bay or lagoon deposits. Erosion is likely to happen at the base of this unit. The deposition is possibly a fluvial channel at the interval of 925-919 m. The sandstone of fluvial channel is covered by 4 m partly mud-rich very fine and fine-grained thin sandstone beds (0.1-0.5 m) with some bioturbation structures and current ripples. Top side of this interval represented infilling of abandoned fluvial channel (Walderhaug, 2012).

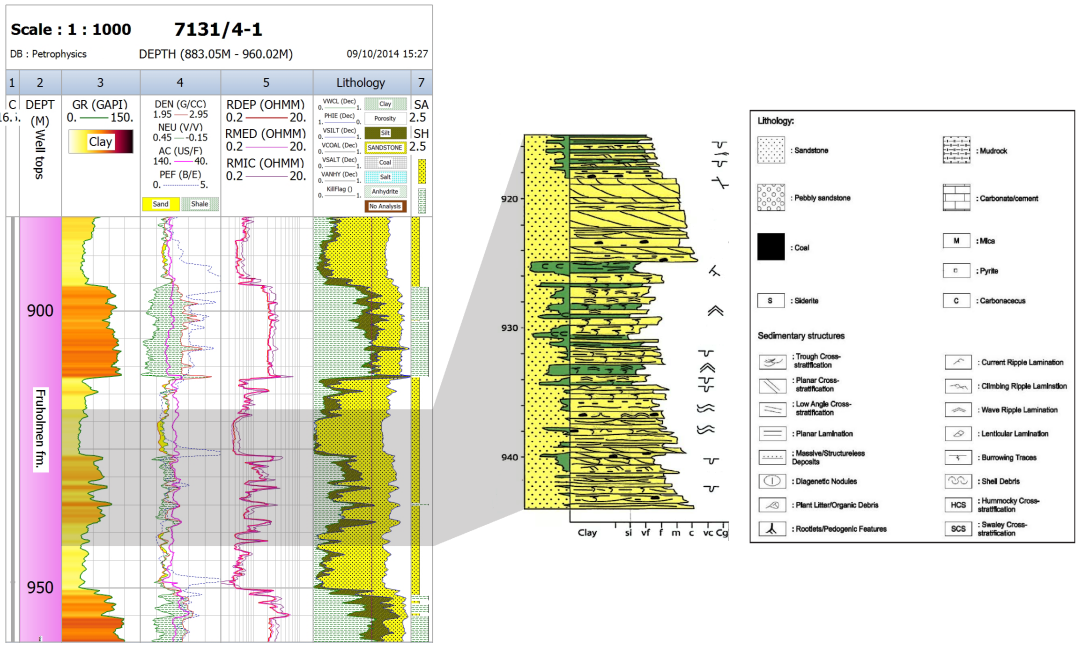

Figure 4.3: Log plot performed in IP and core description (modified from Walderhaug, 2012) of Fruholmen formation in the well 7131/4-1.

4.2.2 Snadd formation

The core description of the well in the Snadd formation is demonstrated with log plot obtained by petrophysical analysis in Figure 4.4. The lower interval of the core was

categorized by mud-rich sandstone and mudstone with siderite concretions demonstrating

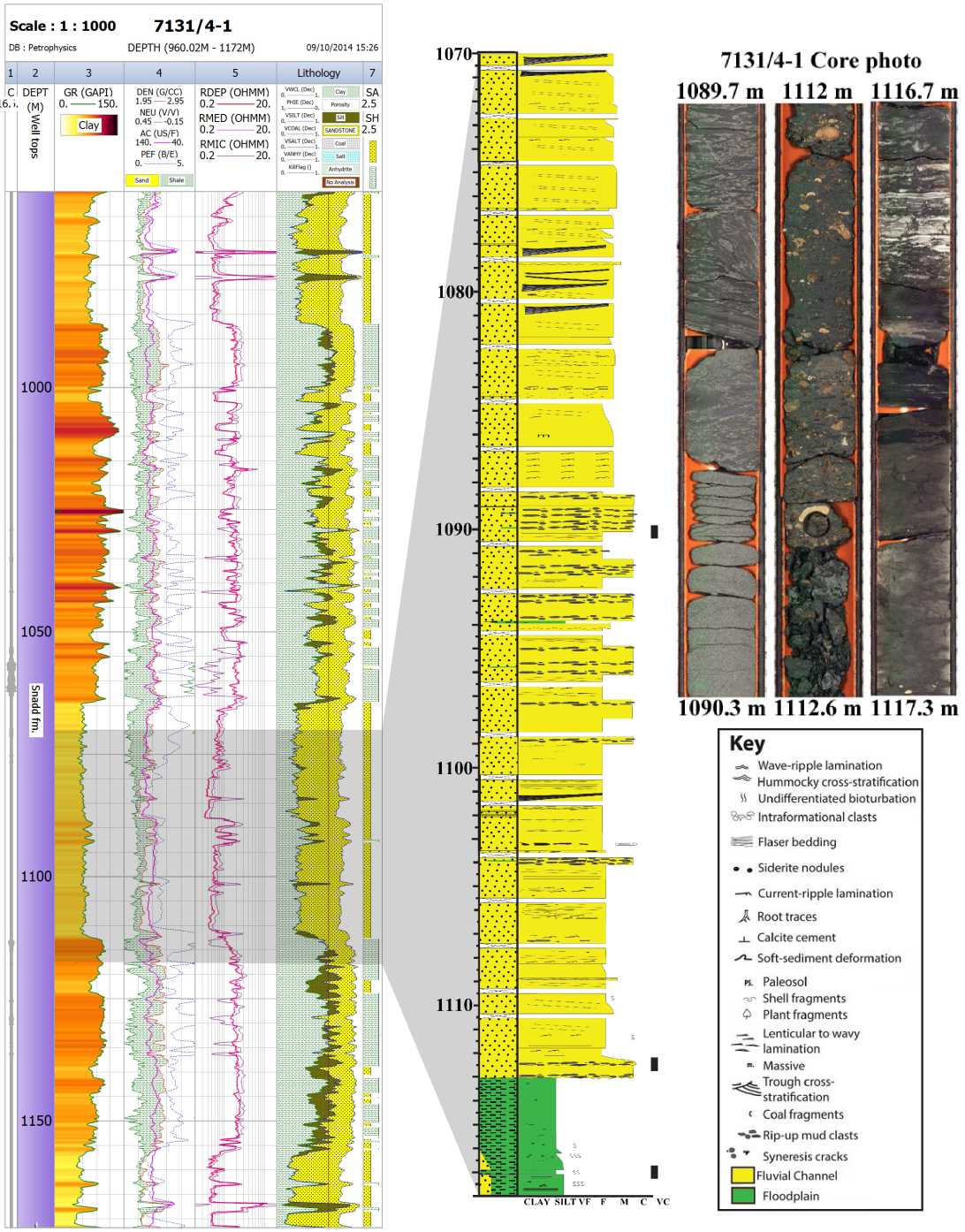

Figure 4.4: Log plot performed in IP, core description and photo (modified from Klausen et al., 2014) of Snadd formation in the well 7131/4-1.

water-saturated paleosol and lake-flow swamp environments. Above this interval, an erosive based thin coarse- to very coarse-grained sandstone with irregular shaped interclasts is most likely a channel-lag deposit. The upward level of 4 m thick trough cross-bedded medium-grained sandstone was interpreted as a channelized dunefield. The interval of 1108-1104 m is dominated by medium-grained sandstone with laminated carbonaceous.

Further upward 20 m thick level of 1104-1084 m was interpreted as a medium- and coarse-grained sandstones with some tabular and trough cross-bedding. A lot of mud- and sand-rich fragments of clastic sediments with some current ripples are also shown at this level. The uppermost 14 m interval indicates a mostly medium- and coarse-grained trough and tabular cross-bedded sandstone with some calcite and siderite cementations. The channel environment in estuarine setting with in-channel dunes and bars was confirmed at 1108-1104 m, 1104-1084 m and 1084-1070 m intervals (Walderhaug, 2012).

4.3 Seismic Well Tie Analysis

The next step was to accomplish the seismic to well calibration after loading the seismic survey and well data. To do this calibration, it was needed to develop a synthetic seismogram. The development of synthetic seismogram was based on four main steps in this project: sonic log calibration, seismic wavelet extraction, synthetic seismogram generation and integrated seismic well tie.

The spike values were removed from the sonic log using despiking tool prior to sonic calibration (Figure 4.5). Sonic calibration was performed by adjusting the sonic values between checkshot points. This process was continued until the integrated sonic times coincided with those from the checkshot. The aim of sonic calibration method was to make a relationship between well depth and time for

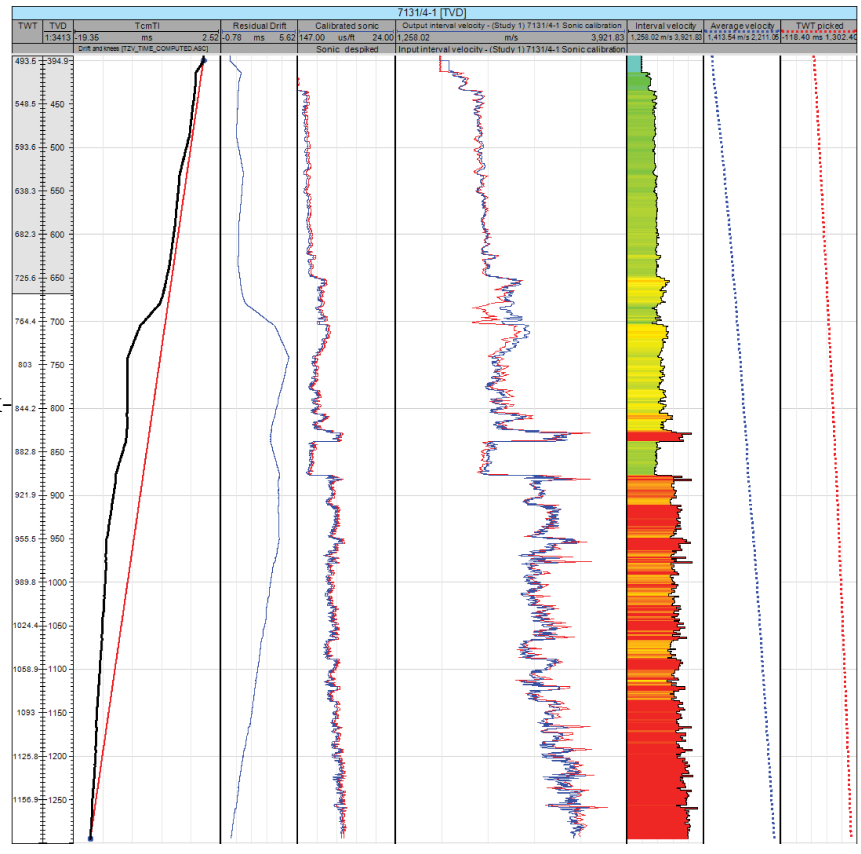

Figure 4.5: Sonic log calibration.

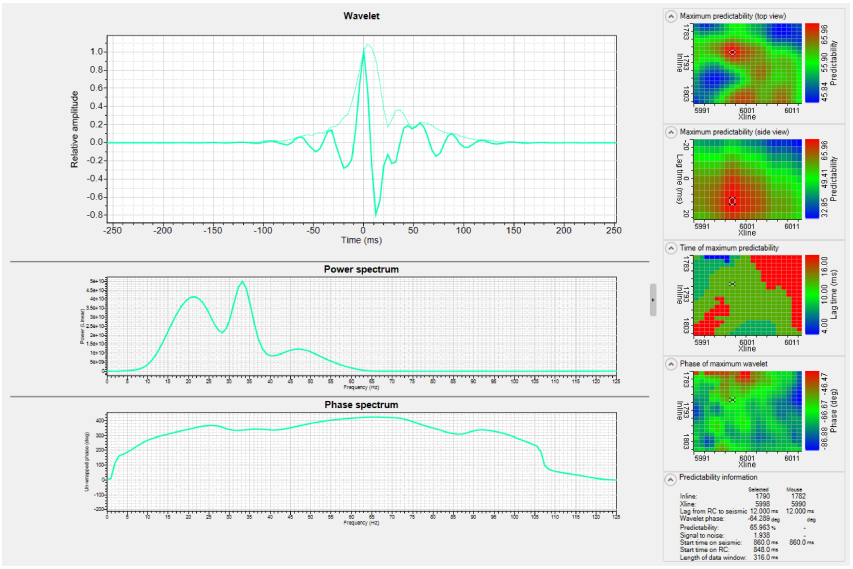

Figure 4.6: Features of the seismic wavelet. The wavelet is extracted from seismic close to well, demonstrating a good percentage of predictability to be applied in the synthetic seismogram generation.

the well shown in Figure 4.5.

After developing the sonic calibration, the wavelet extraction is necessary in prior to the synthetic seismogram generation. In Figure 4.6, a wavelet was extracted directly from the seismic close to well. The wavelet displayed a positive zero phase, and the dominant frequency was in range of 21 to 33 Hz. Thus, the extracted wavelet demonstrated a good percentage of predictability which was above 60. It means that there is a good relationship between the seismic around the well and the reflection coefficient, considering Inline-crossline positions, the lag time and wavelet phase.

If the sonic log is correctly calibrated, and the best wavelet is extracted, the synthetic seismogram can be constructed. It is necessary to use the convolutional model to construct the synthetic seismogram. A basic assumption of this model for stacked seismic trace can be written as a convolution between a wavelet and reflection series:

$$y(t) = w(t) * f(t) \tag{4.2}$$

where $y(t)$, $w(t)$ and $f(t)$ denote recorded seismic signal, input signal and impulse response of the Earth, respectively.

The density and sonic logs are necessary for calculation of the acoustic impedances of various layers used to estimate the reflection coefficient on that interface. The equation of the reflection coefficient is described as a function of acoustic impedance:

$$RC = (AI_i - AI_{i-1})/(AI_i + AI_{i-1}) \tag{4.3}$$

where RC and AI_i are reflection coefficient and acoustic impedance, respectively.

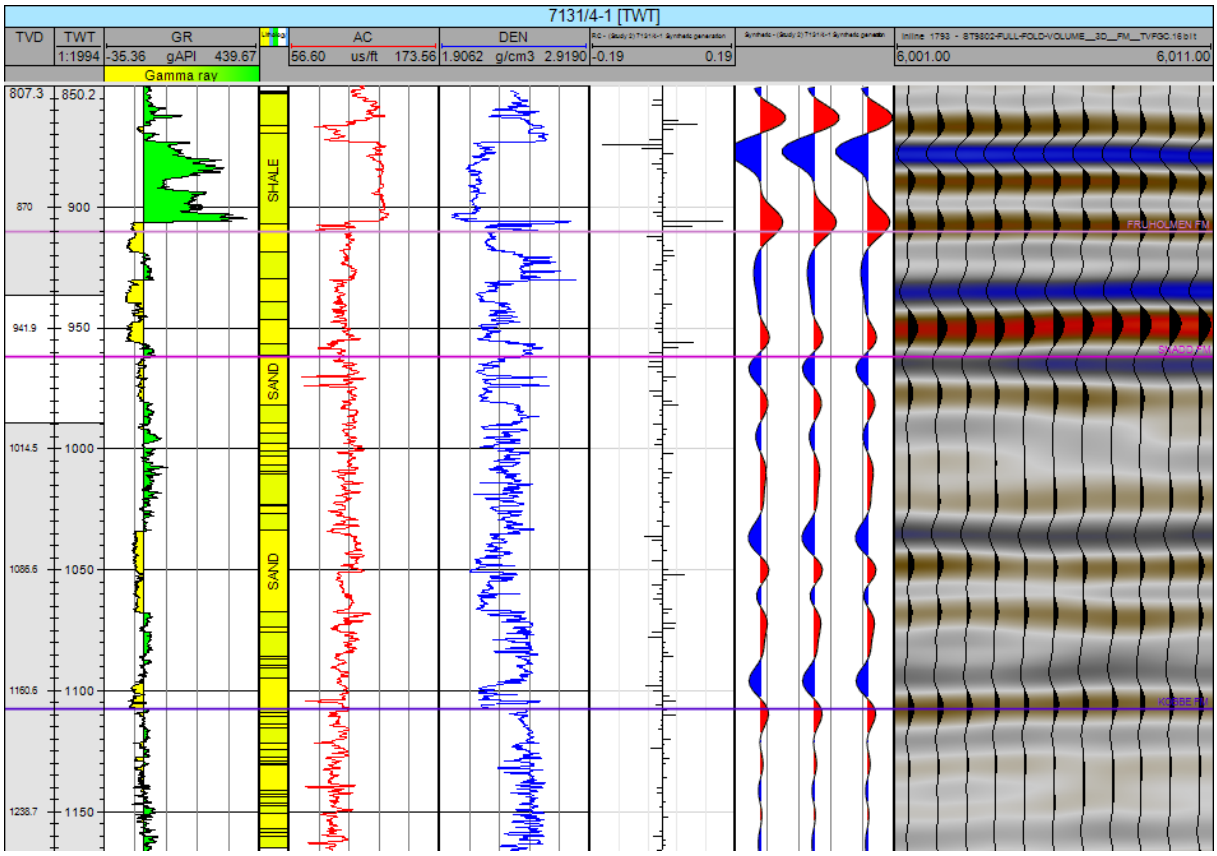

Figure 4.7: Synthetic seismogram. Wavelet is generated from the seismic data, indicating a good relation between seismic and well data. Sand and shale in lithology column are represented by yellow and green colors, respectively.

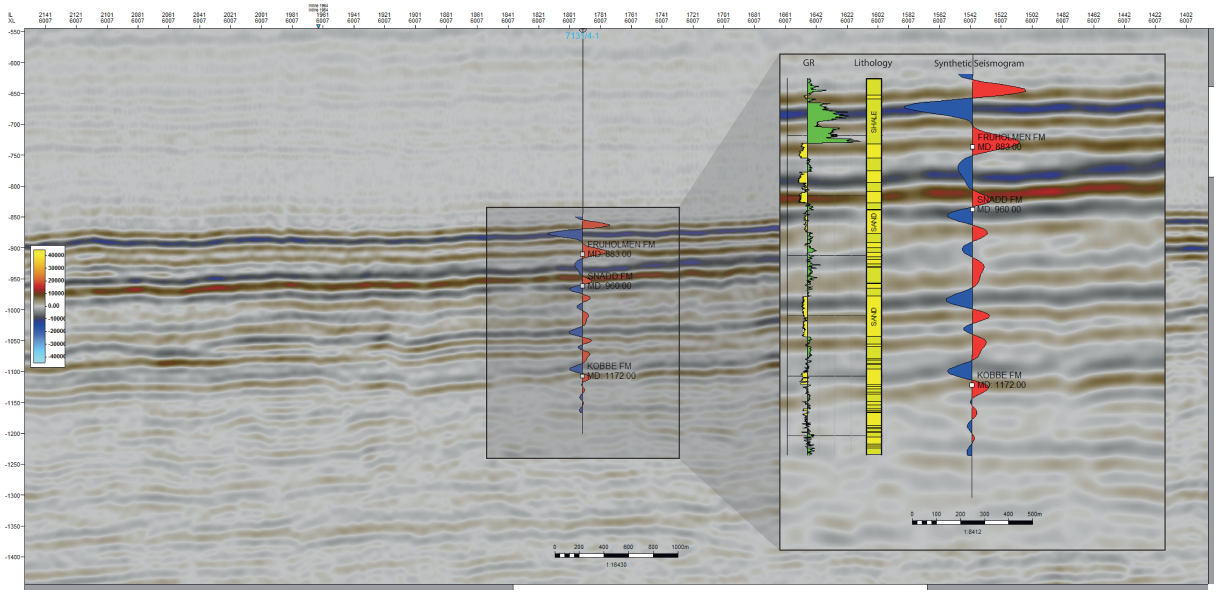

Figure 4.8: Synthetic seismogram in the well location. The relation between reflection series and seismic section (crossline 6007) demonstrated a good match (for details of GR and lithology column, see Figure 4.7).

In this study, output of the synthetic seismogram showed a very good match with seismic data in the area close to the well (Figures 4.7 and 4.8). It means that the well data is almost perfectly tied to the geological markers. Good match between seismic data and synthetic seismogram is necessary for proper correlation of the stratigraphy in the well.

4.4 Seismic Horizon Interpretation

After properly calibrating the seismic data with well, the horizon interpretation was carried out. It is necessary to choose the desired horizons before starting the interpretation. Firstly, two horizons of upper Triassic age which are the top of Fruholmen and Kobbe formations (Figure 4.9) were interpreted based on the geological markers that had been provided by the Norwegian Petroleum Directorate (NPD). Afterwards, although the well was not penetrated to the lower Triassic age, I extended my work into this level interpreting two horizons (Intra Lower and Base Triassic) as shown in Figure 4.10 which was the main focus of the study.

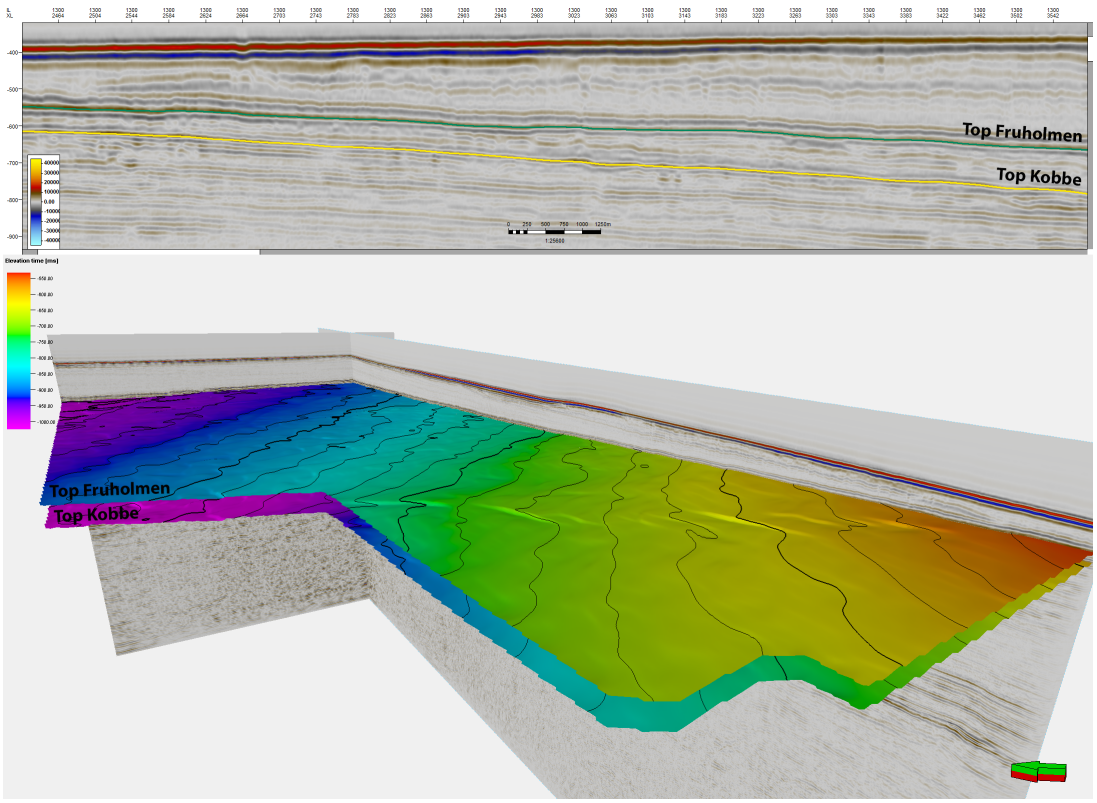

Figure 4.9: Surface maps shown in 3D are created based on Top Fruholmen and Top Kobbe horizons which are illustrated in the section (inline 1300) with green and yellow colors, respectively.

Two auto tracking and manual interpretation methods were used in this project. The strong and continuous seismic reflections were interpreted by auto tracking whereas another method was applied when the reflections were not clearly visible on the data. Assuming the same thickness between the horizons was necessary for accurate interpretation.

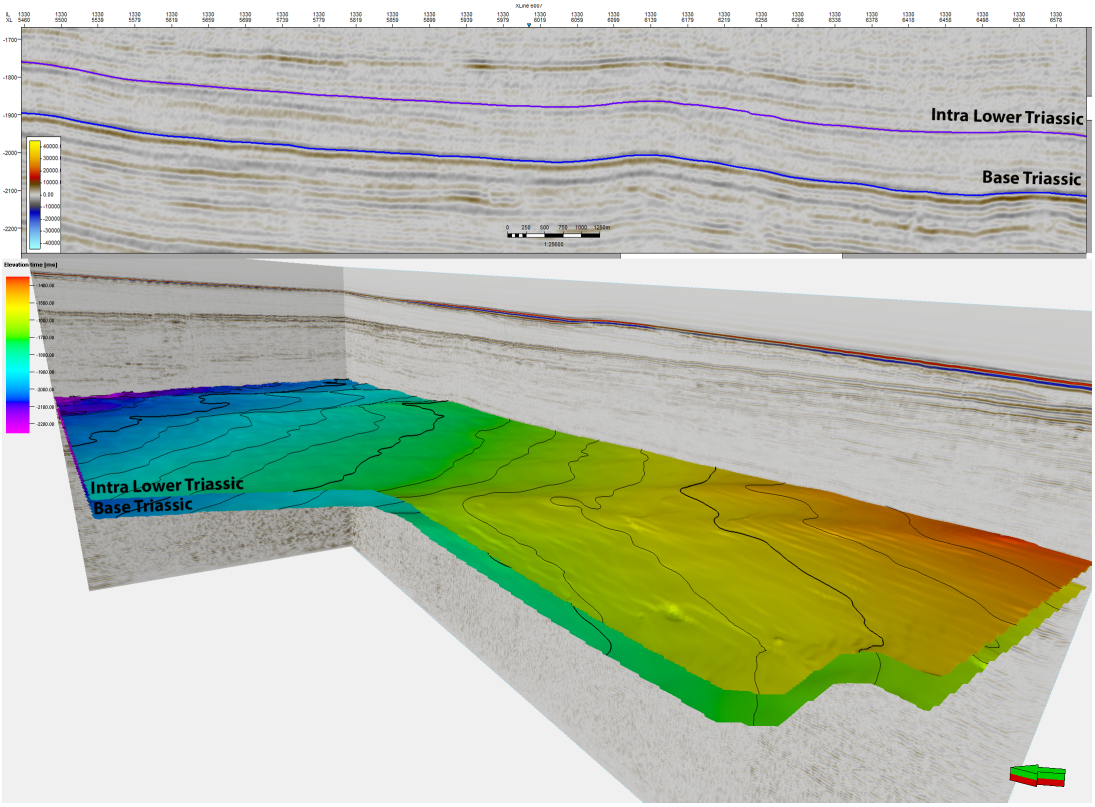

Figure 4.10: Surface maps shown in 3D are created based on Intra Lower and Base Triassic horizons which are illustrated in the section (inline 1330) with purple and dark blue colors, respectively.

4.5 Flattening Method

After interpreting the horizons, the flattening method was performed prior to stratigraphic interpretation. This method which can be used to provide more detailed information about the stratigraphic features was carried out considering two seismic surfaces: Top Fruholmen and Intra Lower Triassic (see Figures 4.9 and 4.10). These seismic surfaces were used as the inputs for flattening of the seismic data. Seismic amplitudes were performed using this flattened data with the aim of identifying anomalies associated with upper and lower part of the Triassic ages. The workflow of flattening method shown in Figure 4.11 was followed to realize stratigraphic interpretation. Using the method, the stratigraphic events were

seen on a flat surface. In addition, the effects of structural elements were neglected.

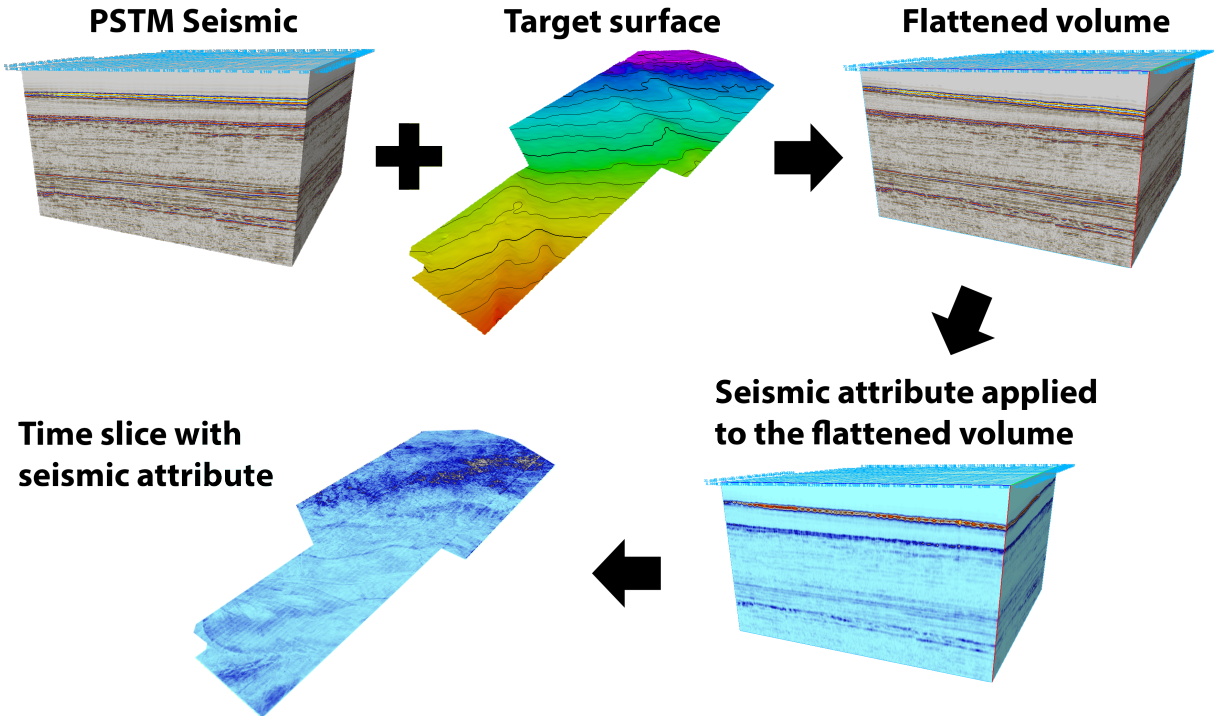

Figure 4.11: Workflow of flattening method used in stratigraphic interpretation.

Chapter 5

Results

5.1 Stratigraphic Interpretation

The considered seismic volume was flattened using target horizon to generate a flattened volume with seismic attribute that is shown as the workflow in Figure 4.11. After flattening the conventional volume, various seismic attributes were applied which among them, it was only RMS attribute that gave a reasonable outcome. For the results of the other implemented seismic attributes, the reader is referred to Appendix B.

RMS attribute is one of the seismic attributes mostly used in this project. The geological features can be isolated from the background features by amplitude response. Resultant time slices of flattening method (Figure 4.11) can reveal geomorphology and flow direction of the channel systems which were distinguished by high amplitude demonstrated in dark blue. However, the low amplitudes demonstrated by light blue in the figures, refer to floodplain surfaces.

Figure 5.1 illustrates the result of flattened volume for the time slice of -816 ms. This seismic flattened volume was created based on the Top Fruholmen horizon with Variance and RMS attributes; it made it possible to interpret the minor faults with NW–SE trend. The fault system in the area was controlled by extension, i.e., the minor faults were characterized as normal faults. A set of polygonal faults could also be detected throughout the area. Although Variance attribute was not the right option for detecting the stratigraphic features, sinuous and erosional channels could be observed in the southwestern part of the area. Erosional channel system can be proved by either identifying its shape on seismic section or on the time slice. Figure 5.2 illustrates the result of flattened

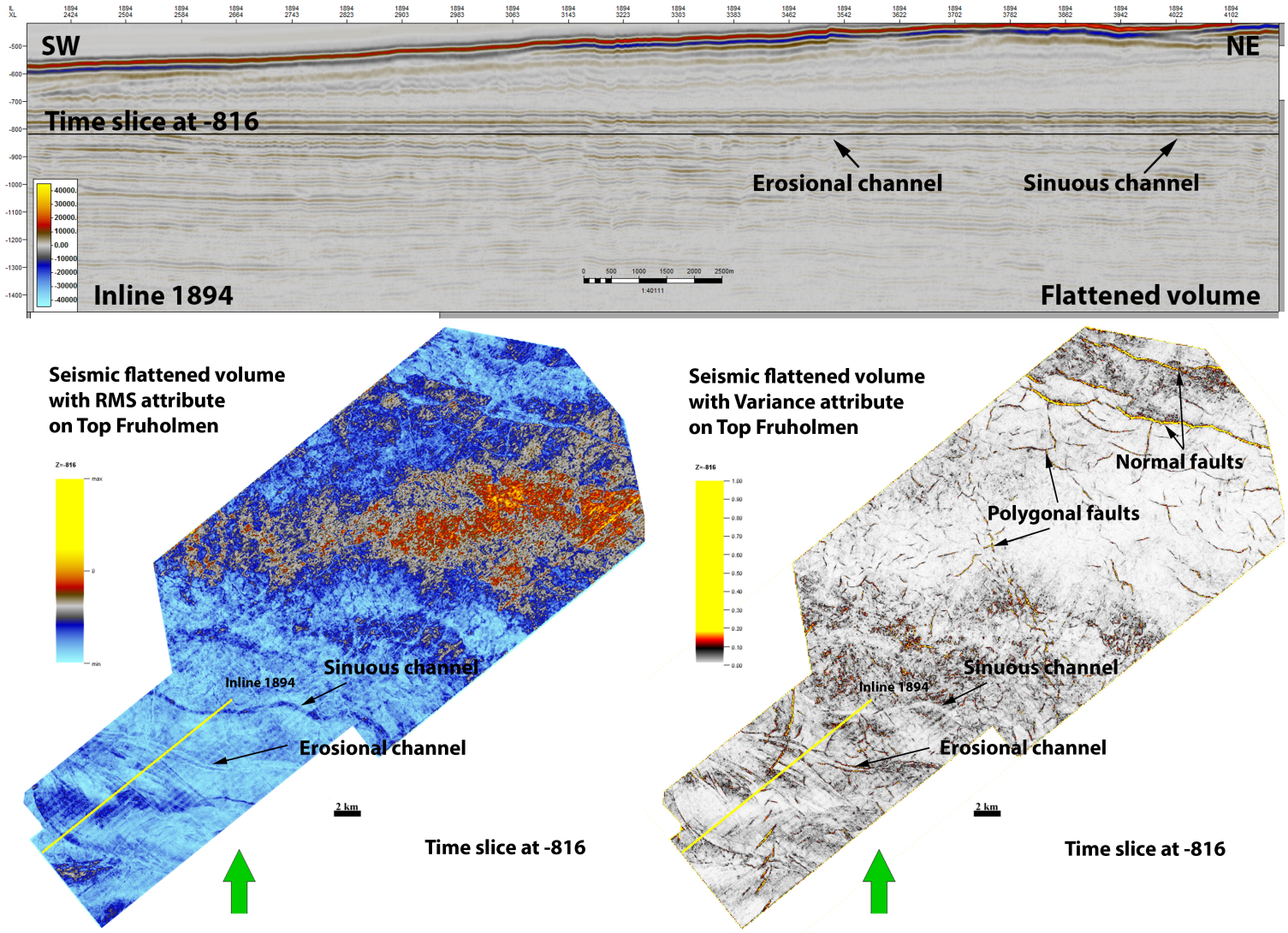

Figure 5.1: Time slice at -816 *ms*. Flattened seismic section and flattened volume with Variance and RMS attributes on Top Fruholmen horizon. Thereby, minor normal and polygonal faults are interpreted. Sinuous and erosional channels are either detected on the seismic section or on the time slice.

volume for another time slice (-864 ms). Thus, the high amplitudes were recorded due to the meandering channels distributed in the area. Previously described minor faults with Variance attribute were seen in this image as well. The result of flattened volume at -928 ms time slice is shown in Figure 5.3. Thus, the high amplitude anomalies were interpreted in the area. Relatively older and younger channels were the reason for these anomalies. Younger channel was not well recorded in this time slice, while the older channel was inferred as major channel deposits. According to Klausen et al., 2014, the channel deposits were interpreted as the products of trunk rivers. These deposits were cut by the minor normal faults. The result of flattened volume at -968 ms time slice is depicted in Figure 5.4. Thereby, the distribution of high amplitude anomalies were interpreted that belong to three various meandering channels which were in the southwestern side of the area.

The seismic flattened volume for time slices at -816, -864, -928 and -968 ms was generated based on the Top Fruholmen horizon with RMS attribute. Based on observation of the cross sections and time slices from figures 5.1 to 5.4, the data has confirmed the existence of fluvial channel systems considering their geometry, distribution and stratigraphic information.

Figure 5.5 illustrates the result of flattened volume at -1916 ms time slice. This seismic flattened volume was created based on the Intra Lower Triassic horizon with RMS attribute. Thus, it was likely to interpret the distribution of high amplitude anomalies in the area. These anomalies belong to deep-water fan system. The amplitude of this system was varied in SW-NE direction. From the seismic section (inline 1430), channels categorized by continuous and discontinuous high amplitude seismic reflections were interpreted to be sand rich, while the low amplitude reflections considered to be mud rich. One irregular shaped pattern was detected in the southwestern side of the area that was interpreted as a carbonate build-up well described by Colpaert et al., 2007.

5.2 Advanced Interpretation

5.2.1 Model Construction

After flattening of Intra Lower Triassic surface, the deep-water fan was defined. Then, new Intra Lower Triassic 1 (thin yellow) horizon (Figure 5.6, A-A') was interpreted using the same horizon interpretation methods. Creating surface map with RMS attribute

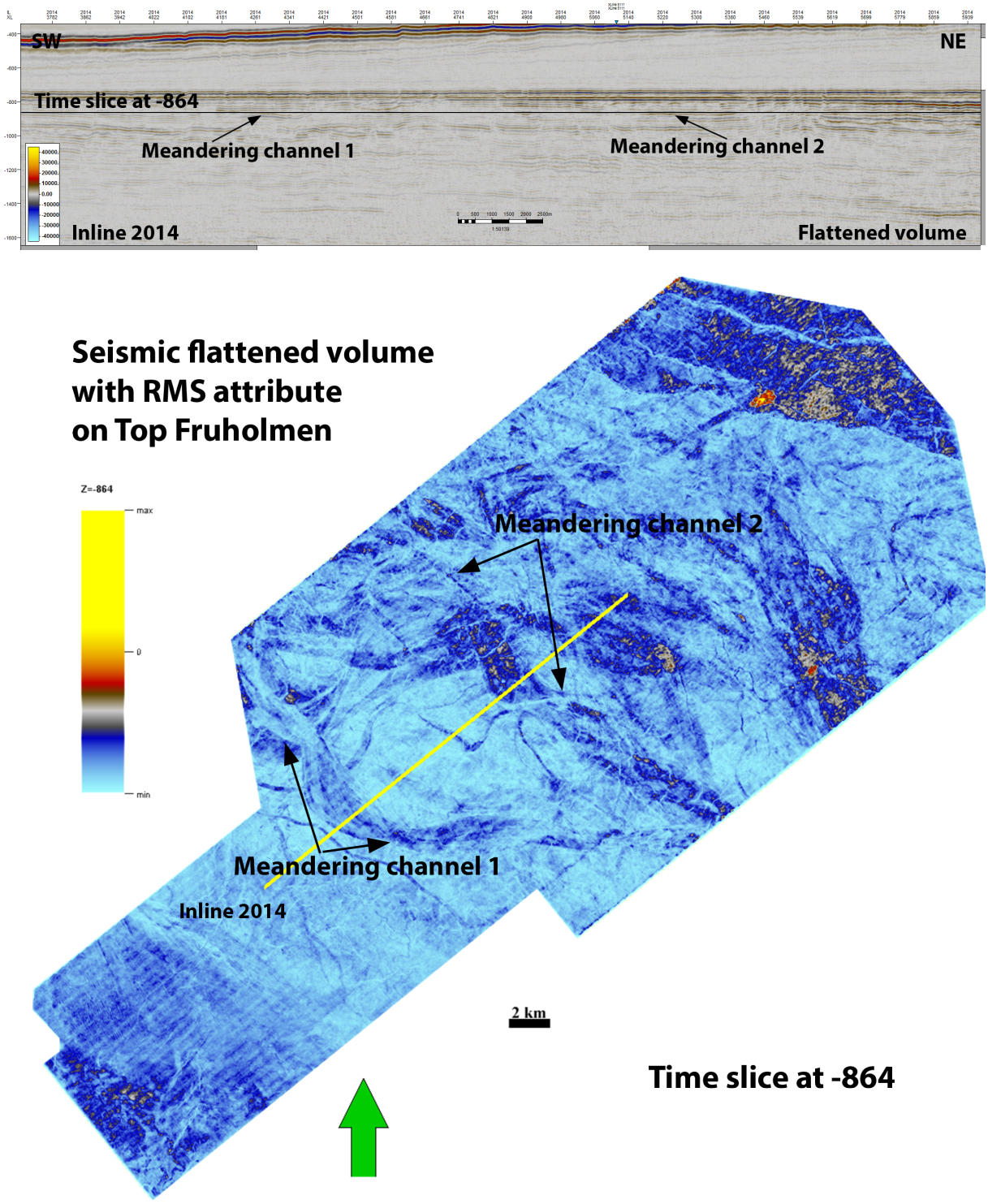

Figure 5.2: Time slice at -864 ms. Flattened seismic section and flattened volume with RMS attribute on Top Fruholmen horizon. Thus, amplitude anomalies are recognized in the area associated with two meandering channels.

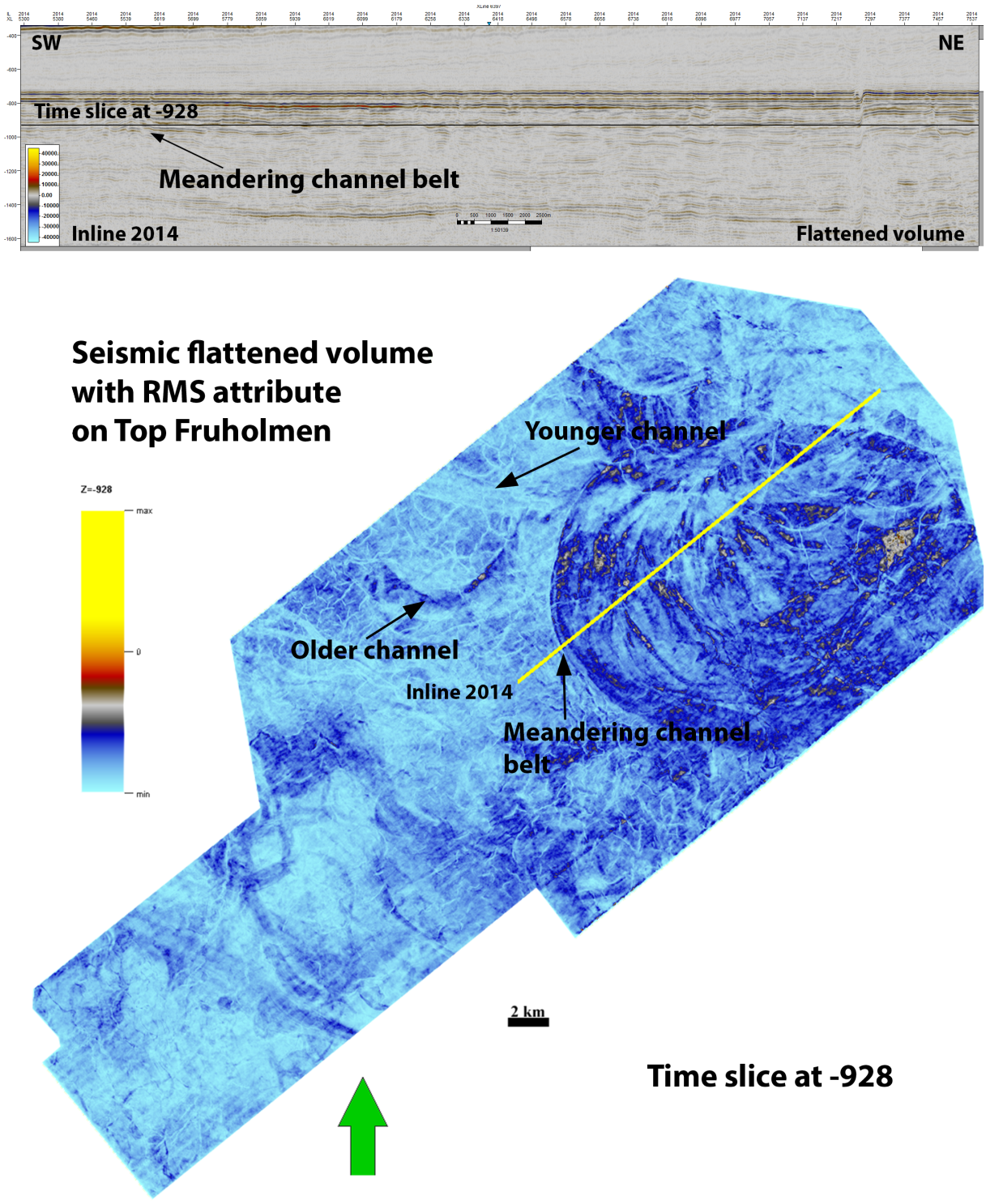

Figure 5.3: Time slice at -928 ms. Flattened seismic section and flattened volume with RMS attribute on Top Fruholmen horizon. The amplitude anomalies are identified related to older channel with meandering belt and younger channel. In this image, it is not easy to follow younger channel. Meandering channel belt can be seen by either on the seismic section or on time slice.

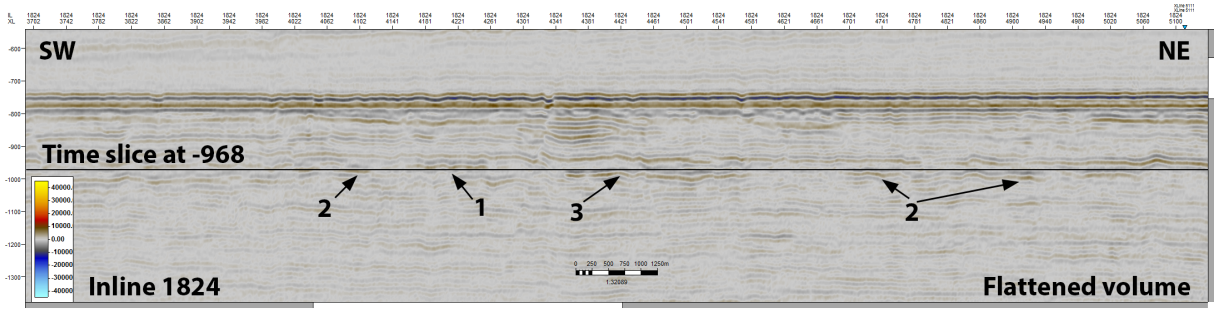

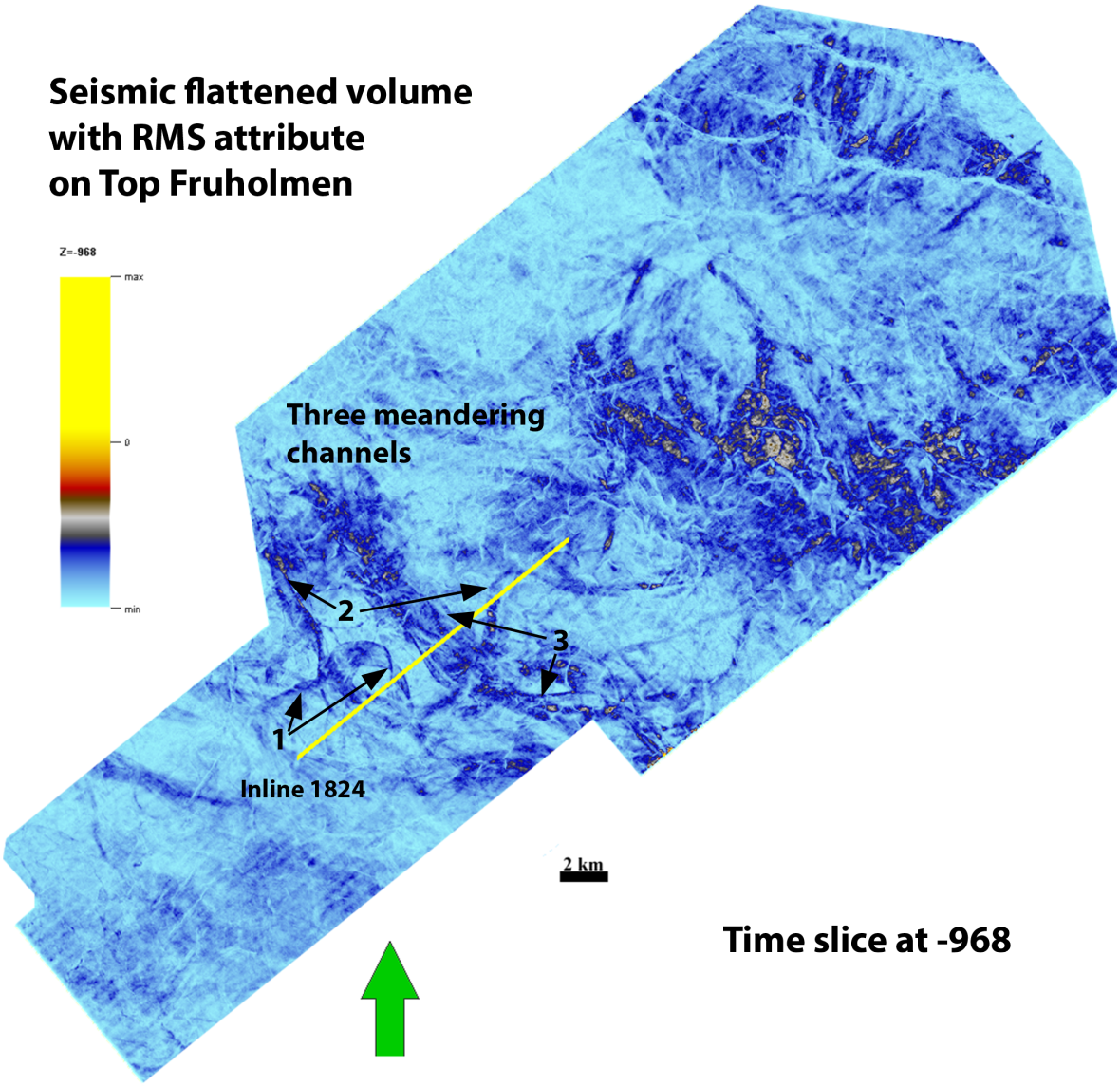

Figure 5.4: Time slice at -968 ms. Flattened seismic section and flattened volume with RMS attribute on Top Fruholmen horizon. Thereby, the three meandering channels are interpreted due to the amplitude changes in the area.

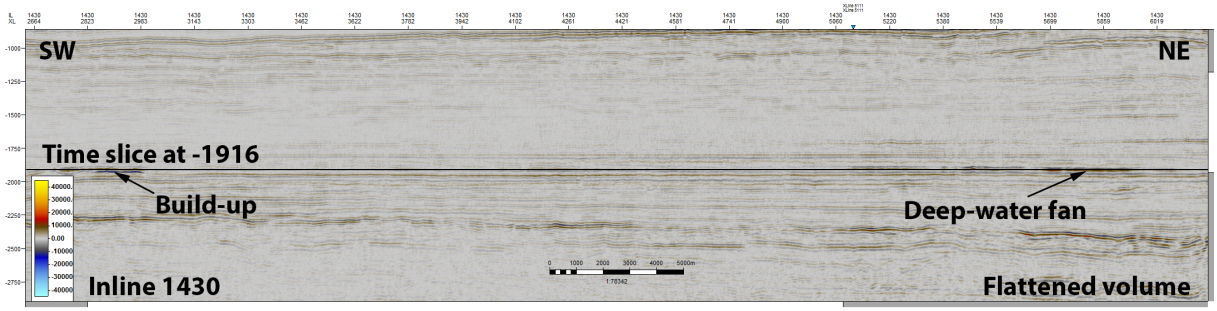

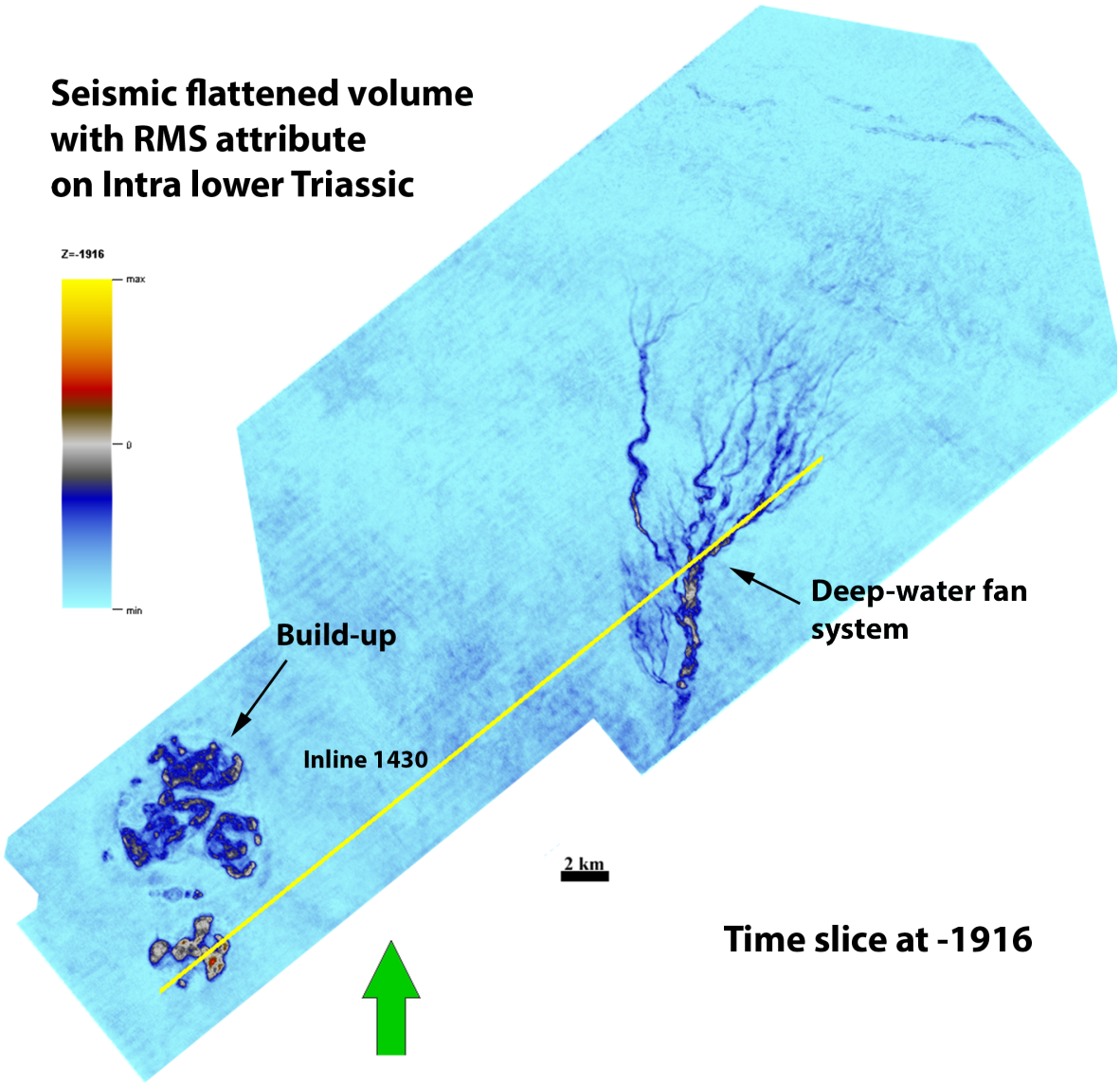

Figure 5.5: Time slice at -1916 *ms*. Flattened seismic section and flattened volume with RMS attribute on Intra Lower Triassic horizon. Thus, amplitude anomaly was detected in the middle of the area which is associated with deep-water fan system. Irregular shaped pattern was imaged on the southwestern part of the area and interpreted as a build-up.

was the next step of the analysis. This surface attribute map indicates similar result as the time slice extracted by flattened volume. RMS map also proves the architecture of the deep-water fan separated from the background features by amplitude responses. Figure 5.7 shows the model of cutting a seismic volume. This model was made out of the area between two surfaces of the volume. The Intra Lower Triassic 1 and Base Triassic surfaces were the main inputs to this model together with Relative Acoustic Impedance volume attribute. From the model, it can be seen that the deep-water fan is deposited in different stages, since the main channel is not meandering compared to secondary single channel. This main compacted channel is most likely feeder channel. Shadow patterns in RAI model can be explained as the noise obtained from the poor data quality and interpretation process.

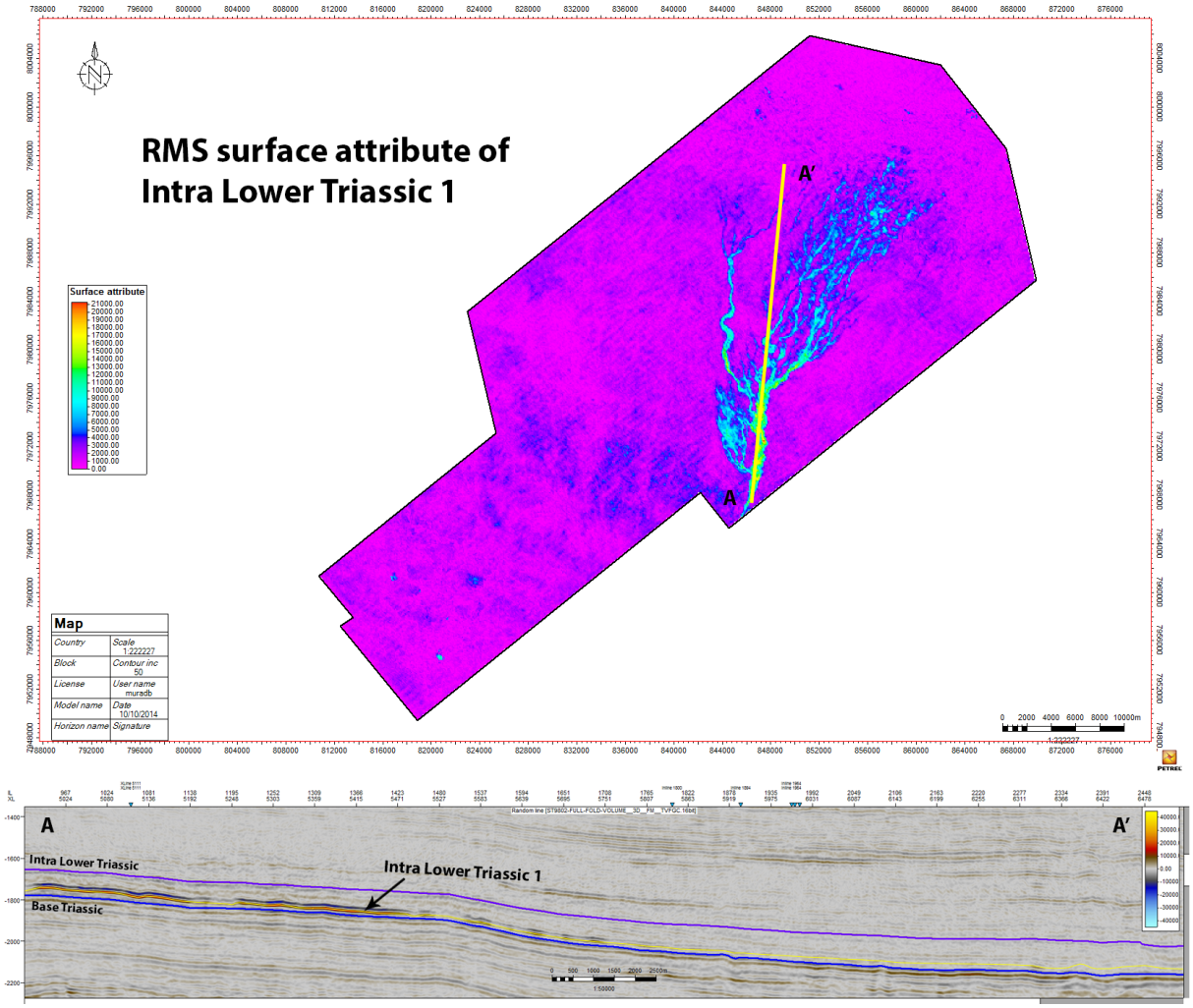

Figure 5.6: RMS attribute map is created based on interpretation of new Intra Lower Triassic 1 horizon shown by thin yellow color on A-A' composite line (for other seismic attributes, see Appendix C).

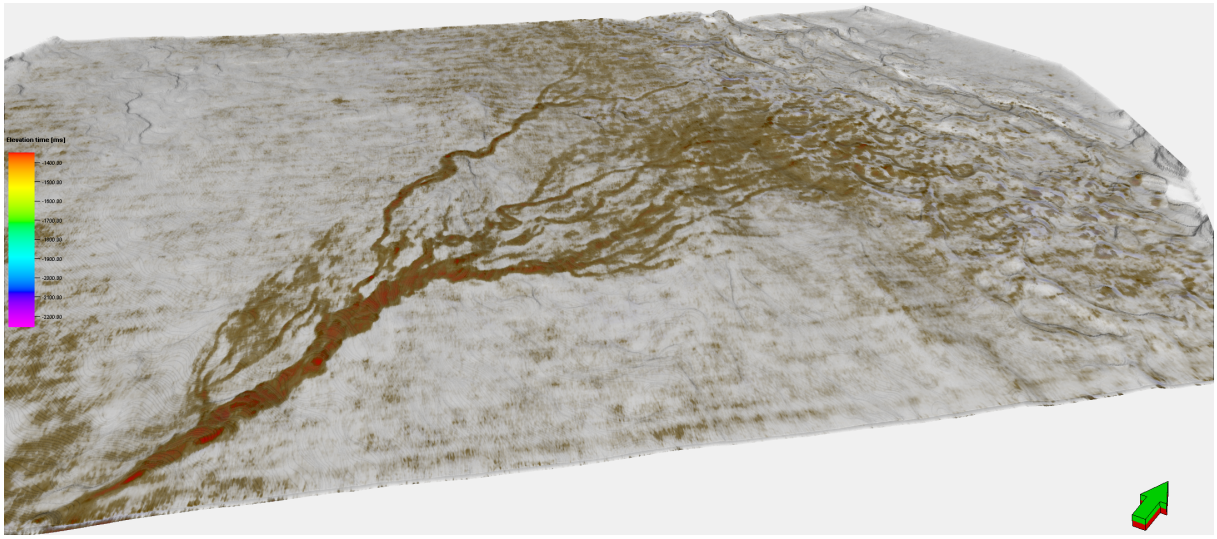

Figure 5.7: The model construction based on Relative Acoustic Impedance (RAI) volume attribute.

5.2.2 Geobody Extraction

Geobody extraction of the deep-water fan was the next step of this project performed to isolate and extract the features of the seismic volume. The RAI model was used for the extraction of this geobody. 3D view of geobody with seismic sections and RMS attribute map helps in a thorough understanding of the geomorphology illustrated in Figure 5.8. Some noises which are discussed in RAI model are also visible on geobody extraction.

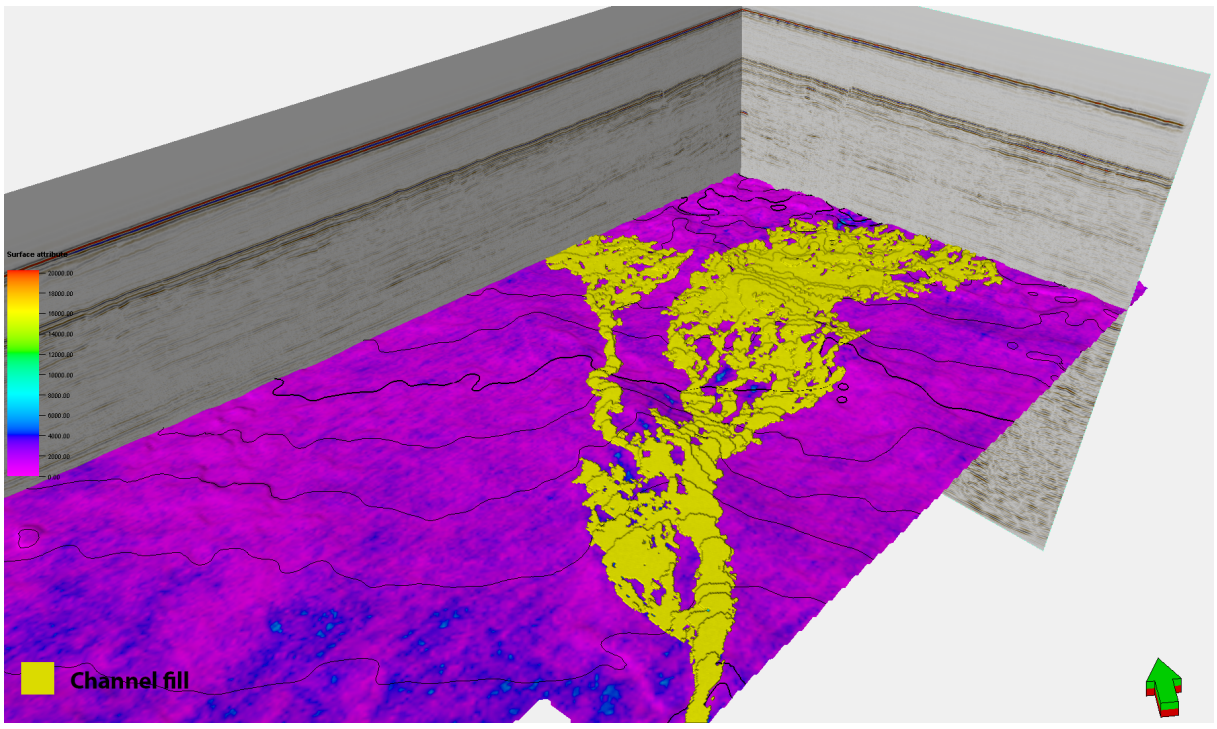

Figure 5.8: 3D view of geobody extraction integrated with the seismic sections and RMS surface map.

Chapter 6

Discussions

6.1 Challenges

Several time slices were extracted using flattening method in Upper and Lower Triassic intervals. This method was performed for Fruholmen and Intra Lower Triassic surfaces. Among the analyses done, the one with RMS attribute showed to be quite promising in determining different stratigraphic features which were isolated by amplitude anomalies determined in each intervals related to fluvial and deep-water sinuous channel systems.

As the first advantage, flattening method gives the possibility to neglect the effect of structural elements and show the details of the features seen on a flat surface. Another privilege is that it requires only one horizon to be interpreted in order to perform the method. Generally, the procedure of the method is not time consuming, because it is not difficult to change time slices on 3D seismic data.

Coming to the disadvantages, method asks for the horizons which are relatively close to the target area, so it can give accurate results. The only time consuming aspect of this method is creating the volume attributes. However, creating surface attributes in the analysis helps in saving time.

Figure 6.1 shows the time slice and surface map of deep-water fan obtained from flattening method and regular horizon interpretation using the same attribute. The onset of main feeder channel and distal fan lobes are not well seen in Figure 6.1a. However, it can be concluded that some noises come from the seismic data as there exist some artifacts in Figure 6.1b. Consequently, detailed internal architecture and geomorphology of deep-water fan is more visible in 6.1a with less noise; however, the lobes of fan have a

shape that is not visible.

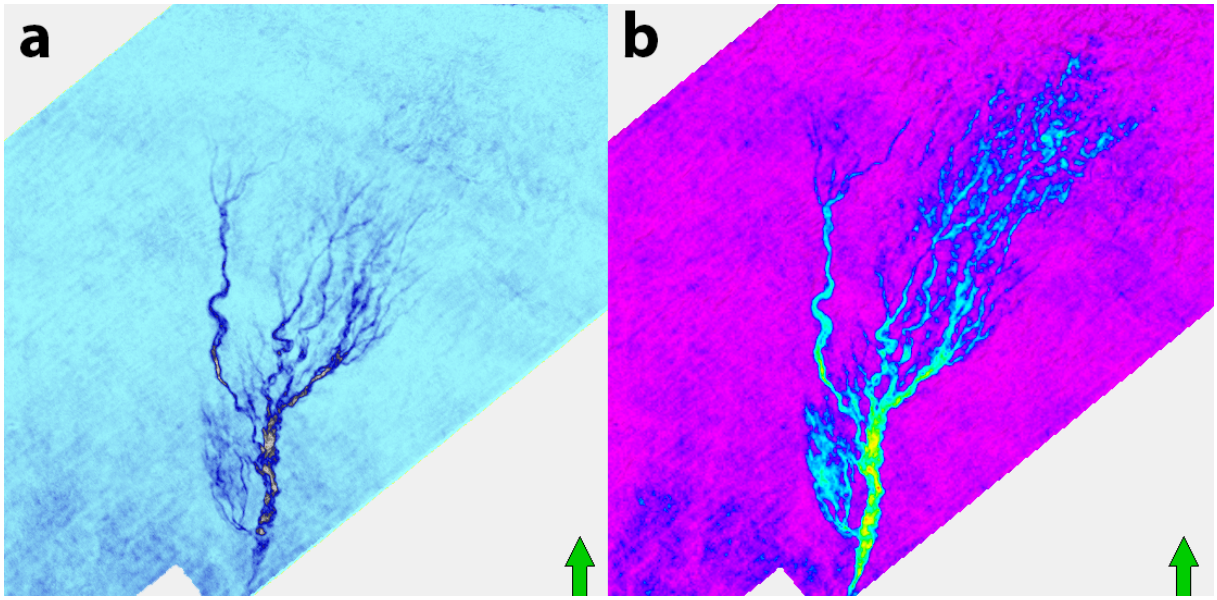

Figure 6.1: Comparison of time slice with surface map: a) Time slice from flettened volume integrating with RMS attribute, b) RMS surface attribute map is performed after interpreting single horizon.

6.2 Seismic Expression

Strong bright amplitude within the Triassic was recognized in 2D seismic line on the Finnmark platform shown in Figure 6.2 (Sollid et al., 2003; Hadler-Jacobsen et al., 2005). Based on the observation of the several clinoform geometries, the clinoform package included a constant thickness and was therefore interpreted as prograding slope cycles. The clinoform reflector continued from upper to lower segment position of the bright amplitude. Bright amplitude anomaly indicated the deposition of the sediments happened in the lower downlapping portion of a single clinoform (Hadler-Jacobsen et al., 2005).

A-A' dip-composite section shows the clinoform geometry of strong reflector which is seismic expression of channelized fan between two parallel Intra Lower and Base Triasssic horizons (Figure 6.3). The inclination of fan changed slightly in SW-NE direction. In the same direction, the strength of amplitude decreased from high to moderate-low which means that the channelized shape was transformed to distributary fan form.

Figure 6.4 shows three strike-composite sectional views of deep-water fan. According to Hadler-Jacobsen et al., 2005, the deep-water fan was deposited within a low shelf to basin setting. The thickness of deep-water fan reflector was not considerably varied in

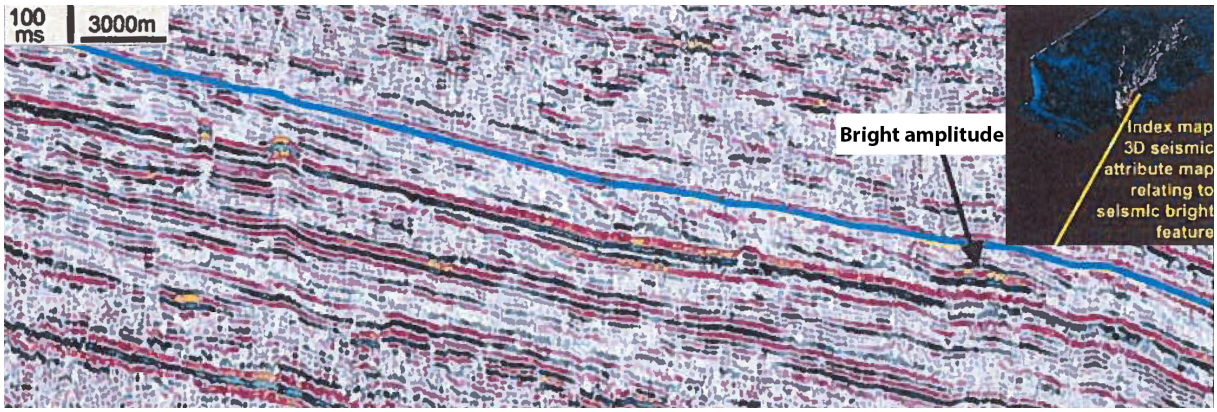

Figure 6.2: 2D seismic section on the Finnmark Platform, SW Barents Sea (modified from Hadler-Jacobsen et al., 2005).

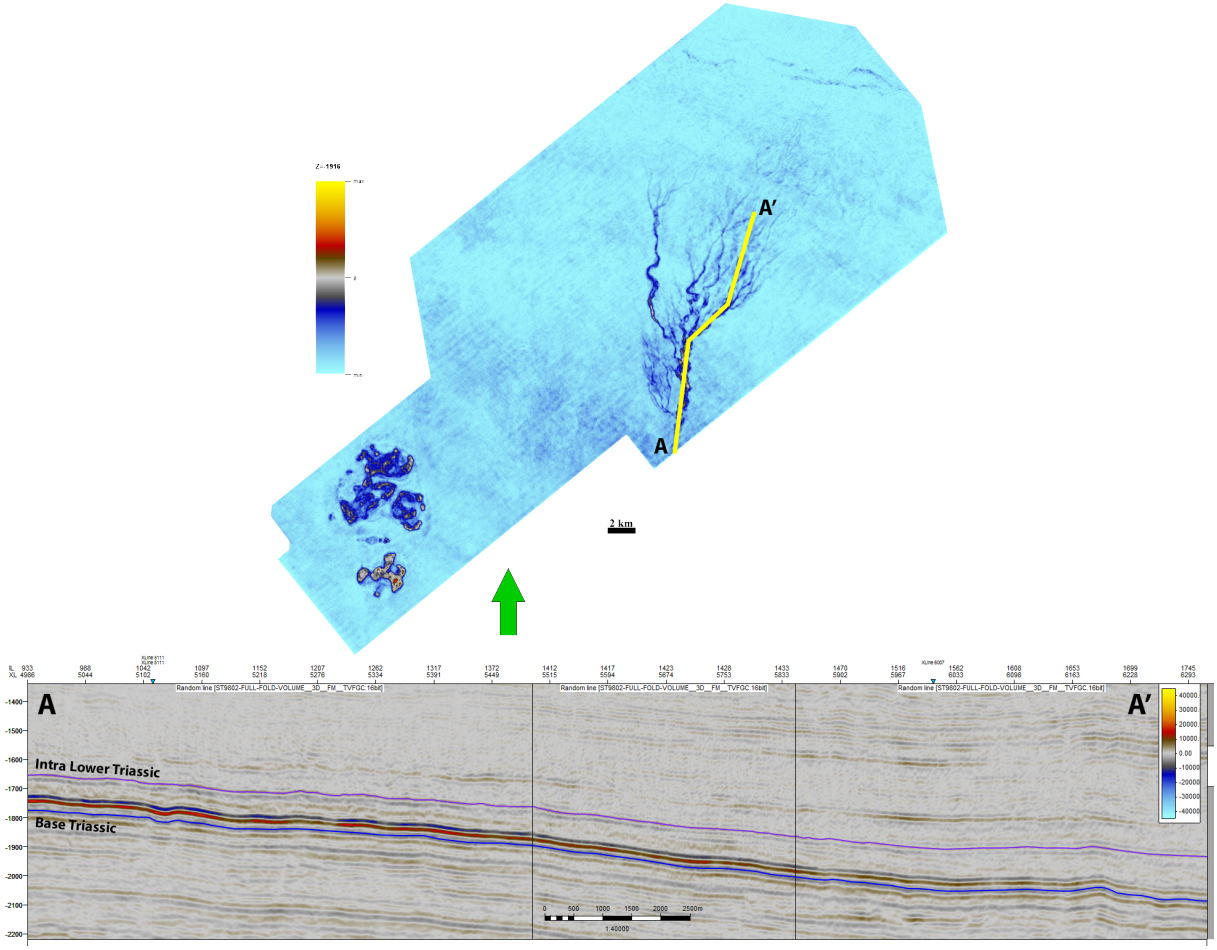

Figure 6.3: Dip-composite section through the deep-water fan.

all sections. However, the best thickness anomaly was recorded in C-C' section. The main feeder channel showed in A-A' section, expresses slightly higher amplitude than the distributary channels in B-B'. This indicates that the sediments were distributed by this main channel and created this finger shaped features. The main channel was deposited earlier than the splay-like feature, as higher amplitude was relatively recorded below

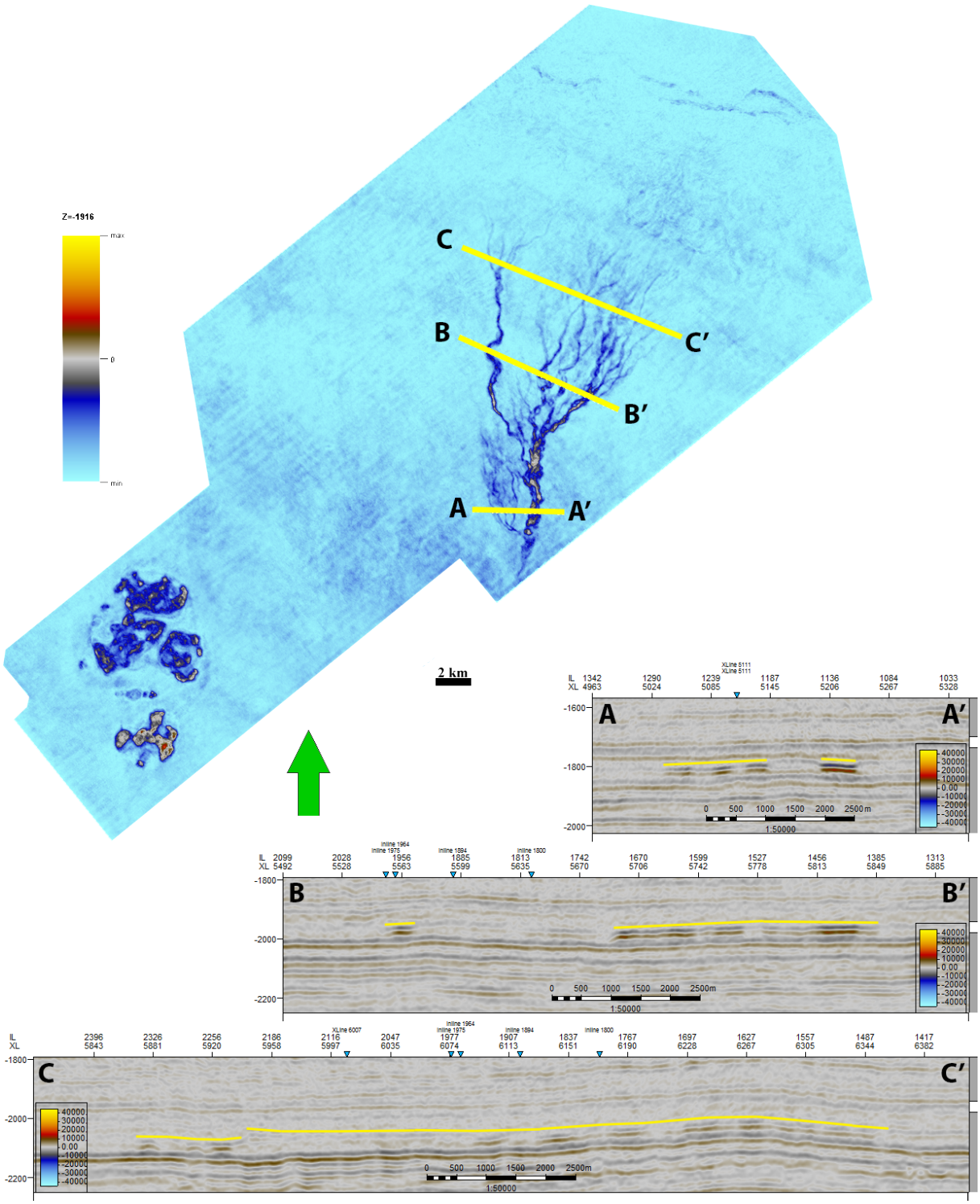

Figure 6.4: Strike-composite sections through the deep-water fan.

the lower amplitude in A-A'. Beyond this features, internal channelized lobe forms are displayed with low amplitude reflections shown in section C-C'.

The section C-C' also illustrates that there is a comparative age difference between these lobe forms. This analysis confirms that the channelized fan was developed in three

main stages (Figure 6.5). According to Hadler-Jacobsen et al., 2005 and Gardner et al., 2003, this development was started with a minor deep-water fan at the toe of slope, and feeder channel was the main conduit of the sediments (A). Afterwards, slope channel avulsion was initiated and followed the same feeder channel at the toe of slope to the basin floor (B). Finally, retreat of the main fan combined with feeder channel backfilling and significant slope overbank splay depositition as a function of reduced feeder channel margin relief occurred (C) (Hadler-Jacobsen et al., 2005).

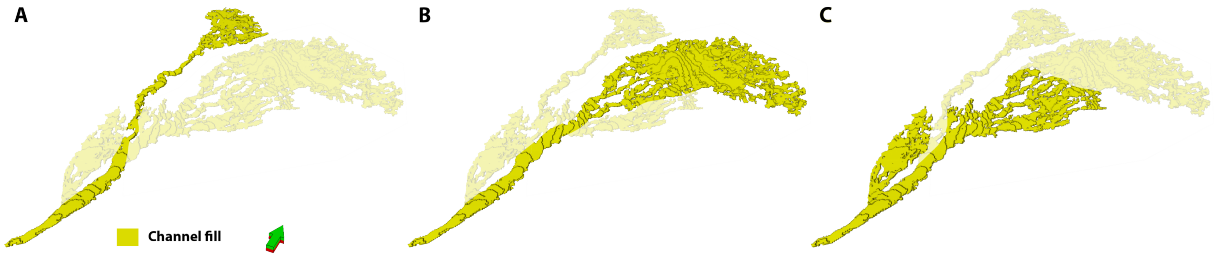

Figure 6.5: The development of deep-water fan is shown in three stages from A to C using geobody extraction.

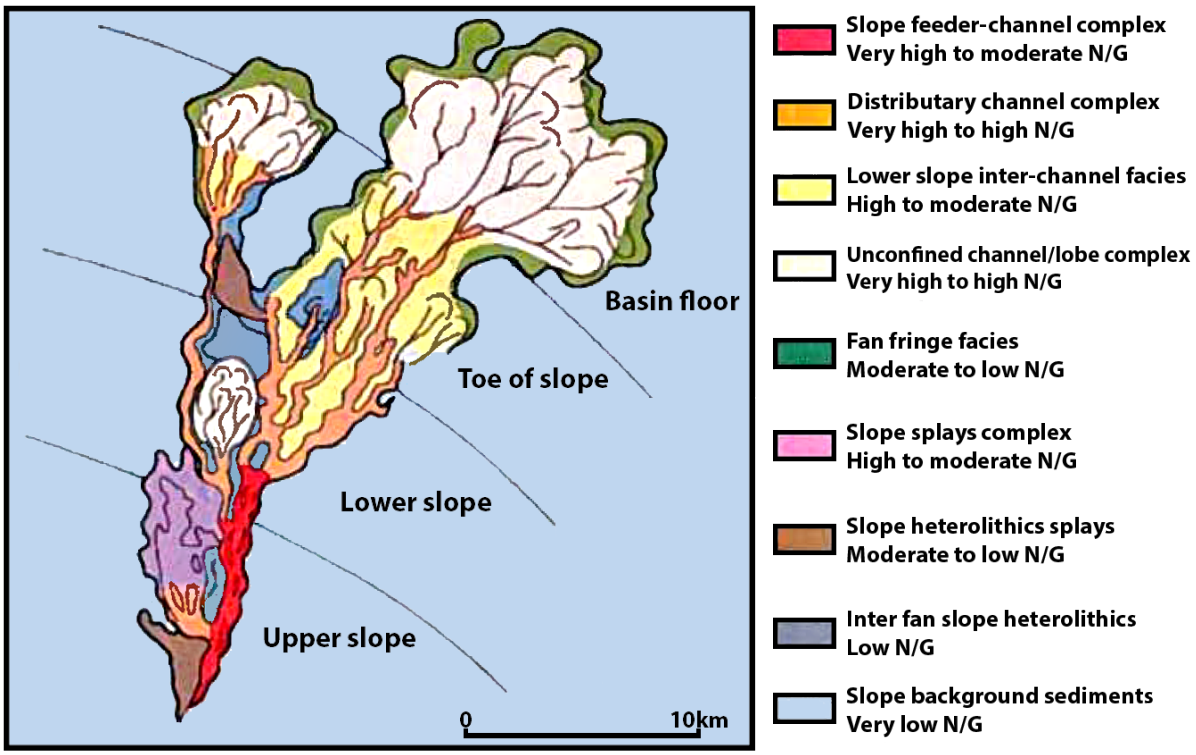

Figure 6.6: Lithology distribution of deep-water fan (modified from Hadler-Jacobsen et al., 2005).

Geobody extracted based on bright amplitude reflections is a good sign of sand-prone lithology (Figure 6.5). Lithology distribution is important for reservoir facies and

net to gross ratio identification. In 2005, the lithology distribution model of deep-water fan (Figure 6.6) was described in the work done by Hadler-Jacobsen et al. The model was created based on outcrop studies from the the Delaware and Tanqua Karoo basins (Johnson et al., 2001; Gardner and Borer, 2000). In the model, the feeder channel, distributary channels with inter-channel facies and channel/lobe complex demonstrated mostly high net to gross ratios.

6.3 Seismic Geomorphology

"Seismic geomorphology, the extraction of geomorphic insights using predominantly three-dimensional seismic data, is a rapidly evolving discipline that facilitates the steady of the subsurface using plan view images" (Posamentier et al., 2007). In this thesis, geomorphic features were extracted using mostly flattening method. The several channel systems were interpreted in the upper and lower part of the Triassic age. The fluvial channels were identified in the Upper Triassic (Snadd formation) confirmed by core analysis studies in the depositional environment section. The deep-water channels were recognized in the lower part (probably Havert formation) of Triassic. The flow of fluvial channel systems (Figure 6.8) was in the north and northwest direction referred by regional geological studies, while deep-water system had the north and northeast trend (Figure 6.9).

A part of the seismic geomorphology was allocated to morphometric calculations estimated based on the channels interpreted from time slices of the upper and lower Triassic part of the seismic volume. Stream and valley lengths (for each value of stream, valley length and stream width, see Figures 6.8, 6.9 and Table 6.1) were measured from the time slices which were the inputs for calculation of the sinuosity ratio. This ratio which is equal to the measure of distance between A and B points along the stream was divided by the straight line (valley length) distance be-

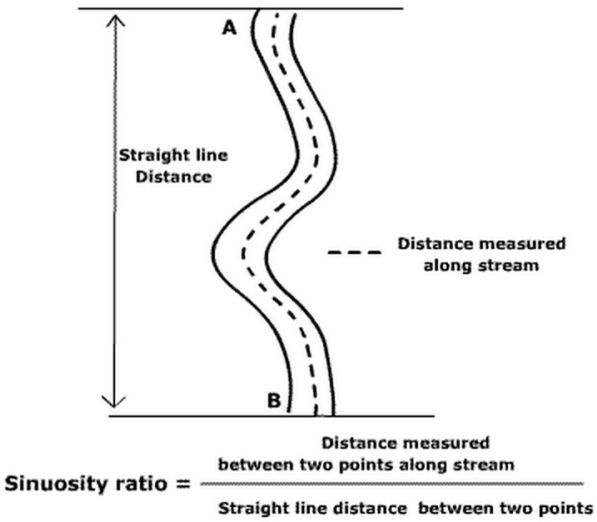

Figure 6.7: Sinuosity ratio (modified from Ritter, 2006).

tween the same points (Figure 6.7). This equation was used to calculate the sinuosity for different length of fluvial and deep-water channels. All the morphometric calculations are summarized in Table 6.1. Based on the information provided by this table, high sinuous channel was identified with a sinuosity ratio of 1.53, measured in time slice at -968 ms which was meandering channel number 2 depicted in Figure 6.8d, while low sinuous channel comprised a ratio of 1.06, shown in Figure 6.8a.

Table 6.1: Morphometric calculations of channels in fluvial and deep-water systems.

Time slices	-816	-864	-864	-928	-968	-968	-968	-1916
Channel numbers	-	1	2	-	1	2	3	-
Stream length (km)	24.5	35.4	35.8	20.3	23.2	33.1	26.5	14.3
Valley length (km)	23.1	30.1	31.1	15.7	18.5	21.6	24.1	12.6
Stream width (km)	0.30	0.75	0.86	0.70	0.30	0.44	0.80	0.50
Sinuosity ratio	1.06	1.18	1.15	1.29	1.25	1.53	1.10	1.14

Geometry, internal architecture and distribution of seismic anomalies in Figure 6.9 help to reveal the geomorphic elements of deep-water system. The main seismic geomorphic elements were the crevasse channels and splay, main feeder channel, distributary channels and channelized lobe complex. These elements were deposited within a low shelf to basin setting.

3D seismic data of several examples showed similarities in external architectures of fluvial and deep-water channel systems, however there were important differences in internal morphology of both channel systems. Similarities and differences of fluvial and deep-water channel systems were recognized by comparing them in the cross- and plan-sectional views (Figure 6.8 and 6.9). The shape of both channel systems was of a meandering type. From the table, it can be seen that sinuosity ratio was similar between meandering channel in Figure 6.9 (1.14) and channel 2 in Figure 6.8b (1.15). Another similarity was identified in the stream width in which deep-water channel had a width of 0.50km, while meandering channel 2 in Figure 6.8d had 0.44km width. However, there was a significant difference in stream lengths of both sinuous channel systems; the length of fluvial channels was longer than deep-water. Although the sinuous channel geometry was developed in the fluvial systems on regional scale, deep-water systems were more episodic. This can be the reason that the seismic expression of deep-water system was

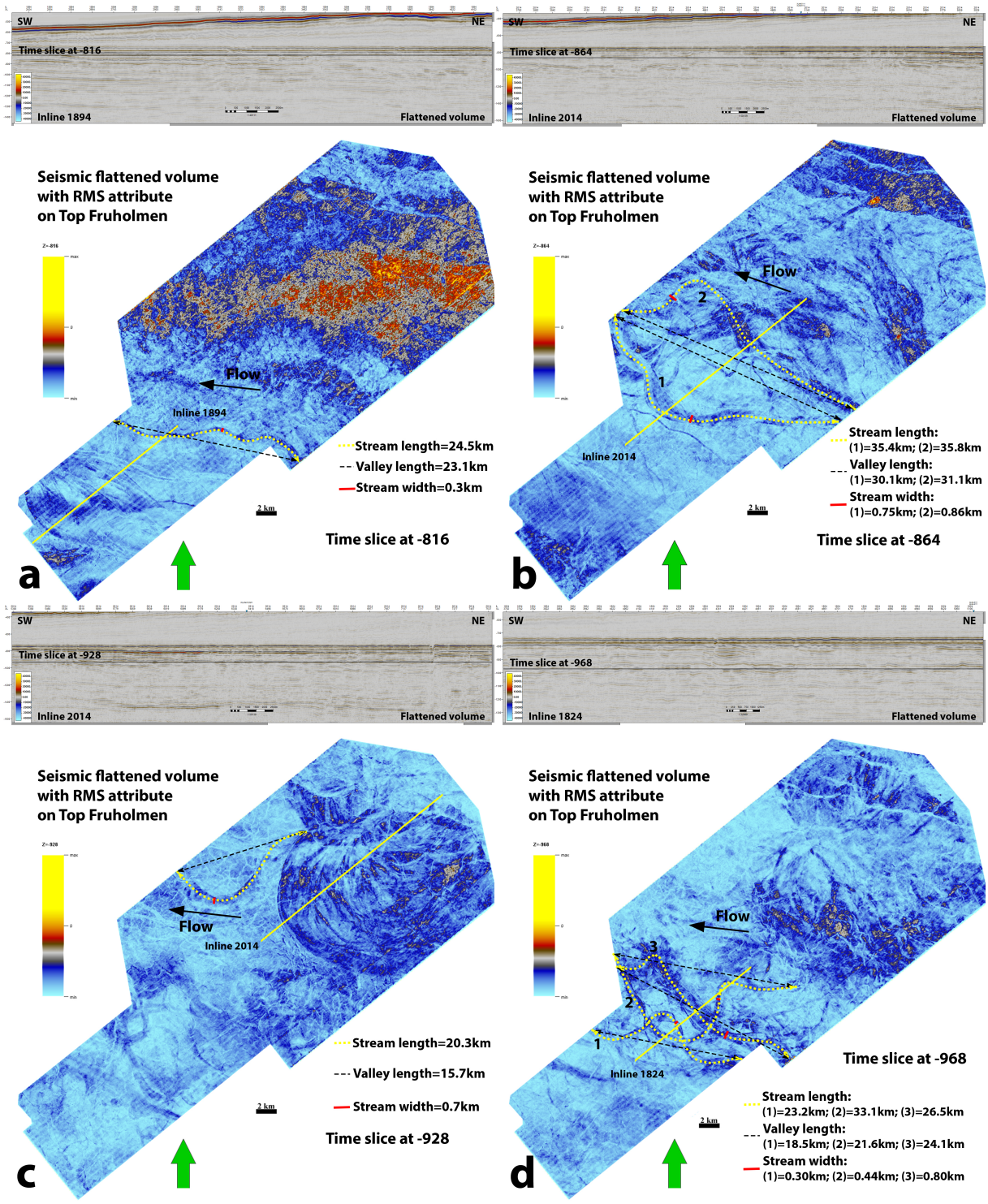

Figure 6.8: Morphometric values such as stream, valley lengths and stream width were calculated based on time slices at -816 (a), -864 (b), -928 (c) and -968 (d) *ms*.

clearly visible in the data than fluvial counterparts.

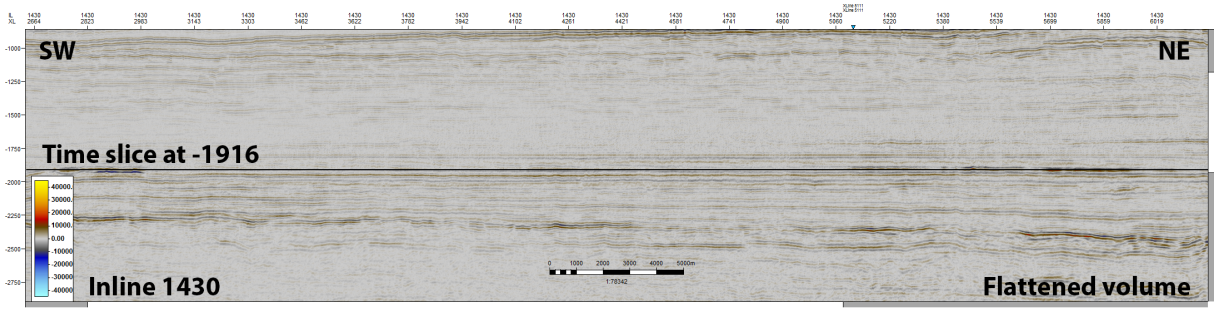

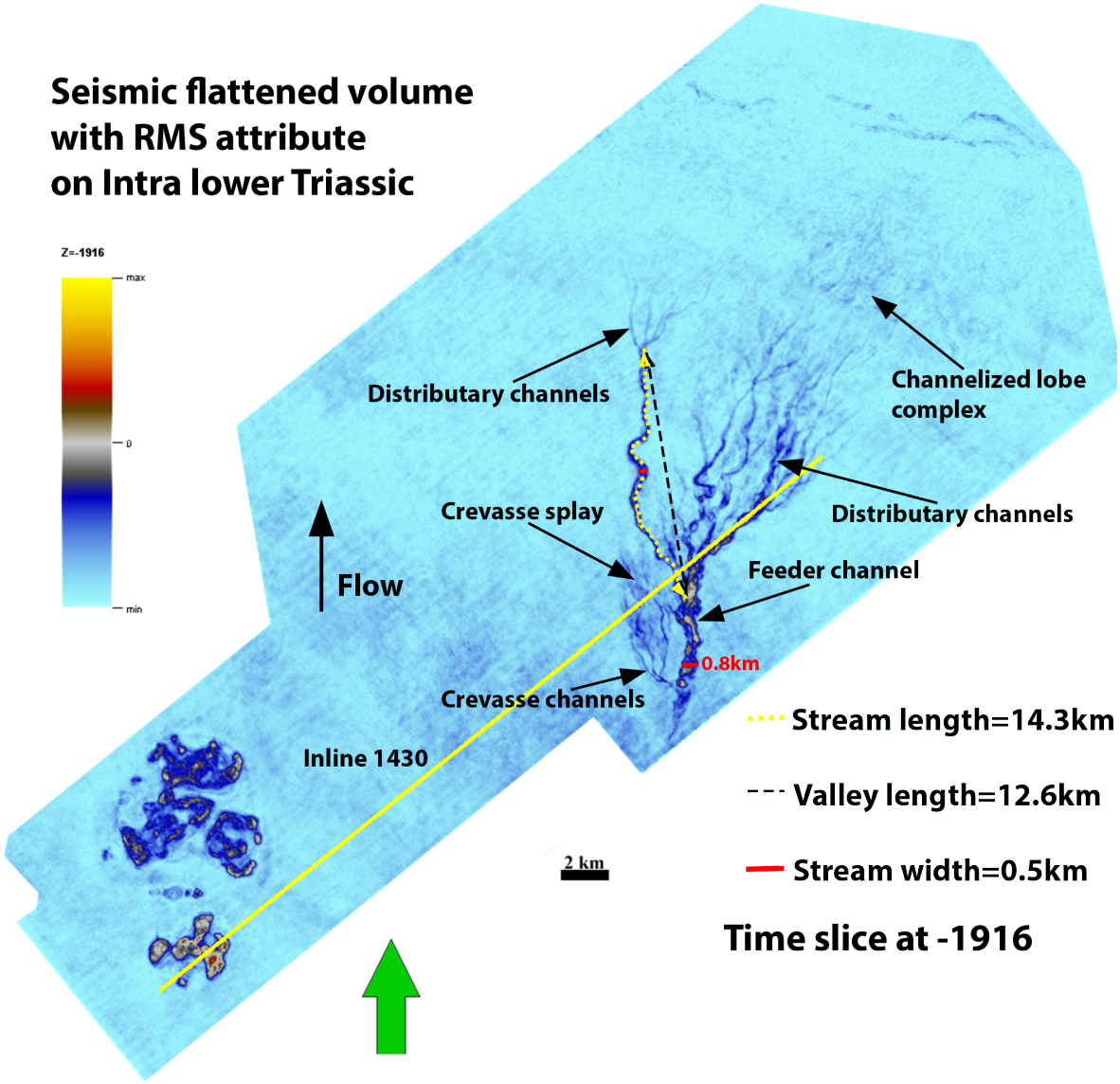

Figure 6.9: Morphometric values such as stream, valley lengths and stream width are calculated based on time slice at -1916 *ms*. Depositional elements of the fan system are also described.

Chapter 7

Conclusions

Mapping and identifying the internal architectures of channel systems was made possible through the advent of 3D seismic data, which eventually allowed the interpretation of stratigraphic features and thorough understanding of different depositional systems in the subsurface. Application of various techniques and methods of interpretation using 3D seismic data helped in determining the seismic expression of deep-water fan system. The observations acquired from the analyses done in this work can be summed up as:

- Based on the observation from seismic time slices and cross sections, the existence of fluvial channel systems has been confirmed in the Snadd formation, while the deep-water channels were identified in the Havert formation.
- The detailed internal architecture of deep-water fan can be seen more clearly in the image obtained from flattening rather than conventional methods. Flattening method enables us to express the actual depositional elements with less artifacts in the seismic data.
- The deep-water fan system was developed in three main phases. These phases can be summarized as the development of deep-water fan from initiation and growth to retreat phases.
- The main depositional elements were the crevasse channels and splay, main feeder channel, distributary channels and channelized lobe complex within a low shelf to basin setting.
- The shape, stream width and sinuosity ratio of deep-water channel are similar to

those of fluvial. However, the significant difference of both sinuous channel systems is in stream lengths. The deep-water system is seismically well expressed in the data compared to the fluvial systems.

References

Brown, A. (2004). *Interpretation of Three-dimensional Seismic Data*. Number no. 42 in AAPG memoir. American Association of Petroleum Geologists and the Society of Exploration Geophysicists.

Bugge, T., Mangerud, G., Elvebakk, G., Mørk, A., Nilsson, I., Fanavoll, S., and Jorunn, V. O. (1995). The upper palaeozoic succession on the finnmark platform, barents sea. *Norsk Geologisk Tidsskrift*, 75(1):3–30. cited By (since 1996)51.

Bulat, J. (2005). Some considerations on the interpretation of seabed images based on commercial 3d seismic in the faroe-shetland channel. *Basin Research*, 17(1):21–42.

Colpaert, A., Pickard, N., Mienert, J., Henriksen, L. B., Rafaelsen, B., and Andreassen, K. (2007). 3d seismic analysis of an upper palaeozoic carbonate succession of the eastern finnmark platform area, norwegian barents sea. *Sedimentary Geology*, 197(1–2):79 – 98.

Faleide, J. I., Gudlaugsson, S. T., and Jacquart, G. (1984). Evolution of the western barents sea. *Marine and Petroleum Geology*, 1(2):123 – 150.

Faleide, J. I., Vågnes, E., and Gudlaugsson, S. T. (1993). Late mesozoic-cenozoic evolution of the south-western barents sea in a regional rift-shear tectonic setting. *Marine and Petroleum Geology*, 10(3):186 – 214.

Gardner, M. H. and Borer, J. M. (2000). Submarine channel architecture along a slope to basin profile, brushy canyon formation, west texas. *AAPG Memoir*, 72:195 – 213. Brushy Mesa;Codorniz Canyon;Colleen Canyon;Guadalupe Canyon;Popo Fault;Salt Flat Bench;.

Gardner, M. H., Borer, J. M., Melick, J. J., Mavilla, N., Dechesne, M., and Wagerle, R. N. (2003). Stratigraphic process-response model for submarine channels and related

features from studies of permian brushy canyon outcrops, west texas. *Marine and Petroleum Geology*, 20(6–8):757 – 787. Turbidites: Models and Problems.

Gernigon, L. and Brönner, M. (2012). Late palaeozoic architecture and evolution of the southwestern barents sea: insights from a new generation of aeromagnetic data. *Journal of the Geological Society*, 169(4):449–459.

Glørstad-Clark, E., Birkeland, E., Nystuen, J., Faleide, J., and Midtkandal, I. (2011). Triassic platform-margin deltas in the western barents sea. *Marine and Petroleum Geology*, 28(7):1294 – 1314.

Glørstad-Clark, E., Faleide, J. I., Lundschien, B. A., and Nystuen, J. P. (2010). Triassic seismic sequence stratigraphy and paleogeography of the western barents sea area. *Marine and Petroleum Geology*, 27(7):1448 – 1475.

Gudlaugsson, S., Faleide, J., Johansen, S., and Breivik, A. (1998). Late palaeozoic structural development of the south-western barents sea. *Marine and Petroleum Geology*, 15(1):73 – 102.

Hadler-Jacobsen, F., Johannessen, E. P., Ashton, N., Henriksen, S., Johnson, S. D., and Kristensen, J. B. (2005). Submarine fan morphology and lithology distribution; a predictable function of sediment delivery, gross shelf-to-basin relief, slope gradient and basin topography. *Petroleum Geology of Northwest Europe: Proceedings of the ... Conference*, 6:1121 – 1145.

Johnson, S. D., Flint, S., Hinds, D., and de Ville Wickens, H. (2001). Anatomy, geometry and sequence stratigraphy of basin floor to slope turbidite systems, tanqua karoo, south africa. *Sedimentology*, 48(5):987 – 1023. Tanqua Karoo;.

Klausen, T. G., Ryseth, A. E., Hellend-Hansen, W., Gawthorpe, R., and Laursen, I. (2014). Spatial and temporal changes in geometries of fluvial channel bodies from the triassic snadd formation of offshore norway. *Journal of Sedimentary Research*, 84(7):567–585.

NPD-Factpages (2014). Well 7131/4-1, Norwegian Petroleum Directorate. http://factpages.npd.no/FactPages/Default.aspx?nav1=wellbore&nav2=PageView|Exploration|All&nav3=5093&culture=en. Accessed: 07-09-2014.

Ogg, G. (2013). Barents Sea Chart, Natural History Museum, the chart was produced with the assistance of lundin norway. http://nhm2.uio.no/norges/litho/Barents_Chart.html. Accessed: 07-09-2014.

Posamentier, H. W., Davies, R. J., Cartwright, J. A., and Wood, L. (2007). Seismic geomorphology - an overview. *Geological Society, London, Special Publications*, 277(1):1–14.

Riis, F., Lundschien, B. A., Hoy, T., Mork, A., and Mork, M. B. E. (2008). Evolution of the Triassic shelf in the northern Barents Sea region. *POLAR RESEARCH*, 27(3):318–338.

Ritter, M. (2006). *The Physical Environment: An Introduction to Physical Geography*. National Council for Geographic Education.

Sheriff, R. and Geldart, L. (1995). *Exploration Seismology*. Cambridge University Press.

Skjold, L. J., van Veen, P. M., Kristensen, S. E., and Rasmussen, A. R. (1998). Triassic sequence stratigraphy of the southwestern barents sea. *Special Publication - Society for Sedimentary Geology*, 60:651 – 666.

Sollid, K., Ashton, N., Gytri, S. R., Henriksen, L. B., Larssen, G. B., Laursen, I., and Ronning, K. (2003). Seismic imaging and characterisation of triassic deep marine, coastal and fluvio-deltaic plays, southwestern barents sea. *Conference and Technical Exhibition - European Association of Geoscientists and Engineers*, 64.

Walderhaug, P. H. (2012). Petrography, diagenesis and reservoir quality of the Triassic Fruholmen, Snadd and Kobbe formations, southern Barents Sea. Master's thesis, Norwegian University of Science and Technology.

Worsley, D. (2008). The post-Caledonian development of Svalbard and the western Barents Sea. *POLAR RESEARCH*, 27(3):298–317.

Yilmaz, Ö. and Doherty, S. (2001). *Seismic data analysis: processing, inversion, and interpretation of seismic data*. Number no. 10, v. 2 in Investigations in geophysics. Society of Exploration Geophysicists.

Abbreviation

3D	**Three-D**imensional
2D	**Two-D**imensional
RMS	**R**oot **M**ean **S**quare
RAI	**R**elative **A**coustic **I**mpedance
GR	**G**amma **R**ay
PEF	**P**hotoelectric **Ef**fect
RC	**R**eflection **C**oefficient
AI	**A**coustic **I**mpedance
SW	**S**outh **W**estern
UTM	**U**niversal **T**ransverse **M**ercator
RKB	**R**otary **K**elly **B**ushing
IP	**I**nteractive **P**etrophysics
SEG	**S**ociety of **E**xploration **G**eophysicists
NPD	**N**orwegian **P**etroleum **D**irectorate

Nomenclature

λ	Wavelength
v	Velocity
f	Frequency
h_0	Depth
t	Two-way travel time
V_{clay}	Clay volume
$y(t)$	Seismic signal
$w(t)$	Input signal
$f(t)$	Impulse response

Appendix A

Petrophysical analysis

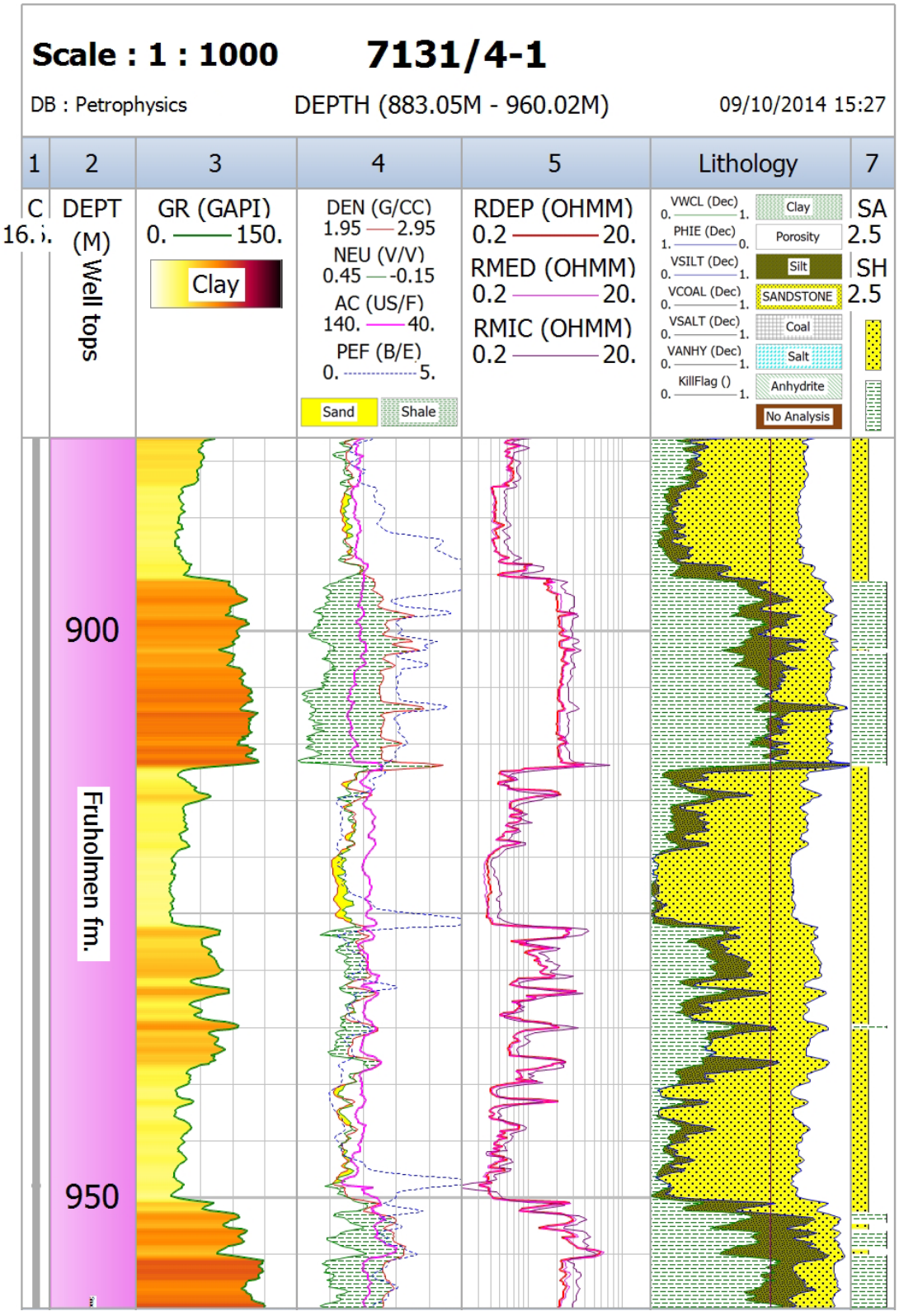

Figure A.1: Log plot of Fruholmen formation.

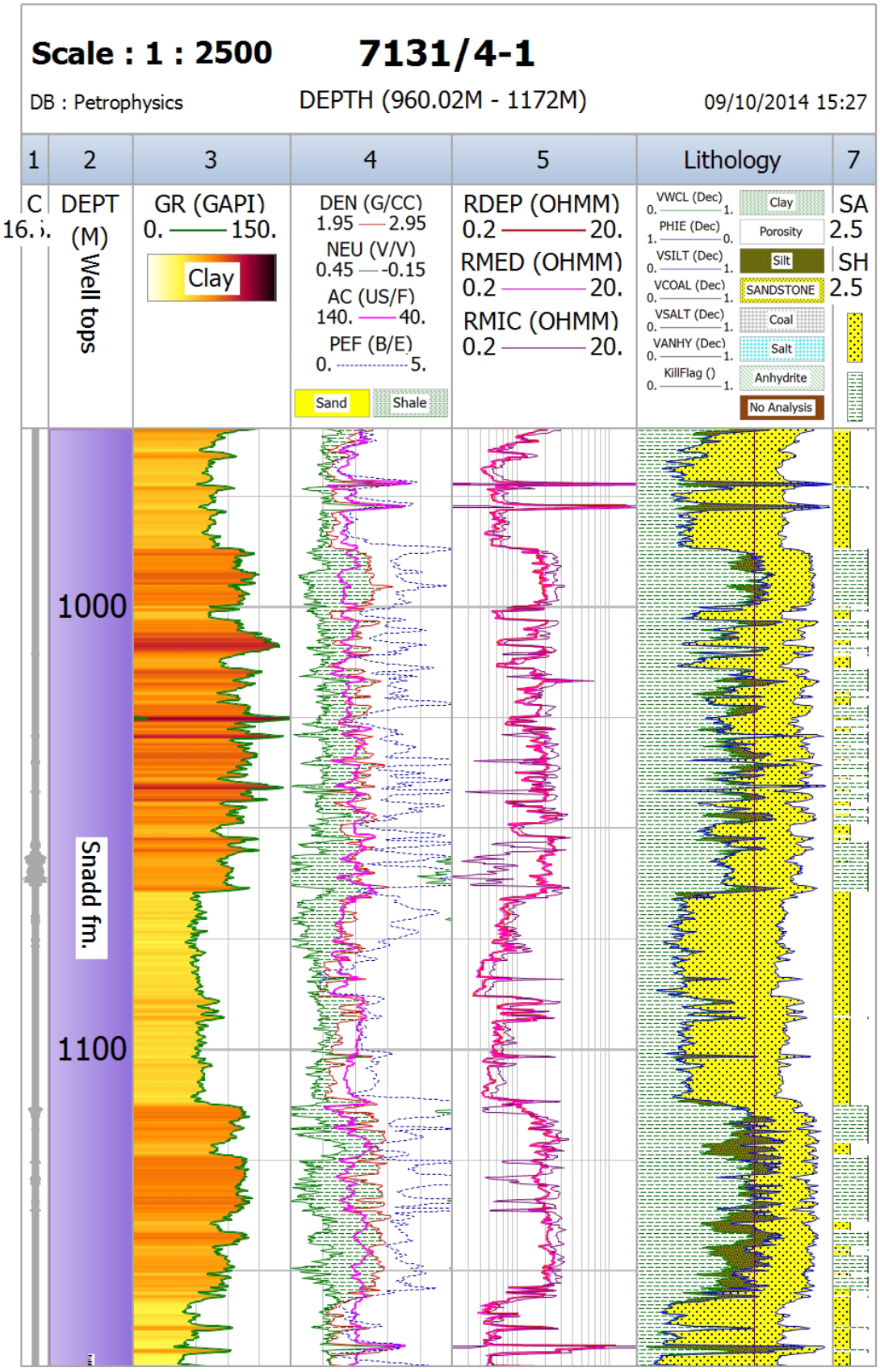

Figure A.2: Log plot of Snadd formation.

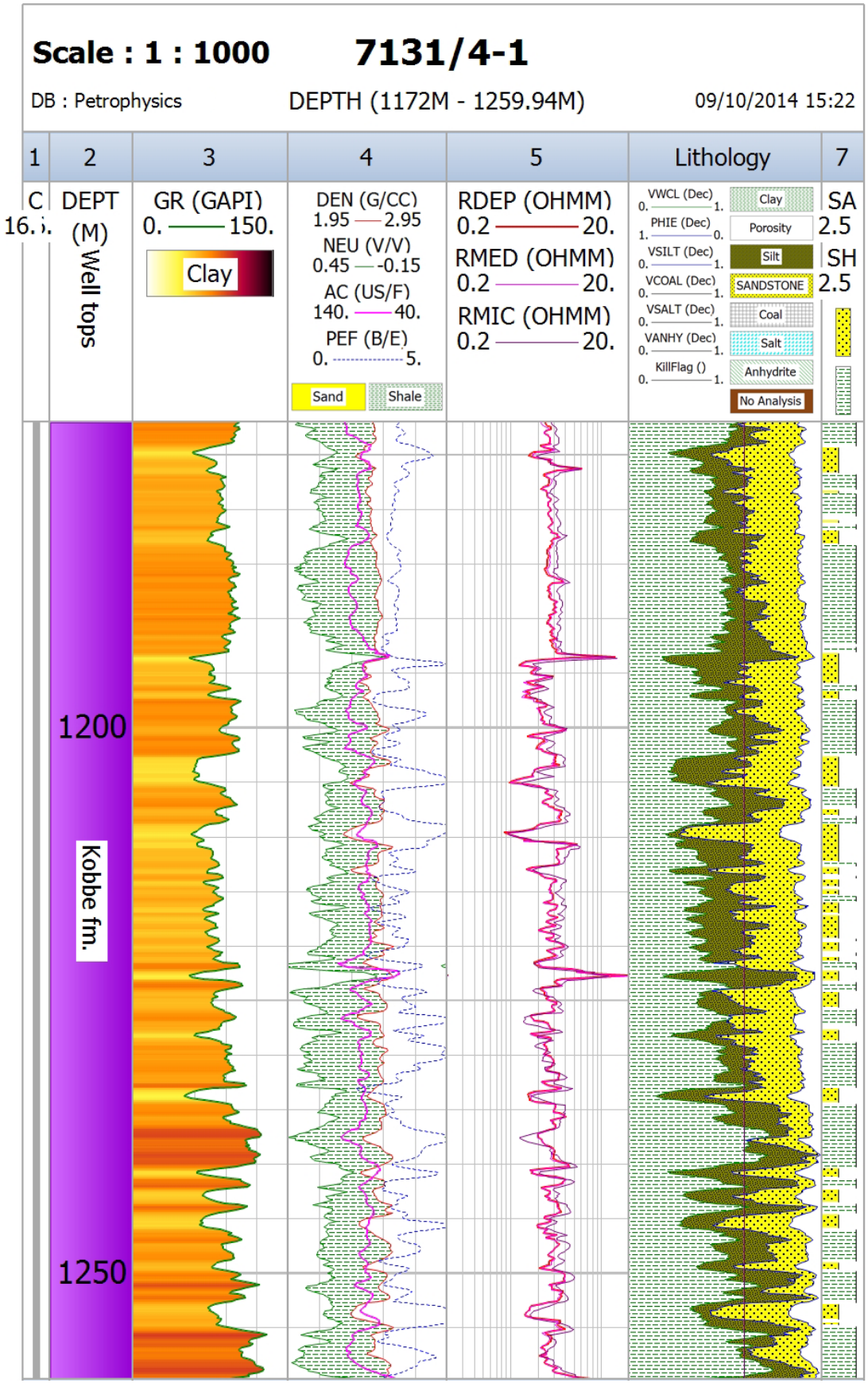

Figure A.3: Log plot of Kobbe formation.

Appendix B

Time slices

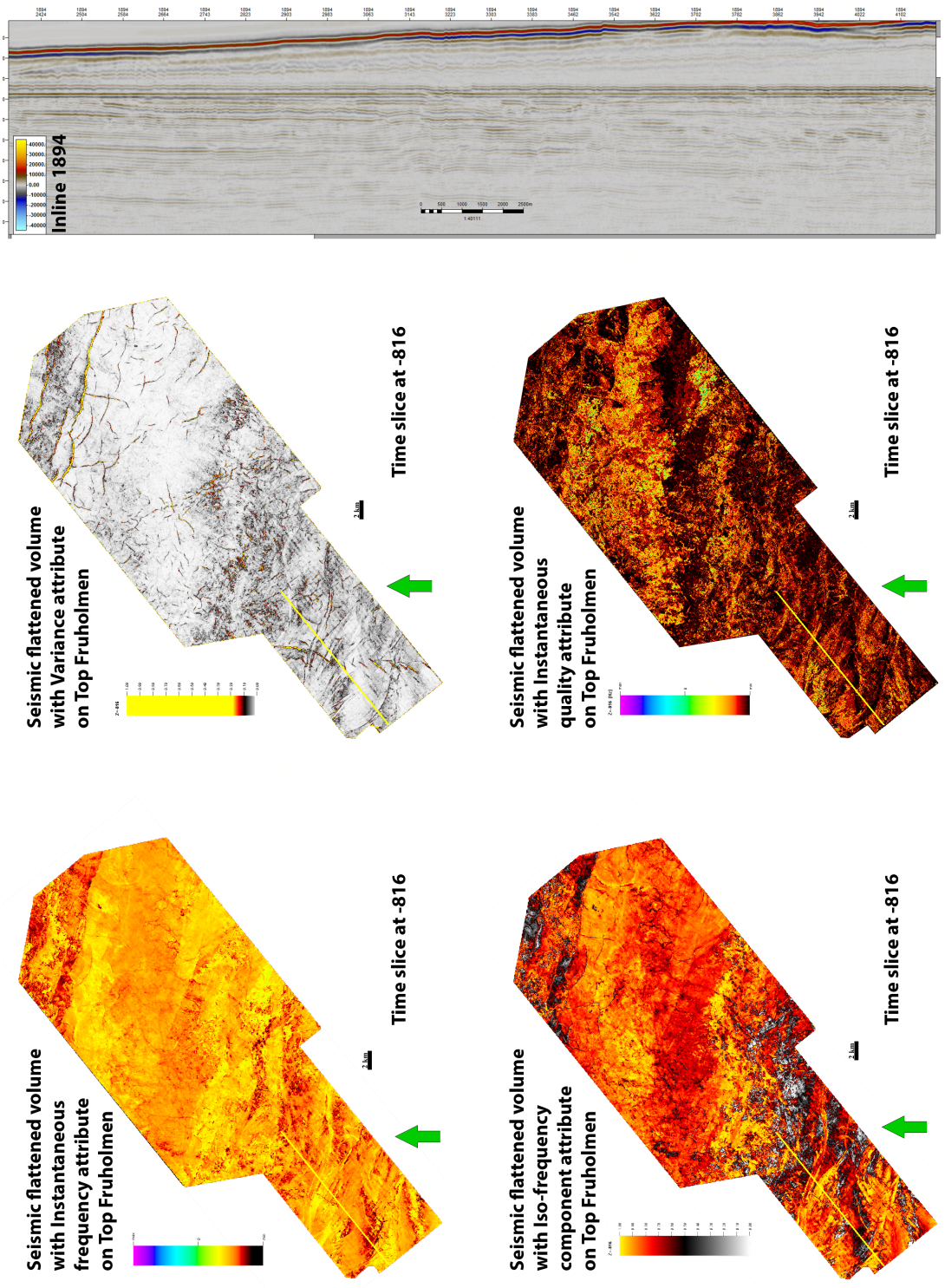

Figure B.1: Time slice at -816 performed by seismic flattened volume on Top Fruholmen.

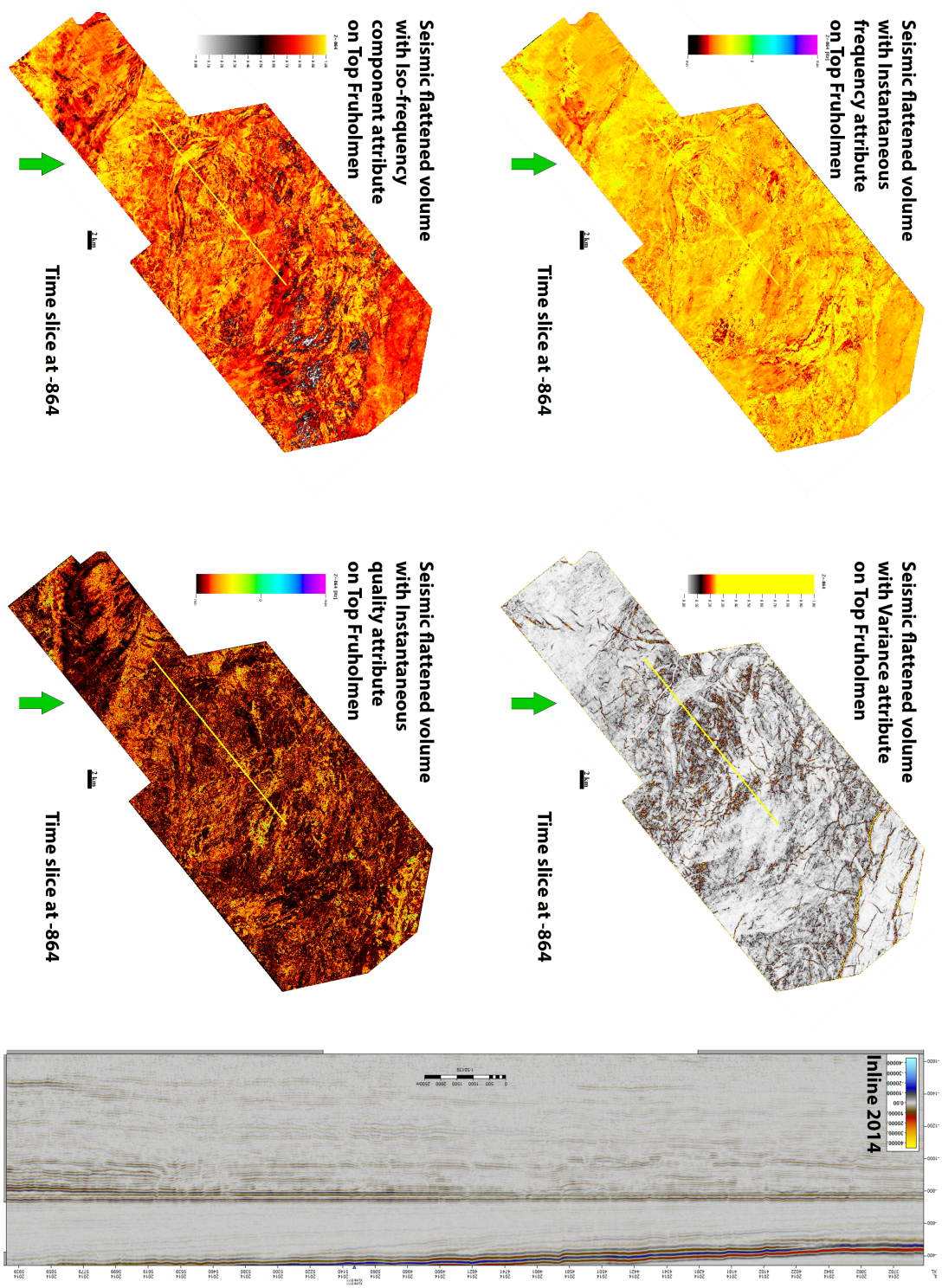

Figure B.2: Time slice at -864 performed by seismic flattened volume on Top Fruholmen.

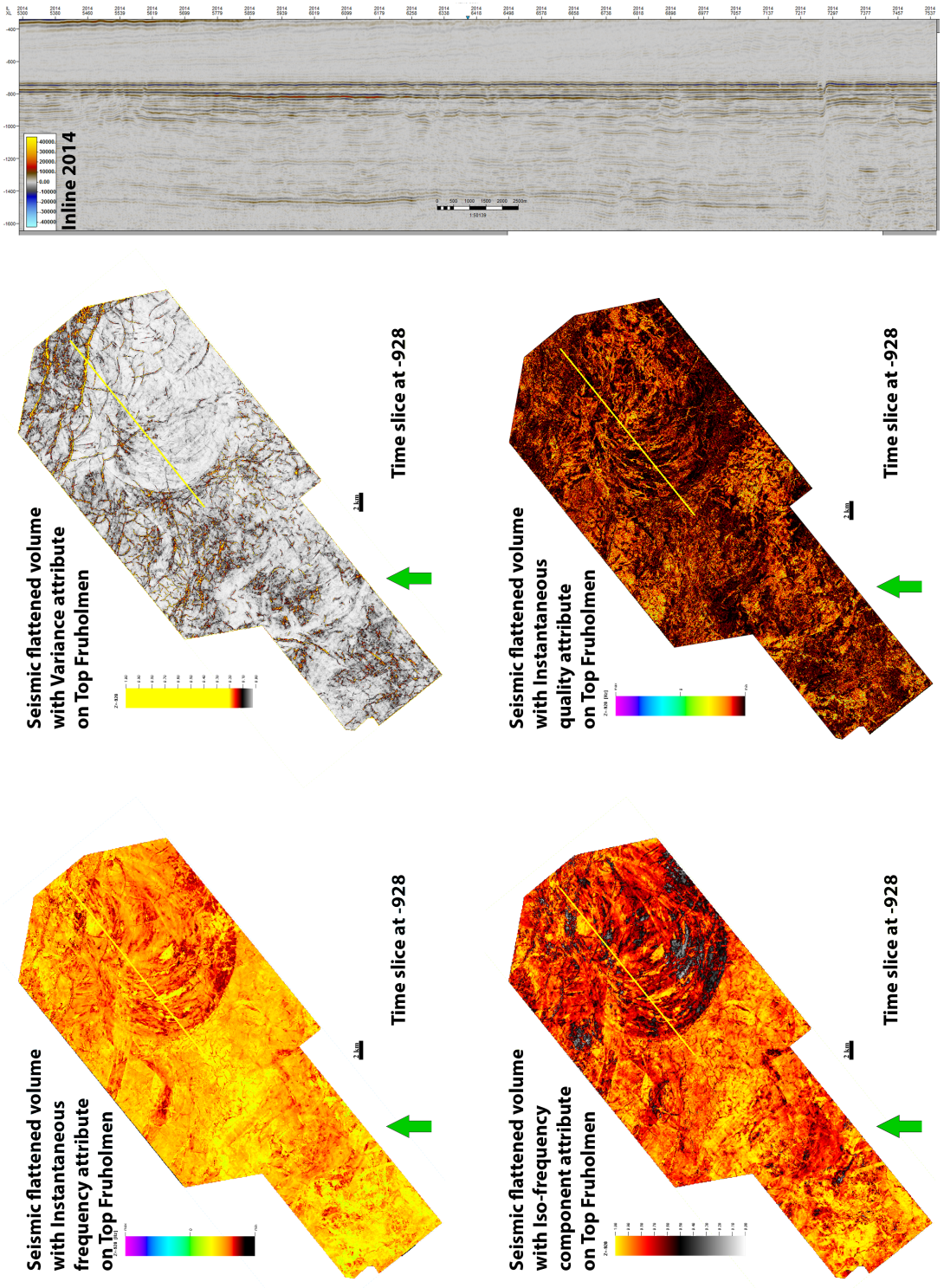

Figure B.3: Time slice at -928 performed by seismic flattened volume on Top Fruholmen.

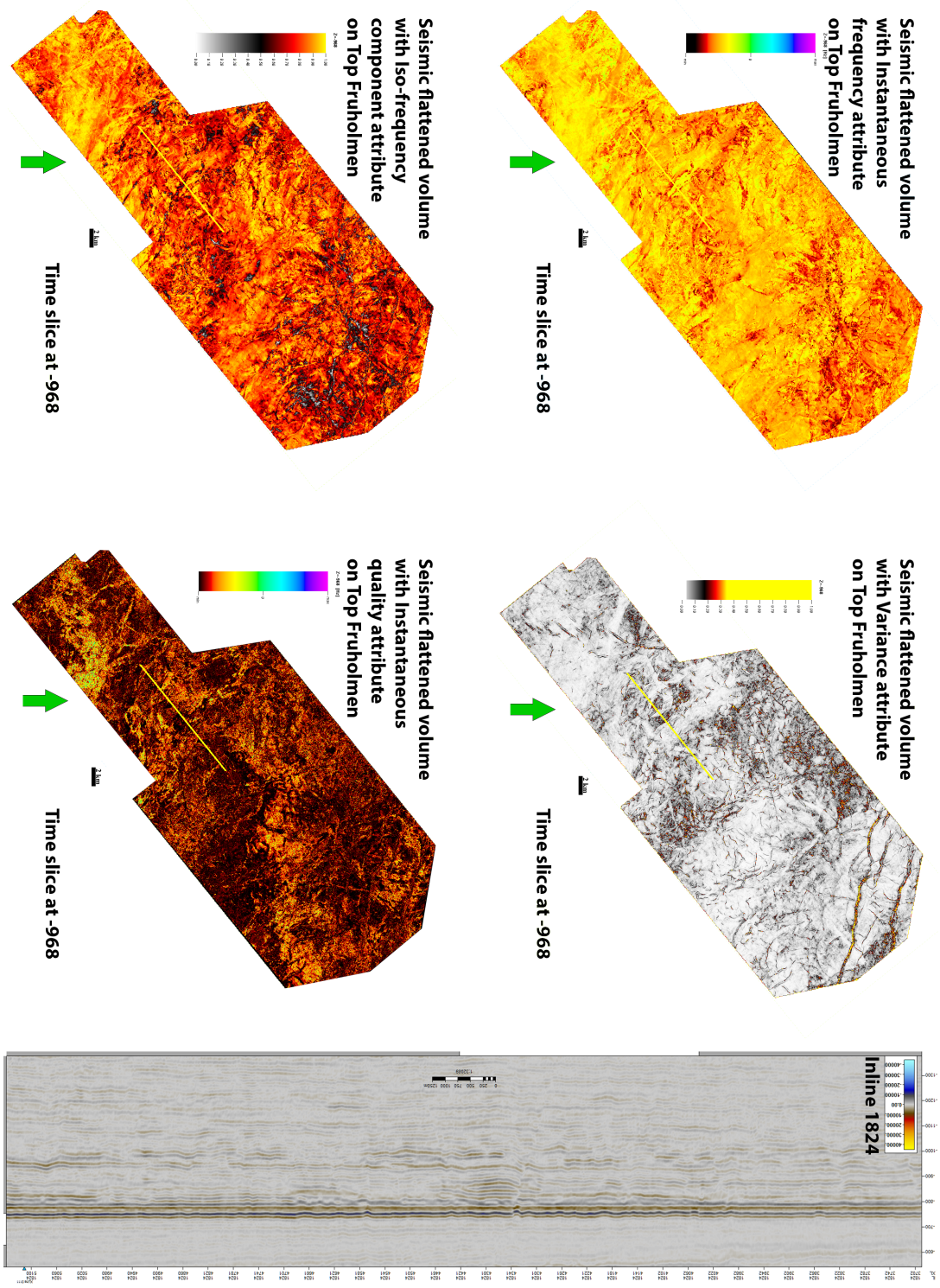

Figure B.4: Time slice at -968 performed by seismic flattened volume on Top Fruholmen.

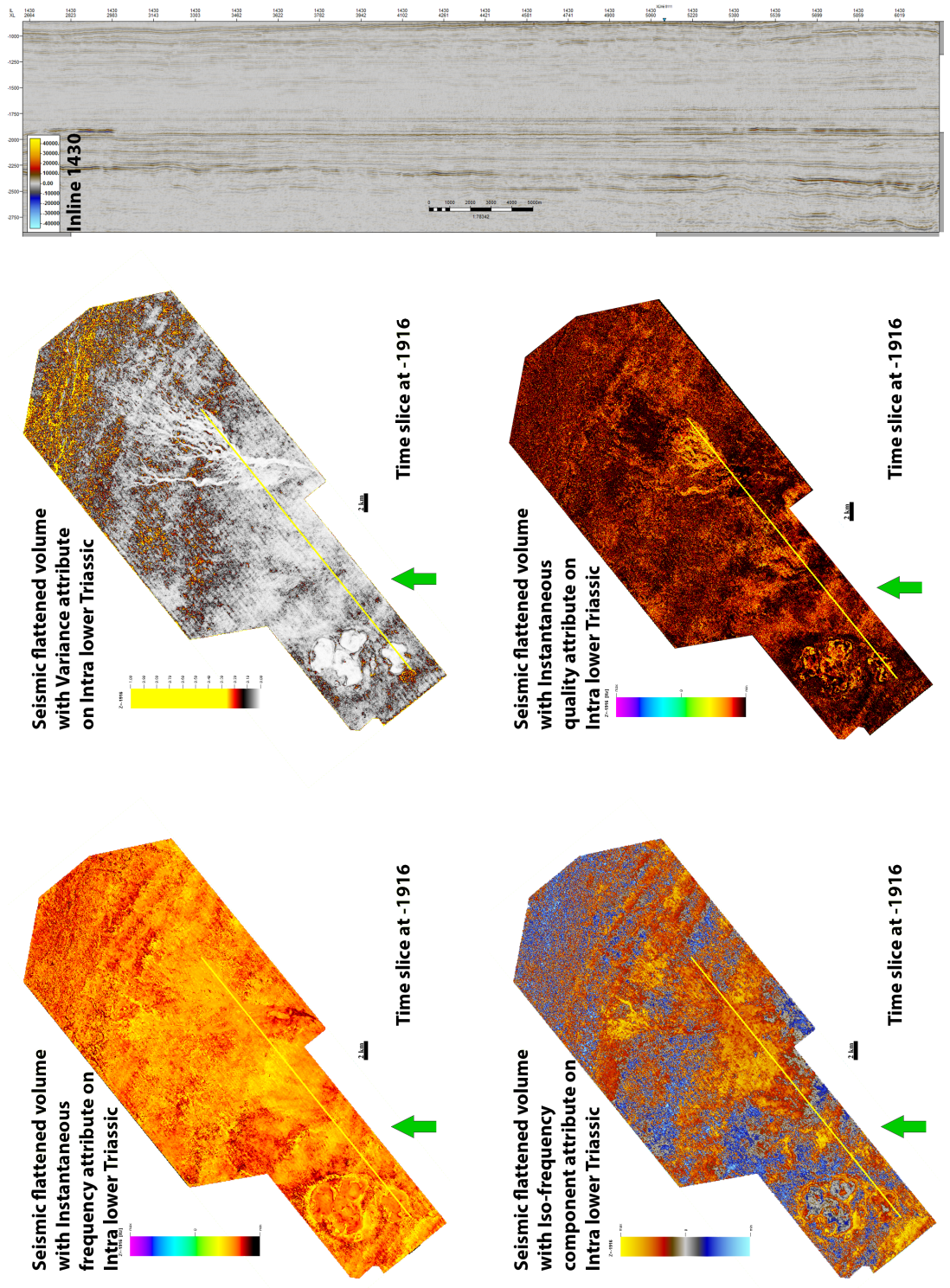

Figure B.5: Time slice at -1916 performed by seismic flattened volume on Intra Lower Triassic.

Appendix C

Surface attributes

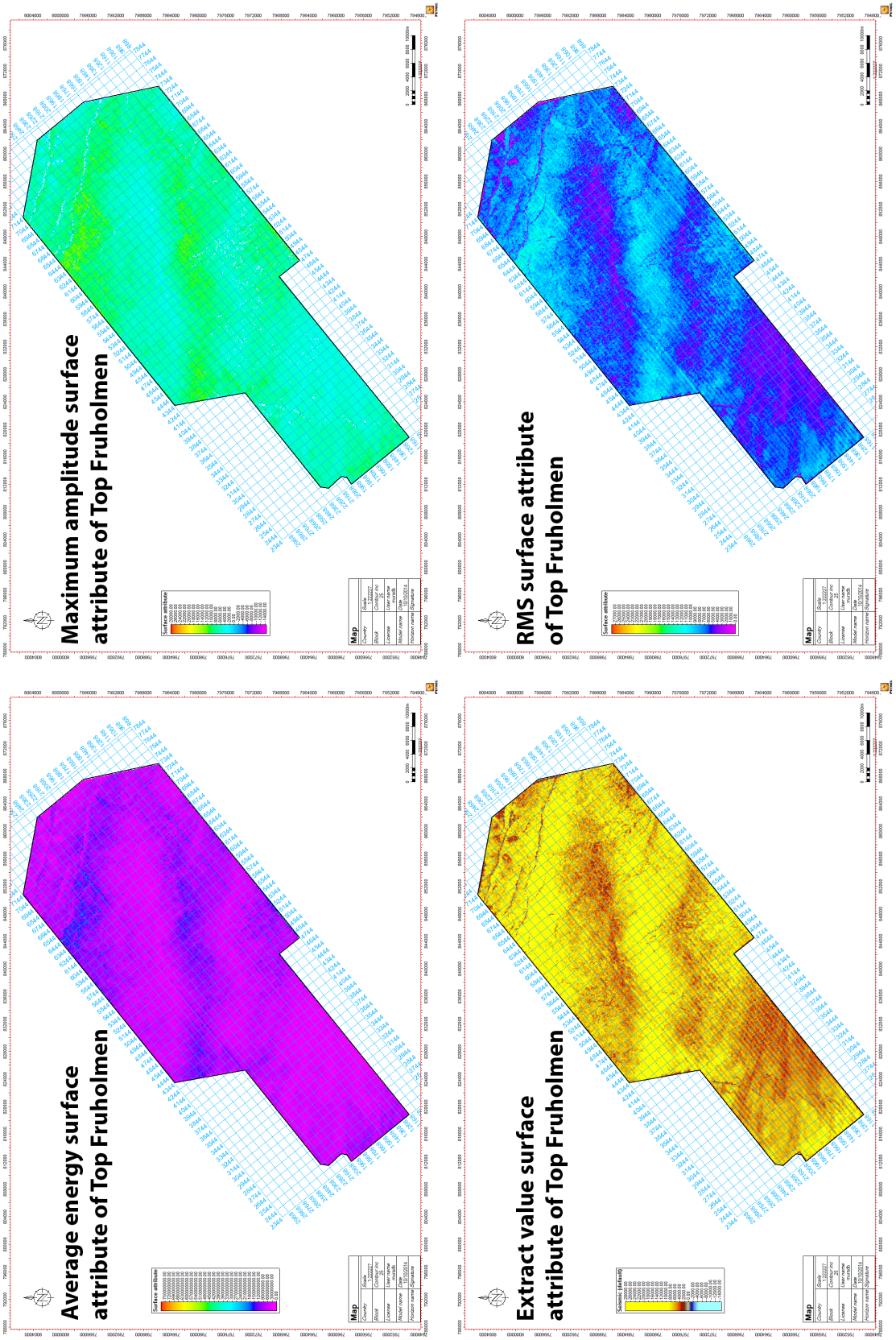

Figure C.1: Surface attributes of Top Fruholmen.

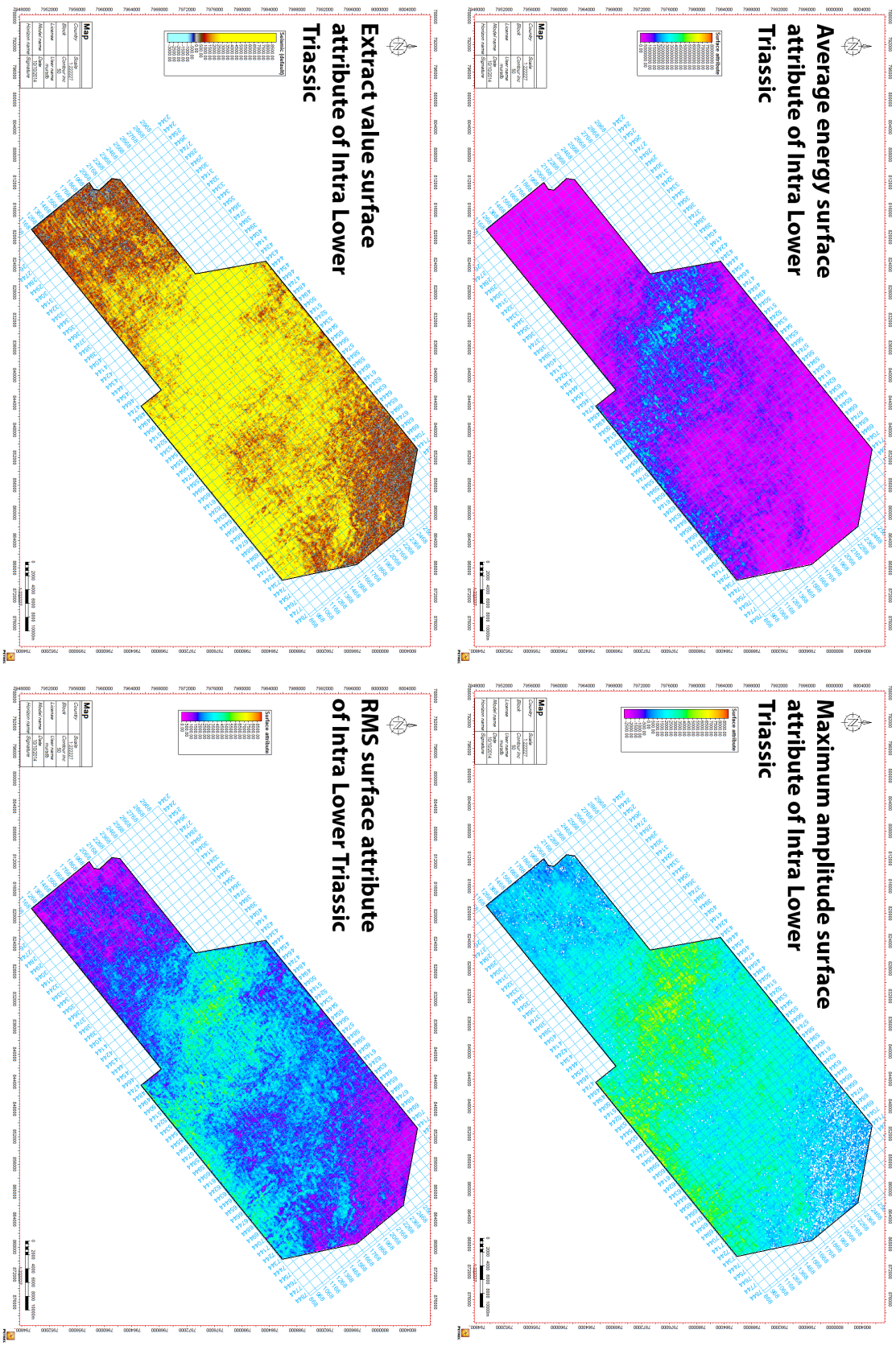

Figure C.2: Surface attributes of Intra Lower Triassic.

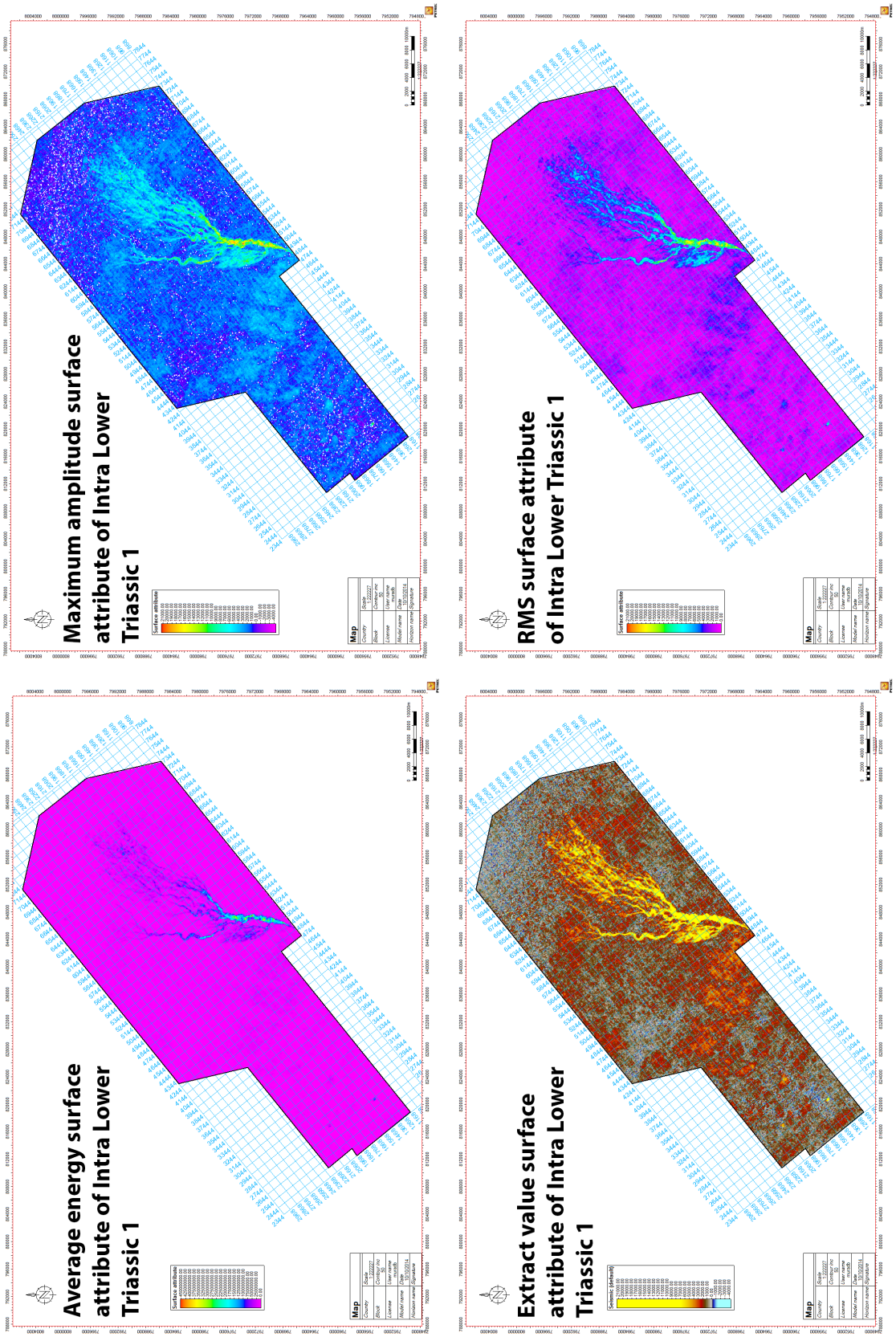

Figure C.3: Surface attributes of Intra Lower Triassic 1.

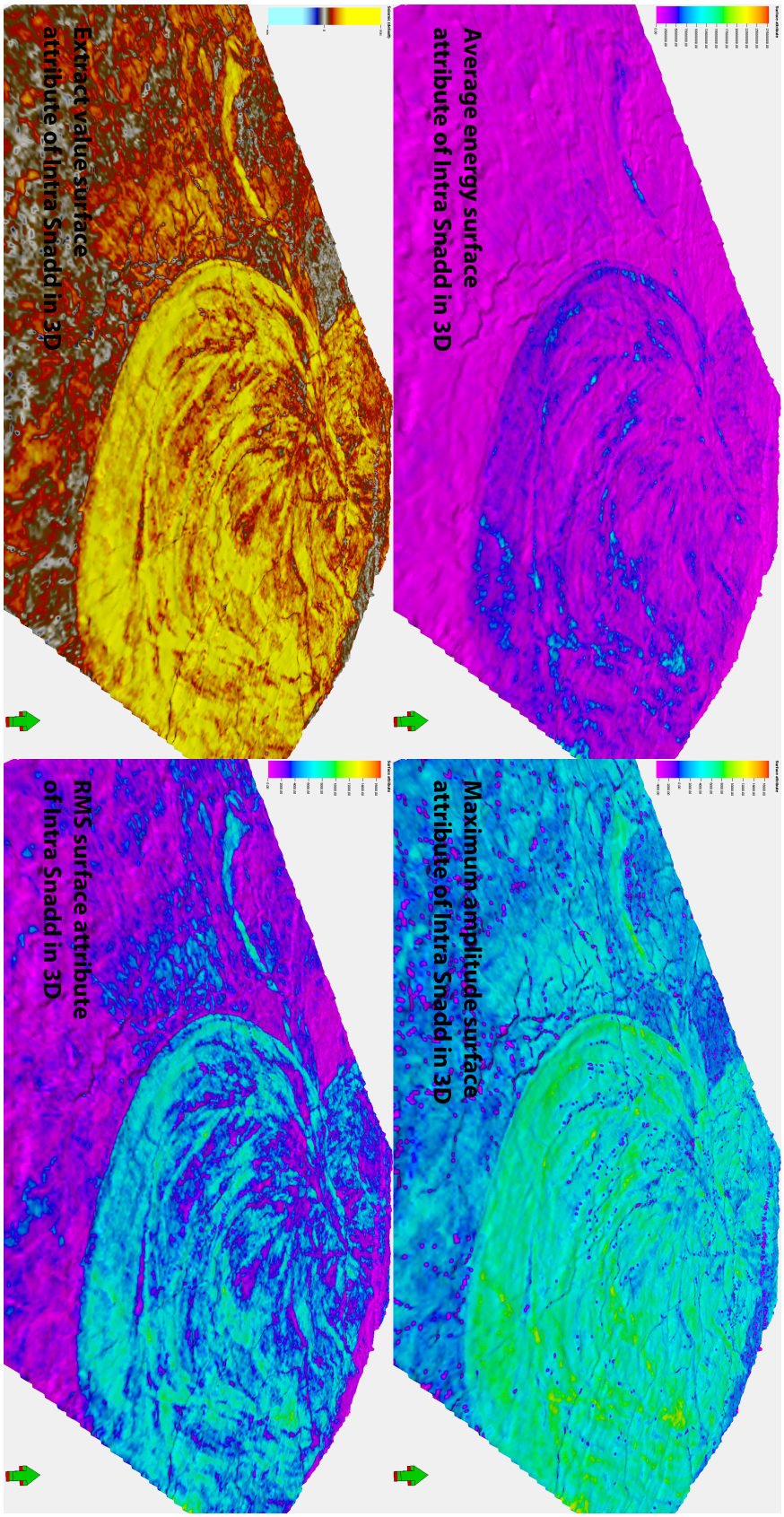

Figure C.4: Surface attributes of Intra Snadd in 3D.

Appendix D

Model constructions

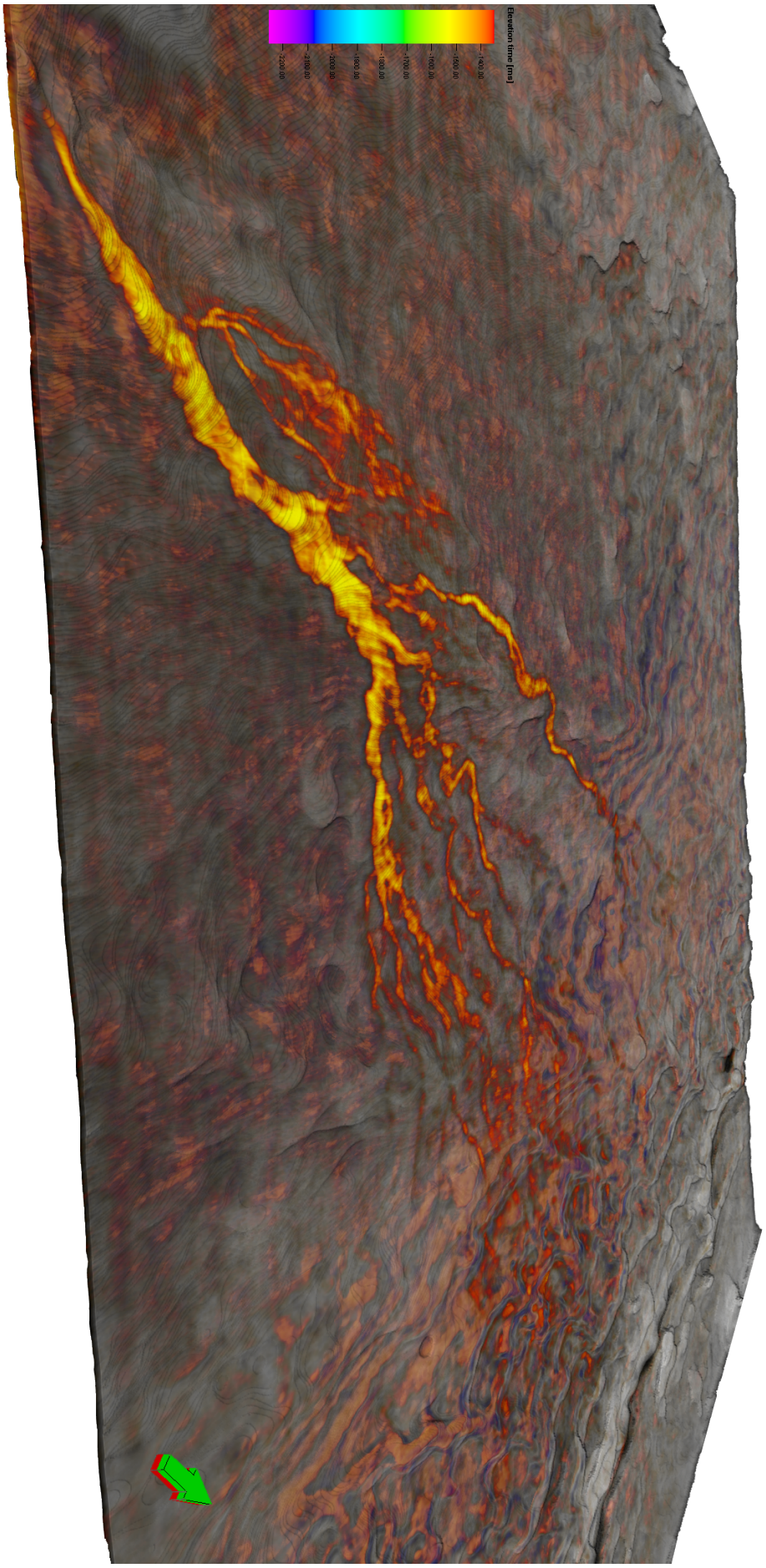

Figure D.1: Model of deep-water fan from seismic volume.

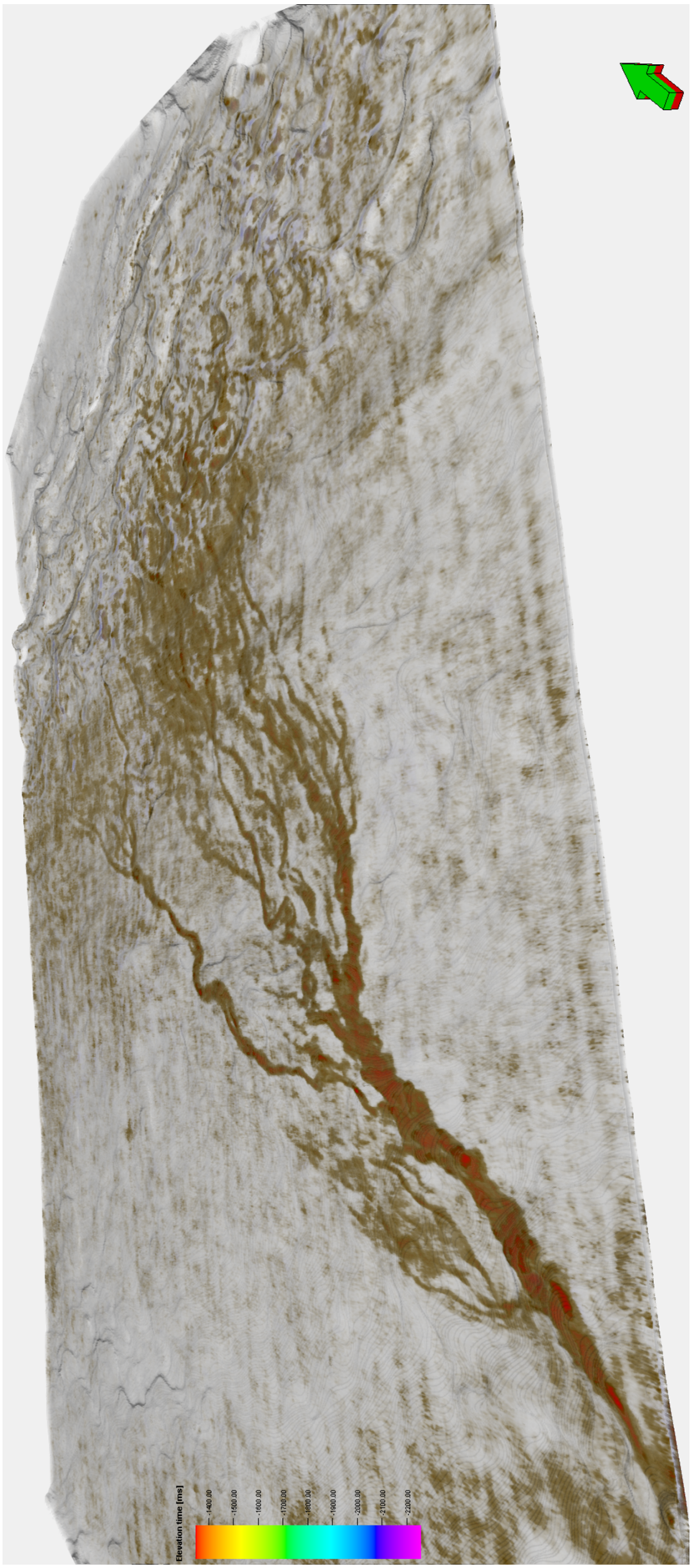

Figure D.2: Model of deep-water fan with RAI attribute.